

DISSERTATION

submitted to the

Combined Faculty of Natural Sciences and Mathematics

of the Ruperto Carola University Heidelberg, Germany

for the degree of

Doctor of Natural Sciences

Presented by

M.Tech. (Biotechnology) Mahak Singhal

Born in: Sri Ganganagar, India

Oral examination: 11.11.2019

Angio-regulation of liver neovascularization and lung metastatic progression

Referees:

Prof. Dr. Ana Martin-Villalba

Prof. Dr. Hellmut Augustin

The presented research was carried out in the department of Vascular Oncology and Metastasis at the German Cancer Research Center (DKFZ), Heidelberg, Germany, between November 2013 and July 2019.

Acknowledgments

I would like to thank everyone who has supported me throughout and contributed towards the successful completion of my doctoral thesis.

I express my heartfelt gratitude to my thesis supervisor **Hellmut Augustin** for allowing me to undertake such ambitious projects and mentoring me through ups and downs in the last six years. You have been an excellent teacher, and have trusted me with all the scientific independence and furnished me with career-shaping opportunities to guide my academic future. It has been an absolute pleasure, though something challenging, to work in close association with you. **Thank you!**

I am grateful to **Prof. Dr. Ana Martin-Villalba** for giving me the opportunity to accomplish my doctoral thesis in the combined faculties of Natural Sciences and Mathematics of the Ruprecht-Karls-Universität of Heidelberg and the Deutsche Krebsforschungszentrum (DKFZ). Thank you for your guidance and scientific advice during my thesis advisory committee meetings. I take this opportunity to also thank **Prof. Dr. Karin de Visser** and **Prof. Dr. Mathias Heikenwälder** for their active participation and thoughtful comments during my thesis advisory committee meetings. I also thank **Prof. Dr. Peter Angel** and **PD. Dr. Karin Müller-Decker** for taking part in my defense examination.

I am very thankful to the Helmholtz International Graduate School for Cancer Research for supporting me through my PhD research at the DKFZ. I would like to thank **Dr. Lindsay Murrells**, **Dr. Barbara Janssens**, and their teams for teaching me various soft skills during my tenure as a student council member.

Ashik Ahmed Abdul Pari, **Eva Besemfelder**, and **Nicolas Gengenbacher**, you three have been the backbone of our dream team and supported me with your love, and helped me to mature into a far better person as compared to the teenager who came to Heidelberg in 2013. You all have been extremely patient and have often overlooked my shortcomings. It has been an honor and great learning experience to work with you.

I thank **Junhao Hu**, **Soniya Savant**, and **Kshitij Srivastava** for mentoring me during the initial years of my PhD and helping me to shape my naïve thoughts into technically-feasible scientific projects. Junhao Hu, I thank you for numerous thought-provoking scientific discussions and your continuous encouragement during my PhD. You always made it look very easy and took a lot of pressure off my shoulders while preparing, revising, and editing our liver manuscript. I hope that this is just the beginning of our scientific collaboration.

I want to thank the whole A190 team for being a caring family to me. You welcomed me with an open heart and taught me every bit of what I know today. I cherish all the crazy scientific, geopolitical, and cultural discussion that we had during our coffee breaks. I thank all the past alumni (Aida, Annegret, Beate, Claudia, Corinne, Courtney, Fiona, Fuwei, Idil, Ignacio, Laura, Lise, Martin A., Martin T., Sila, Silvia, Stephanie K., Teresa, Tina, Wietske, and Zulfiyya) and the present members (Anja, Catalina, Denise, Dimitri, Donato, Evangelia, Guanxiong, Jingjing, Katharina, Ki Hong, Miki, Moritz, Paula, Stephanie G., and Xiaowen) for being part of this memorable journey. I especially thank Anja Runge for constructive and meticulous corrections of my thesis.

I want to thank Barbara, Benjamin, Carleen, Claudine, Daniela, Jessica, Lorena, Maike, Maria, Petra, and Stella for supporting me and answering all my technical and bureaucratic questions.

Acknowledgments

I have been very fortunate to meet a bunch of very friendly people who made my stay in Heidelberg enjoyable and especially, kept me going through the hard times during my PhD. I would like to thank Rakesh, Sakeena, Ashwin, Nalini, Yuvaraaj, Ruby, Khwab, Vishnu, Subhamoy, Supriya, Raghu, Himanshu, Sushma, Hiya, Anca, Laura, Agne, Cornelia, Chiara, Almira, Ling, Julia, Daniel, Simon, Sara, Azer, Antonino, Sebastian, Calvin, Devina, Felix, Pablo, Isa, Dwain, Ivan, and Thomas. Rakesh Sharma, I thank you for numerous night-long discussions about science over coffee. I thank Sankar, Yoga, Anirudh, Anuj, Swetha, Arathy, Partha, and the Zenithers (Tarun, Ashish R, Ashish K, Madhukant, Adarsh, and Diwaker) for always being there for me.

Lastly, I want to thank my family who have backed me throughout my life and more so, in the past six years. Thanks, mom and dad for being a constant source of inspiration and encouragement, and always motivating me to undertake the most challenging tasks. My sister, brother-in-law, and my niece, for being a never-lasting spark of joy and happiness. **Thank you!**

Table of contents

ACKNOWLEDGMENTS.....	I
TABLE OF CONTENTS.....	©
LIST OF FIGURES.....	V
LIST OF TABLES	V@
ZUSAMMENFASSUNG	1
SUMMARY	2
1. INTRODUCTION	3
1.1. DEVELOPMENT OF THE VASCULAR SYSTEM	3
1.1.1. <i>Embryonic development of the vascular system</i>	3
1.2. VASCULAR CONTROL OF ORGANOGENESIS	5
1.3. ORGANOTYPIC VASCULATURE MAINTAINS TISSUE HOMEOSTASIS.....	6
1.3.1. <i>Cellular source of endothelial cells during adult neoangiogenesis</i>	7
1.3.2. <i>Liver as a model organ to study tissue regeneration</i>	8
1.3.3. <i>Clinical assessment of HSC-based regenerative therapies for liver damage</i>	9
1.4. INSTRUCTIVE ROLE OF ENDOTHELIAL CELLS DURING TUMOR PROGRESSION	10
1.4.1. <i>Discovery of VEGF/VEGFR</i>	11
1.4.2. <i>Rise of anti-VEGF as the first stroma-targeting therapy</i>	12
1.4.3. <i>Second generation anti-angiogenic therapy</i>	14
1.4.4. <i>Beyond angiogenesis, EC-derived signals promote metastasis</i>	15
1.5. AIMS OF THE STUDY	18
2. RESULTS AND DISCUSSION	19
2.1. ENDOTHELIAL CELL FITNESS DICTATES THE SOURCE OF REGENERATING LIVER VASCULATURE	19
2.1.1. <i>Bone marrow-derived cells incorporate in the irradiation-damaged liver vasculature</i>	19
2.1.2. <i>BMDMC do not incorporate in the intact vasculature during liver regeneration</i>	24
2.1.3. <i>Liver neovascularization during chronic liver damage</i>	27
2.1.4. <i>Bone marrow-based cellular therapies fail to promote liver vascular regeneration</i>	29
2.2. TEMPORAL MULTI-OMICS IDENTIFIES LRG1 AS A VASCULAR INSTRUCTOR FOR EARLY METASTATIC COLONIZATION	34
2.2.1. <i>Modeling metastatic disease in mouse tumor models</i>	34
2.2.2. <i>Transcriptional evolution of lung EC during metastasis</i>	35
2.2.3. <i>Lrg1 mediates EC responsiveness to tumor progression</i>	42
2.2.4. <i>Leukocyte-derived LRG1 is dispensable for tumor progression</i>	48
2.2.5. <i>Single-cell RNA-seq analysis reveals no changes in the vascular tree during metastasis</i>	50
2.2.6. <i>Systemically elevated LRG1 facilitates metastatic colonization</i>	53
2.2.7. <i>LRG1 inhibition limits metastasis and prolongs overall survival</i>	56
3. CONCLUSION	58
3.1. BONE MARROW-DERIVED CELLS HARBOR REPARATIVE POTENTIAL AND CAN PHYSICALLY INTEGRATE INTO THE AILING LIVER VASCULATURE	58
3.2. RESIDENT EC ARE PROLIFERATION-EFFICIENT AND CAN RESTORE LIVER VASCULATURE	59
3.3. TEMPORAL EVOLUTION OF LUNG EC WITH METASTATIC PROGRESSION	60
4. MATERIALS AND METHODS	62
4.1. MATERIALS	62
4.1.1. <i>Chemicals</i>	62
4.1.2. <i>Cells</i>	62
4.1.3. <i>Cell culture reagents</i>	62

Table of contents

4.1.4.	<i>Growth factors, proteins and enzymes</i>	62
4.1.5.	<i>Primers and Oligonucleotides</i>	63
4.1.6.	<i>TaqMan™ assays</i>	63
4.1.7.	<i>PCR/RT-qPCR reagents, nucleotides and buffers</i>	64
4.1.8.	<i>Antibodies</i>	64
4.1.9.	<i>Staining reagents</i>	65
4.1.10.	<i>Kits</i>	65
4.1.11.	<i>Reagents for animal experimentation</i>	66
4.1.12.	<i>Consumables</i>	66
4.1.13.	<i>Equipments</i>	67
4.1.14.	<i>Softwares</i>	68
4.1.15.	<i>Solutions and buffers</i>	68
4.2.	METHODS	69
4.2.1.	<i>Mouse experiments</i>	69
4.2.2.	<i>Cells</i>	69
4.2.3.	<i>Tumor models</i>	69
4.2.4.	<i>Partial hepatectomy</i>	70
4.2.5.	<i>Transplantation of HSC without irradiation</i>	70
4.2.6.	<i>Irradiation-preconditioned bone marrow chimeric mice</i>	70
4.2.7.	<i>Microarray analysis</i>	71
4.2.8.	<i>Constitutive labeling of EC in VECad-Cre^{ERT2}xRosa-YFP^{fl/fl} mice</i>	71
4.2.9.	<i>Chronic liver injury models</i>	71
4.2.10.	<i>Regenerative therapy</i>	72
4.2.11.	<i>Flow cytometry analysis</i>	72
4.2.12.	<i>Bulk RNA-sequencing and data analysis</i>	73
4.2.13.	<i>Single-cell RNA-sequencing</i>	73
4.2.14.	<i>Serum Proteomics</i>	74
4.2.15.	<i>Hematoxylin and eosin staining</i>	76
4.2.16.	<i>Immunofluorescence stainings and analysis</i>	76
4.2.17.	<i>Gene expression analysis</i>	77
4.2.18.	<i>Statistical analysis</i>	77
	ABBREVIATIONS	78
	PUBLICATIONS	82
	REFERENCES	83

List of figures

Figure 1. Relationship between vascular and hematopoietic cells.....	5
Figure 2. Stages of metastatic progression.....	11
Figure 3. Evolution of the (pre-)metastatic niche during metastasis.....	17
Figure 4. Irradiation-conditioned BM chimeras recruit BMDMC to the regenerating liver.	20
Figure 5. Bone marrow-derived EC are functionally indistinguishable from resident liver EC.....	21
Figure 6. Irradiation-based myeloablation induces EC injury.....	24
Figure 7. BM cells do not contribute to the regeneration of liver vessels in non-myeloablative chimeric mice.	25
Figure 8. Regeneration of liver vasculature relies on preexisting EC.....	26
Figure 9. Liver neovascularization during chronic liver injury.....	28
Figure 10. Infused BM cells do not incorporate into the regenerating liver vasculature.	31
Figure 11. G-CSF mobilized BM cells do not incorporate into the regenerating liver vasculature.	33
Figure 12. Mouse models to mimic spontaneous metastasis.	35
Figure 13. Temporal analysis of lung EC during tumor progression.	36
Figure 14. Transcriptomic evolution of lung EC during metastasis.	37
Figure 15. Lung EC show enrichment of genes related to inflammatory responses.	39
Figure 16. Presence of a primary tumor alters the immune landscape in the lung.....	40
Figure 17. Immune-phenotyping of lung tissue during metastasis progression.	42
Figure 18. Expression kinetics of genes involved in the EC development gene set.....	43
Figure 19. Upstream regulators of EC transcriptional changes.....	44
Figure 20. Proteomic analysis of serum during metastasis progression.....	46
Figure 21. LRG1 is systemically upregulated in a breast (MMTV-PyMT) cancer model.....	47
Figure 22. Leukocyte-derived LRG1 is dispensable for metastasis.	49
Figure 23. Lrg1-KO BM chimeras exhibit no apparent defects in primary tumor vasculature.	50
Figure 24. Single-cell analysis of lung endothelium during metastasis.....	52
Figure 25. Vascular endothelial cells are the major source of Lrg1.....	53
Figure 26. Elevated levels of LRG1 facilitate metastatic colonization.....	54
Figure 27. Systemic LRG1 does not affect extravasation of circulating tumor cells.	56
Figure 28. LRG1 neutralization inhibits metastasis.....	57
Figure 29. EC fitness dictates the source of regenerating liver vasculature.	59
Figure 30. EC-derived angiocrine signals facilitate early metastatic colonization.....	61

List of tables

Table 1	Chemical suppliers.....	62
Table 2	Mouse tumor cell lines.....	62
Table 3	Cell culture reagents.....	62
Table 4	Growth factors, proteins and enzymes.....	62
Table 5	Genotyping primers.....	63
Table 6	TaqMan™ assays.....	63
Table 7	PCR and RT-qPCR reagents, nucleotides and buffers.....	64
Table 8	Primary antibodies.....	64
Table 9	Secondary antibodies.....	65
Table 10	Staining reagents.....	65
Table 11	Kits.....	65
Table 12	Reagents for animal experimentation.....	66
Table 13	Consumables.....	66
Table 14	Equipments.....	67
Table 15	Softwares.....	68
Table 16	Recipe for preparing solutions and buffers.....	68

Zusammenfassung

Blutgefäße durchziehen den gesamten Körper und versorgen jede Zelle mit Sauerstoff und Nährstoffen. Endothelzellen (EC) stellen die innerste Zellschicht von Blutgefäßen dar, welche lange Zeit ausschließlich als inerte und passive Grenzfläche betrachtet wurde. In der letzten Dekade haben jedoch zahlreiche Forschungsergebnisse eine aktive Rolle von EC bei der Aufrechterhaltung einer physiologischen Gewebshomöostase aufgezeigt. Zusätzlich spielen angiokrine Mediatoren aus EC, die multidirektional Signale innerhalb der lokalen Gewebsmikroumgebung vermitteln, eine übergeordnete Rolle in der Wundheilung und zahlreicher pathologischer Prozesse, unter anderem bei Krebserkrankungen. Die vorliegende Studie zielte darauf ab (i) zelluläre Quellen zu ermitteln, die an der Reparatur und Erneuerung von Blutgefäßen in adulten Mäusen beteiligt sind, sowie (ii) die dynamische Evolution des Genexpressionsmusters von EC während der Progression von Tumormetastasen zu untersuchen.

Um die unterschiedlichen zellulären Quellen aufzuschlüsseln, die an der vaskulären Reparatur beteiligt sind, wurde als Untersuchungsmodell eine partielle (zwei Drittel-) Hepatektomie (PHx) in adulten Mäusen durchgeführt. Die adulte Leber hat die einzigartige Fähigkeit ihre verlorene Gewebemasse innerhalb von 10 Tagen nach PHx komplett zu regenerieren. Genetische Abstammungsuntersuchungen („lineage tracing“) zeigten, dass unbeschädigte, nach PHx verbliebene Lebergefäßzellen effizient proliferieren um ein vollständig funktionelles vaskuläres Netzwerk wiederherzustellen. Im Gegensatz hierzu, führt eine Strahlenbelastung zu einer derartigen Beschädigung lokaler Leber-EC, dass Knochenmarkszellen für die vaskuläre Reparatur benötigt werden. Daher können sowohl lokale EC sowie Vorläuferzellen aus dem Knochenmark als potentielle Quellen der Lebergefäßregeneration dienen, deren relative Beteiligung von der zellulären Fitness der verbliebenen Lebervaskulatur abhängt.

Um zu verstehen welche Rolle angiokrine Mediatoren bei der Etablierung einer metastatischen Nische spielen, wurde in einem fortschrittlichen Maustumormodell vergleichend sowohl das Transkriptom von Lungen-EC als auch das Serum-Proteom an verschiedenen Zeitpunkten der Metastasenprogression bestimmt. *Leucine Rich alpha-2-Glycoprotein 1* (LRG1) wurde hierbei als ein EC-spezifisches Signal identifiziert, dessen Genexpressionsmuster die Abfolge einer Tumor-induzierten systemischen Entzündungsreaktion widerspiegelt. Weitere Einzelzell-Analysen von Lungen-EC sowie Multi-Organ-Gefäßanalysen offenbarten, dass LRG1 bei einer Tumorerkrankung in multiplen Gefäßbetten hochreguliert wird. Funktionell erleichtert ein systemisch erhöhter LRG1-Spiegel die metastatische Kolonisierung. Daher unterdrückt eine postoperative adjuvante Therapie mit einem LRG1-neutralisierenden Antikörper Metastasierung und verlängert das Gesamtüberleben, im Vergleich zu Kontroll-IgG-behandelten Mäusen. Insgesamt repräsentieren die erstellten Datensätze eine beispiellose Ressource um per intelligenter Datenanalyse angiokrine Mediatoren zu identifizieren, die als mögliche Zielstrukturen dienen könnten, um eine metastatische Progression zu limitieren.

Summary

Blood vessels are disseminated throughout the body and nourish every cell with oxygenated blood. Endothelial cells (EC) that line up the vessels were long believed to form a passive barrier, and were considered quiescent in nature. Intense research efforts, during the past decade, have uncovered rather an active gatekeeper function of EC to maintain physiological tissue homeostasis. In turn, EC-derived angiocrine signals, which mediate multi-directional crosstalk with local tissue microenvironment, are crucial for tissue repair and different pathological disorders including cancer. The present study was aimed at investigating (i) the cellular sources that contribute towards vascular repair and rejuvenation in adult mice, and (ii) the dynamic evolution of EC gene signature with metastatic progression.

To elucidate different cellular sources that might contribute to vascular repair, 2/3rd partial hepatectomy (PHx) was performed on adult mice. The adult liver harbors a unique ability that it is capable of restoring its lost mass within 10 days following PHx. Lineage tracing experiments unveiled that under non-vascular damaging conditions, the remaining liver vasculature is proliferation efficient, and can yield a fully functional vascular network. However, following an irradiation exposure, liver EC witnessed catastrophic damage, and required a bone marrow-derived contribution for liver vascular repair. Thus, both resident and bone marrow-derived cells can act as the potential sources, but their contribution relies on the fitness of the remaining liver vasculature.

To understand the underlying role of angiocrine factors in promoting a metastatic niche, comparative lung EC transcriptomic and serum proteomic screens were undertaken at sequential stages of disease progression in an advanced mouse model of metastasis. Leucine Rich alpha-2-Glycoprotein 1 (LRG1) was identified as an EC-specific signal whose gene expression closely reflected tumor-induced systemic inflammation. Further, single-cell analysis of lung EC, as well as multi-organ vascular analysis, revealed that *Lrg1* expression was upregulated throughout all vascular beds with the presence of a primary tumor. Functionally, systemically elevated levels of LRG1 facilitated metastatic colonization. In turn, postsurgical adjuvant administration of LRG1-neutralizing antibody suppressed metastasis and improved overall survival of mice as compared to the IgG-control treatment. Overall, the established datasets will serve as an unparalleled resource to datamine angiocrine signals, which can be targeted to limit metastatic progression.

1. Introduction

The vascular system consists of blood and lymph vessels, which are disseminated throughout all organ systems and are used not only as conduit for oxygen- and nutrient-rich blood but also for effective drainage to recycle excess interstitial fluid (1). Indeed, blood vessels form human body's largest surface area covering approximately 7,000 m² and extending nearly 50,000 km in length. Tightly intertwined endothelial cells (EC) constitute an interface between the circulation and the parenchymal tissue. These tissue-specific vascular beds thereby exert gatekeeper functions on tissue homeostasis by deploying sets of organ-specific chemokines and morphogens, defined as angiocrine factors (2, 3). Vascular malformation or dysregulation of homeostatic angiocrine signals is the single most common cause of human mortality accounting for more than two-thirds of deaths. Research in the past decade has demonstrated that while a set of EC-derived signals orchestrates tissue regeneration, others can nourish the metastatic niche to allow outgrowth of disseminated tumor cells (4, 5). Therefore, a better understanding of endothelial cell biology and different angiocrine signals will warrant mechanism-based therapeutic development for various fields of biomedical research.

1.1. Development of the vascular system

The establishment of a fully functional cardiovascular system is an early imperative event for embryonic development (6). Successive processes of vasculogenesis and angiogenesis result in embryonic vascular network. Vasculogenesis, refers to *de novo* formation of blood vessels from mesoderm-derived precursor cells while angiogenesis includes the formation of subsequent blood vessels by the expansion of differentiated EC of the neighboring vessels (7). Upon maturation, the vascular system encompasses a hierarchical network of arteries, arterioles, capillaries, venules and veins, which not only nourishes the embryo with nutrients and oxygen but also provides inductive signals for organogenesis through organotypic vasculature (8). While vasculogenesis appears to be a unique mechanism for early embryonic vascular development, (neo)-angiogenesis is required during later stages of embryonic development as well as in adults, especially under pathological conditions such as wound healing, tissue regeneration, and tumor progression.

1.1.1. Embryonic development of the vascular system

Vascular development commences shortly after gastrulation as an early embryonic event. The primary vascular network is established by vasculogenesis, wherein mesoderm-derived hemangioblasts, common progenitors for EC as well as hematopoietic cells, cluster together to form blood islands in the extraembryonic yolk sac around embryonic day E7.0-7.5 (9-11). These blood islands turn into initial blood vessels demarcating an external layer of endothelial progenitor cells defined as angioblasts and an inner core of spherical cells, which eventually constitute the blood. Thereafter, neighboring blood

islands extend towards each other and anastomose to form a primordial vascular plexus (12-14). In parallel, intraembryonic mesodermal cells assemble symmetrically at the lateral sides of the embryo to form the pre-endocardial tubes. They later fuse to give rise to the endocardium of the heart (10). Simultaneously, intraembryonic blood vessels acquire either arterial or venous fate thereby, giving rise to the dorsal aorta and cardinal vein (15). The appearance of first arterial and venous blood vessels marks the inception of blood circulation.

After building the yolk sac vasculature and paired dorsal aorta, EC sprout into avascular ectoderm-derived organs thereby, expanding the preexisting network of blood vessels. Further extension of vascular labyrinth occurs either via sprouting angiogenesis or by splitting the existing vessels through intussusception (4, 16, 17). Sprouting angiogenesis begins with proangiogenic stimuli inducing a highly motile and invasive phenotype in endothelial cells referred to as tip cells. Tip cells probe for the guidance cues in the nearby microenvironment and lay the ground for the following stalk cells to proliferate and elongate the vessel lumen. Eventually, tip cells from neighboring sprouts anastomose to build vessel loops. Thereafter, the initiation of blood flow and the recruitment of mural cells mark a fully functional blood vessel (18). Intussusceptive microvessel growth commences with sporadic closing of opposite capillary walls to raise transluminal pillars (19-21). Subsequently, these pillars increase in girth as mural cells invade into them. Sometimes, pillars may rise in series to yield a fold-like split in a vessel thereby, demarcating a hierarchical network of feeding vessels. Unlike sprouting angiogenesis, intussusception is achieved in a relatively rapid, energetically- and metabolically-efficient manner as well as is accompanied by an almost absence of endothelial cell proliferation (7, 22). Taken together, sequential processes of vasculogenesis and angiogenesis provide a rudimentary vascular mesh, which is further expanded and pruned by intussusception.

It was long believed that endothelial cells are self-contained, and are direct descendants of a single germ layer – mesoderm. Yet, with technical advancements, a growing number of studies suggest that other cellular sources may contribute to the developing endothelium, especially to the fetal liver vasculature. Endoderm-derived KDR^+ $FOXA2^+$ cells were described to give rise to both hepatocytes and $CD31^+$ liver EC (23, 24). Similarly, a fraction of fetal liver vasculature was reported to be of endocardial origin and shared a common ancestry with the coronary arteries (25). More recently, yolk sac-derived erythro-myeloid progenitors (EMP), precursors for tissue-resident macrophages, were found to incorporate and intersperse into the intraembryonic vascular plexus (26, 27). EMP-derived EC were detected in multiple organs however, they predominated amongst the liver sinusoidal endothelial cells (LSEC; accounting up to 60%). The dependence of liver growth on rapid vascular expansion may justify the liver being a preferential homing site for the endoderm-derived cells as well as EMP. Although the recent discoveries have uncovered new cellular origins of embryonic EC, it still remains unanswered whether EC-derived from different sources exhibit heterogenous functional characteristics during physiological and pathological conditions.

1.2. Vascular control of organogenesis

Establishment of the cardiovascular system is a prerequisite for the process of organogenesis and later embryonic development. Apart from the very fundamental function of plumbing blood, the endothelium provides instructive cues to facilitate organogenesis (8). During liver organogenesis, endothelial cells draw a border to separate newly-specified hepatic endoderm cells and the septum transverse mesenchyme, thereby promoting liver morphogenesis (28). Likewise, blood vessels impart inductive signals for endocrine pancreatic differentiation (29). The development of the hematopoietic system and the vascular system goes hand in hand as they share a common ancestry. Although budding of the hematopoietic stem cells (HSC) from the aortic-gonado-mesonephros (AGM) region was described in the 1920s, their exact cell of origin remained a highly controversial and unanswered question until recently (30). In 2008, employing definite genetic lineage tracing tools, hemogenic endothelium, but not AGM mesenchyme, was found capable of yielding multipotent long-term HSC (31). Different hierarchical models have been discussed to establish a lineage relationship between hematopoietic and endothelial cells (Fig. 1). Similarly, the instructive role of endothelium has been reported in the case of adipose (32) and bone (33) tissue, and during kidney (34), and neural (35) development. Overall, EC actively communicate with the parenchymal cells to steer the organ development and to achieve functional homeostasis.

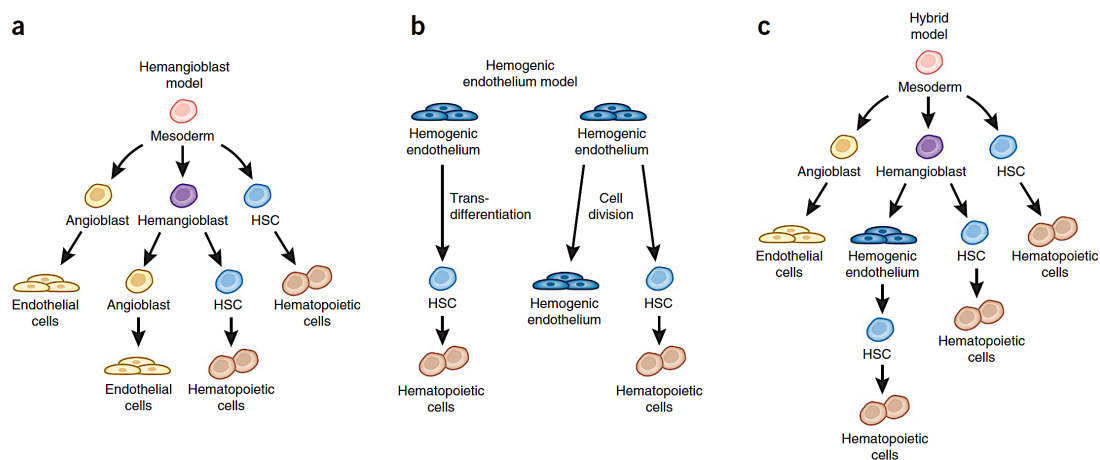


Figure 1. Relationship between vascular and hematopoietic cells. Mesoderm-derived cells serve as the common progenitors for both EC and hematopoietic cells. Yet, the exact occurrence of events remains controversial. (A) Hemangioblasts were long believed to differentiate into either angioblast (EC-precursor) or hematopoietic stem cells (HSC, the common precursor for all hematopoietic cells) (30). (B) A growing number of studies argued against the existence of hemangioblasts and demonstrated that mesoderm-derived hemogenic endothelium could either trans-differentiate into HSC or undergo asymmetric cell division to produce both EC and HSC (31). (C) More recently, a study undertaking detailed molecular analysis rather suggested a hybrid model incorporating both hemangioblasts and hemogenic endothelium (36). The spatiotemporal regulation of hemogenic endothelial cells, during embryonic development, might also be linked to various extrinsic factors defined by the organ-specific vascular beds. Adapted with permission from (30).

1.3. Organotypic vasculature maintains tissue homeostasis

Blood vessels constitute a systemically disseminated organ, which serves as a critical interface for exchange between the blood and local organ environment. Similar to their instructive role during organogenesis; organ-specific EC play a central role in sustaining tissue homeostasis, orchestrating tissue repair, and preventing pathological disorders (2, 5). EC-derived angiocrine factors act in a paracrine and/or juxtacrine manner on different cellular entities within the tissue microenvironment (basolateral side) and on the hematopoietic cells (luminal side) to maintain a functional equilibrium. Upon physiological perturbation such as inflammation, tissue wounding, pathological disorders; EC exhibit a carefully choreographed response to resolve a life-threatening situation and to re-attain the tissue homeostasis. Organotypic vascular niches are well-recognized to house quiescent tissue stem cells and to promote their self-renewal, thereby providing an adaptive platform to precisely regulate the tissue turnover rate. For example, subsets of brain EC exhibited a planar morphology which allowed for a direct contact with neural stem cells. Under steady state conditions, endothelial expression of membrane-bound EFNB2 and JAG1 facilitated neural stem cell dormancy (37). Furthermore, EC, located in the choroid plexus, secreted NTF3 into cerebrospinal fluid to modulate neural stem cell quiescence throughout the brain (38). Likewise, the adipose vasculature furnished a progenitor niche to harbor proliferating adipocytes and assisted in attaining systemic glucose homeostasis (39). In line with the fetal development, vascular niches modulate steady-state hematopoiesis via a battery of angiocrine-acting molecules like JAG1, KITLG, CXCL12, etc. Ablation of any of these angiocrine molecules negatively affected the hematopoietic recovery and resulted in the exhaustion of HSC compartment (40).

Apart from providing a safe house for the tissue-specific stem cells, the angiocrine role of blood vessels during tissue regeneration has recently been unveiled. The lung and liver present a unique experimental feature that following a partial loss of tissue (pneumonectomy/hepatectomy), the remaining healthy lobes undergo a rapid regenerative process to regain the lost tissue mass (41). After unilateral pneumonectomy (PNx), lung EC produced MMP14 which, in turn, promoted the shedding of HB-EGF to allow alveolar reconstitution (42). Concomitantly, neutralization of MMP14 resulted in an impaired tissue regeneration which could be rescued by intravascular transplantation of MMP14⁺ capillary EC into a pneumonectomized mouse. Furthermore, platelet-derived SDF1 primed the lung vasculature to secrete MMP14, thereby driving (neo)-alveologenesis (43). In case of a chronic injury model, pulmonary EC, in concordance with the perivascular mural cells, elicited a fibrotic response which hinders tissue repair (44). Mechanistically, lung EC recruited perivascular fibroblasts in a JAG1-dependent manner to mount a fibrotic response. Therefore, a better understanding of angiocrine circuits will enable correction of maladapted vascular niches to ameliorate fibrosis and spur tissue regeneration.

The liver is a fascinating and one of the most-studied experimental organs for tissue regeneration. Considering its crucial role in regulating blood glucose and ammonia levels, the liver-to-body weight ratio is perhaps one of the most precisely controlled physiological parameters (45, 46). Therefore, the

liver requires a well-coordinated effort especially between the two major hepatic populations – hepatocytes and liver sinusoidal EC (LSEC), to successfully attain functional homeostasis following an insult such as 2/3rd partial hepatectomy (PHx). After PHx, every cell in the remaining one-third of the liver theoretically needs to cycle 1.66 times to restore the lost mass. Yet, not all the cell types proliferate at once, liver regeneration is a spatiotemporally-controlled procedure to ensure a complete tissue restoration without compromising the liver function during the repair process. Hepatocytes are the first ones to proliferate with their proliferation peaking around 24 hours post-PHx. This is achieved by a rapid inhibition of LSEC-derived TGF β that functions as an endogenous inhibitor of hepatocyte proliferation (47). During this early inductive phase (1-3 days post-PHx), LSEC additionally downregulated ANGPT2, a key autocrine angiogenic signal, thereby, restricting the proliferation of the LSEC compartment. During the angiogenic phase (3-8 days post-PHx), gradual recovery of LSEC-derived ANGPT2 unleashed the brake and allowed the expansion of the remaining liver vasculature. Mice lacking *Angpt2* displayed a delayed tissue regeneration. Furthermore, the alteration in the hepatic blood flow was recently found to correlate with the secretion of angiocrine modulators of liver regeneration (48). After PHx, all the hepatic blood flows through only one-third of the original liver, this enhanced blood perfusion resulted in ITGB1- and VEGFR3-mediated LSEC expression of hepatocyte growth factor which indeed promoted hepatocyte proliferation (49). The above-mentioned examples, concerning different vascular beds and adult tissue regeneration, strongly emphasize on the emerging, yet the central role of endothelial-derived signals on tissue homeostasis. Despite exerting a myriad of gatekeeping functions on tissue microenvironment, the cellular origin of endothelial cells during adult neoangiogenesis remains elusive.

1.3.1. Cellular source of endothelial cells during adult neoangiogenesis

Any disruption in tissue homeostasis, in the case of pathologies such as tissue damage, inflammation, cancer, and cardiovascular disorders, requires an active proliferation of the vascular network to resolve the crisis (50, 51). EC are not post-mitotic implying that they retain their ability to undergo mitosis if necessary (14, 52). Therefore, it was long believed that postnatal vascular expansion was solely achieved by the process of angiogenesis, that is, by proliferation, migration, and pruning of preexisting blood vessels (53). And, the process of vasculogenesis was reported to be largely restricted to the early embryonic development. However, the isolation of putative circulating endothelial progenitor cells (EPC) from human peripheral blood and their direct contribution to augment an ailing ischemic vasculature opened a new chapter in the field of vascular biology research (54). First, EPC, a fraction of circulating mononuclear cells with surface expression of CD34 and VEGFR2, were shown to proliferate *in vitro* on fibronectin-coated dishes and to uptake acetylated low-density lipoprotein (55). Second, when injected intravenously, *in vitro* expanded EPC could home to the ischemic limb tissue and directly incorporate into newly-growing capillaries. These two findings strongly supported the

presence of immature circulating EPC which can contribute and aid postnatal vascular expansion via the process of vascularization (56).

The emergence of postnatal vascularization met with a lot of excitement as it opened new therapeutic avenues especially for pathologies with a defunct vasculature (57). Indeed, this revolutionary new field of research, to date, has seen approximately 3,000 publications with “endothelial progenitor cells” embedded in their title. Soon after the isolation of circulating EPC, researchers realized that CD34⁺ VEGFR2⁺ cells constitute a very heterogeneous population and it might include circulating mature EC (58). Therefore, further research focused on underpinning molecular and functional characteristics of the EPC population. CD133 was identified as the third most important qualifier to permit a cell as an endothelial precursor. CD133 was found to be restricted to the circulating EPC while both the activated and the mature endothelium were tested negative for CD133 (58). Today, researchers, across the globe, employ a variety of surface markers for the isolation of EPC including CD34, VEGFR2, CD133, CD105, CD117, Tie1, Tie2, and CXCR4 (59). Several of these markers either overlap with HSC or with mature EC (60, 61). Thus, even after two decades of exciting and rigorous cutting-edge research, no universal definition exists to isolate circulating EPC and their mere existence still remains a highly controversial topic (62-64).

1.3.2. Liver as a model organ to study tissue regeneration

To investigate adult neovascularization, oftentimes, the liver has been employed as a model organ. This is primarily attributed to a very high regenerative potential of the liver (65) as well as the continued lack of availability of donor tissue for liver transplantation in the clinics (66). Different preclinical models have been deployed to study tissue repair/regeneration in the liver which includes both acute (such as partial (2/3rd) hepatectomy or a single injection of dimethylnitrosamine (DMN) or monocrotaline (MCT)) and chronic (such as repeated administration of carbon tetrachloride (CCl₄) or adenovirus-mediated damage) challenges (67, 68). Considering multiple cellular sources contribute to the embryonic liver vasculature (as discussed in section 1.1.1.), bone marrow (BM)-derived precursors were hypothesized to assist the restoration of liver vasculature (69). In a very elegant experiment with parabiotic pairs, wherein a global GFP-expressing mouse was conjoined with a wild-type counterpart, myeloid progenitors (both common myeloid progenitors and granulocyte/macrophage progenitors) contributed 3.9% of the liver endothelial cells under steady-state conditions over a period of 6 months (70). Additional experiments revealed that these BM-derived LSEC were EGFP⁺ CD45⁻ CD31⁺ VWF⁺, hence, supporting the notion that BM-derived cells were functional and genuinely integrated into liver vessels. Approximately 4% BM contribution under steady-state conditions ignited the hypothesis that perhaps following an acute liver injury; BM precursors might contribute substantially to the ailing liver vasculature (71, 72).

To investigate the contribution of BM precursors, lineage tracing experiments were performed on the livers of MCT-treated mice (73). Indeed, BM-derived cells replaced almost one-quarter of the resident

LSEC (74). These BM-derived cells were CD45⁺ CD133⁺ and, thus defined as LSEC progenitor cells (SPC). Spatially, SPC integrated throughout the liver vessels including periportal, mid-lobular, and central vein region. Apart from the vascular restoration, SPC expressed very high levels of hepatocyte growth factor thereby facilitating liver rejuvenation. These results underlined a crucial role of SPC-expressed paracrine factors in stimulating tissue repair. Concomitantly, infusion of BM cells following PHx revealed a strong incorporation of CD133⁺ SPC into the liver vasculature (75). Interestingly, original non-fenestrated SPC, upon integration, acquired fenestrae emphasizing on their differentiation into *bona fide* LSEC. In fact, bone marrow suppression led to impaired liver regeneration, even during the inductive phase, which implies an essential role of BM progenitor-derived factors on hepatocyte proliferation.

Detailed analysis of bone marrow tissue unveiled a rapid expansion of BM-derived SPC on day 3 post-PHx (75). This led to an increased count of mobilized SPC which could be found circulating in the peripheral blood. Given that the timing of BM-derived SPC proliferation coincided with the commencement of the angiogenic phase further provided evidence of SPC involvement in liver regeneration. Mechanistically, hepatic vascular endothelial growth factor (VEGF) mediated long distance crosstalk to mobilize BM precursors and subsequently, their differentiation and integration into newly formed liver vessels (76). Taken together, recovering liver vasculature absorbs circulating BM-derived SPC which, in turn, provide cues for the proliferation of other cellular entities to attain a morphologically normal, and fully functioning liver tissue.

1.3.3. Clinical assessment of HSC-based regenerative therapies for liver damage

The overwhelming preclinical evidence that BM-derived precursors contribute to liver rejuvenation promoted HSC-based cell therapies to the clinics (77-79). Initial clinical studies were proof-of-concept trials and were primarily aimed at assessing safety, tolerability, and associated side-effects of hematopoietic cell-based therapies (80, 81). Administration of whole bone marrow mononuclear cells in patients with liver cirrhosis resulted in increased serum albumin and enhanced the expression of proliferating cell nuclear antigen, thereby, suggesting active proliferation of hepatocytes (82). In a parallel study, infusion of purified CD34⁺ HSC through the portal vein, in patients with chronic liver disease, led to an improvement in serum bilirubin with no associated complications (83). Another study applied granulocyte-colony stimulation factor (G-CSF) based therapy to mobilize autologous HSC in order to bypass the injection of HSC into the portal vein or hepatic artery (84). G-CSF-mediated mobilization of BM cells ameliorated liver fibrosis, therefore, improving both Child-Pugh and model for end-stage liver disease (MELD) scores. Whilst most of the initial studies unanimously rendered hematopoietic cell-based therapies safe and tolerable, the clinical outcome of combining stem cell mobilization and/or infusion of BM precursors remained inconclusive (85, 86).

Considering an ever-increasing demand for organs that outstrips the supply, the cell therapies offered an attractive therapeutic avenue to mitigate liver disease. This led to numerous small-scale clinical

studies, however, inconsistencies in study design, small statistical numbers, and limited readouts made it nearly impossible to assess the efficacy of cell therapies in patients with liver cirrhosis (64, 81, 87). This instigated randomized controlled trials to better judge the clinical efficacy of HSC transplantation on the prognosis of the liver disease. Co-administration of BM mononuclear cells and standard medical therapy (SMT) resulted neither in the proliferation of hepatocytes nor an improvement of liver function when compared with the SMT alone, in a randomized controlled trial involving 58 patients with decompensated alcoholic liver disease (88). A more recent multicenter phase-2 clinical trial aimed at combining G-CSF administration with a repeated infusion of CD133⁺ HSC in 81 patients with compensated liver cirrhosis (89). The combinatorial therapy failed to yield any improvement in liver functionality (as measured by the MELD score) or to ameliorate fibrosis as compared with either the SMT or administration of G-CSF alone. Indeed, patients treated with the combinatorial therapy were found at a higher risk of developing adverse events such as ascites. Unlike the smaller case studies, two major clinical randomized controlled trials found no evidence to support any direct role of BM-derived cells in liver reparation/rejuvenation.

The disparity between preclinical and clinical findings raises an urgent need to revisit the data acquired from the animal experiments and to perform definite and unambiguous analyses to reveal the underlying cellular sources for regenerating adult vasculature. Alongside, it remains to be assessed whether different pathological perturbations require distinct regenerative programs for the recovery of tissue morphology and function.

1.4. Instructive role of endothelial cells during tumor progression

Tumor progression is a complex multi-step process that revolves around a transformed cell trying to orchestrate a conducive environment to survive and grow into a malignant tumor (Fig. 2). Neoplastic transformation of a cell allows for uninterrupted proliferation (90, 91). To sustain this unrestricted growth and to satisfy ever-increasing nutritional requirements, a tumor must undergo an angiogenic switch wherein tumor cells begin to express an array of pro-angiogenic signals such as vascular endothelial growth factor (VEGF), placenta-like growth factor (PLGF), basic fibroblast growth factor (bFGF), platelet-derived endothelial growth factor (PD-EGF), etc (92). Successful realization of the angiogenic switch permits a tumor to grow beyond the size of 1-2 mm³ (93). In fact, Judah Folkman described tumor cells and associated endothelial cells as a highly integrated ecosystem where the mitotic index of the two populations relies on each other. The dependence of tumor cells on vasculature could be explained as the probability of a tumor cell entering mitosis reduced sharply with increasing distance from the nearest capillary (94, 95). Indeed, the diffusion gradient of oxygen and nutrients makes it obligatory for every cell to reside within 100 μm distance to a blood vessel (96). These observations led Judah Folkman to postulate that by cutting the blood supply, cancer can be starved into remission (93).

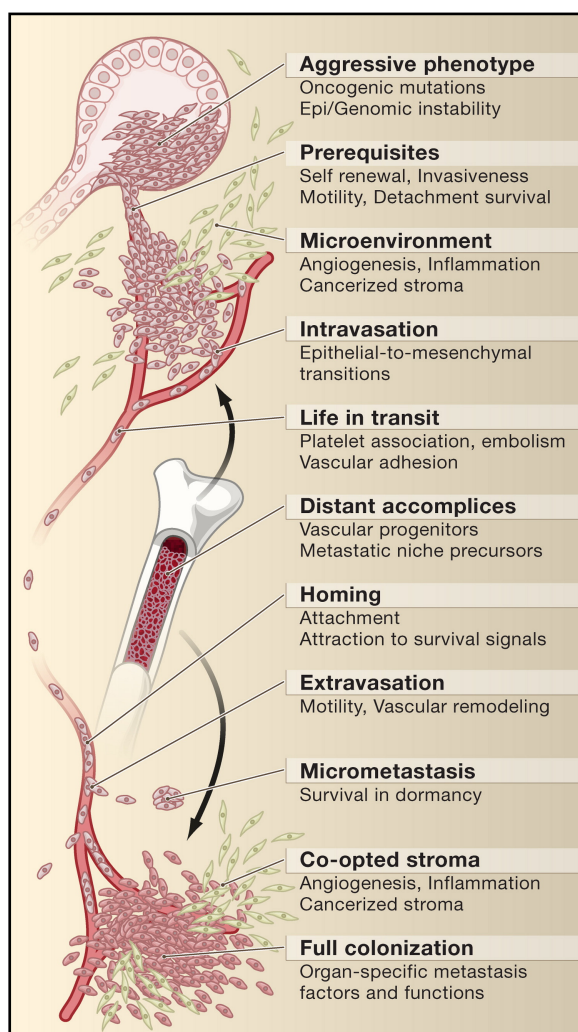


Figure 2. Stages of metastatic progression.

Acquisition of neoplastic characteristics including self-sufficiency in growth signals, evading apoptosis, and limitless replicative potential marks the beginning of a primary tumor. This benign tumor eventually starts to invade into the underlying basement matrix, assembles a conducive microenvironment, and secretes a wide array of inflammatory cytokines, which promotes a systemic hematopoietic response. Tumor cells, either by undergoing an epithelial-mesenchymal transition or by the means of collective migration enter into the circulation. By association with platelets and mesenchymal cells, tumor cells evade anoikis, immune cell-mediated killing, and shear stress to survive in circulation. Subsequently, circulating tumor cells attach and transmigrate through the endothelium of a distant organ. Extravasated cells face a hostile foreign environment, which often forces them to enter into a state of dormancy wherein tumor cells co-opt in the vicinity of vascular cells. Eventually, tumor cells fabricate a favorable local stroma to favor awakening of the dormant tumor cells and grow into a lethal metastasis. Most, if not all, steps of the metastatic cascade are rate-limiting in nature and therefore, in all likelihood, occur in parallel rather than sequentially as predicted initially. Adapted with permission from (97).

1.4.1. Discovery of VEGF/VEGFR

Judah Folkman's hypothesis that "anti-angiogenesis" could possibly treat cancer and neovascular diseases marked the beginning of a new chapter for the field of vascular biology. With a great deal of enthusiasm, researchers across the globe investigated different molecular signals that could either promote or restrict neovascularization. In 1983, Senger and coworkers described Vascular Permeability Factor (VPF) as a soluble factor in the conditioned media of a guinea pig tumor cell line (98). The authors' observation that "as little as 200 ng (5×10^{-12} mole) of the purified material increased vascular permeability to a degree equivalent to that induced by 1.25 μg (4×10^{-9} mole) of histamine" was revolutionary and highlighted a very potent induction of vascular permeability by VPF. Eventually, in 1989, two independent research groups isolated and cloned Vascular Endothelial Growth Factor (VEGF) that closely mimicked molecular characteristics of VPF (99, 100). Interestingly, VEGF exhibited both endothelial mitogenic and vessel permeability-enhancing activity as compared with other EC mitogens such as bFGF. Further efforts were made to characterize different isoforms of VEGF arising

from alternative exon splicing, of VEGF (especially the most common isoforms - VEGF₁₂₁, VEGF₁₆₅, VEGF₁₈₉, and VEGF₂₀₆). Similar to the native VEGF, VEGF₁₆₅ is a soluble heparin-binding mitogenic signal and the most common isoform reported in different physiological and pathological conditions (101). In contrast to higher molecular weight isoforms, VEGF₁₂₁ lacks the heparin-binding domain and manifests highly tissue diffusible characteristics (102). The presence of a heparin-binding domain allows VEGF to bind to the extra-cellular matrix which can be rapidly processed by proteases such as plasmin and MMP3 (103). VEGF processing at the carboxyl terminal results in the diffusible form of matrix-bound VEGF.

Soon after the discovery of VEGF, two highly homologous receptor tyrosine kinases – VEGFR1 and VEGFR2 were identified as the key surface receptors through which VEGF exerts its physiopathological effects (104, 105). VEGFR1 and VEGFR2 were both predominantly expressed by the cells of blood vessels. VEGFR2, however, displayed a much higher affinity to the ligand as compared with VEGFR1 and therefore, was designated as the primary signaling receptor promoting EC mitogenesis and vascular permeability (106). In response of VEGF binding, VEGFR2 undergoes homodimerization and autophosphorylation to initiate a cascade of downstream signaling events (107). VEGF/VEGFR signaling facilitates neoangiogenesis via promotion of tube formation ability and invasiveness of EC, production of extra-cellular matrix, and by inducing supportive survival signals in newly-formed blood vessels (108). Additionally, VEGF also activates a plethora of matrix modulators such as plasminogen, collagenases, matrix metalloproteases to remodel the basement membrane, thereby, releasing a variety of growth factors (107, 109).

1.4.2. Rise of anti-VEGF as the first stroma-targeting therapy

Following neoplastic transformation, the rapid proliferation of tumor cells results in an intratumoral hypoxic core (110). To alleviate hypoxia, cancer cells frequently express high levels of VEGF to attract EC from the neighboring blood vessels, and to promote active sprouting angiogenesis (111). Indeed, hypoxia-inducible factor (HIF) was identified as a major transcriptional activator of VEGF gene expression and elevated levels of HIF1 α were found to positively correlate with tumor progression and invasion (112-114). Concomitantly, VEGF mRNA overexpression was reported for the majority of cancer entities, and oftentimes, correlated with intratumoral vessel density, tumor invasiveness, and overall clinical prognosis (115, 116). Keeping these observations in mind, researchers from Napoleone Ferrara's laboratory developed a monoclonal antibody A.4.6.1 to recognize all biologically active isoforms of VEGF (117). As expected, VEGF-neutralizing antibody suppressed the growth of human tumor xenografts in a dose-dependent manner, providing the first proof-of-principle validation for the "anti-angiogenesis" hypothesis of Judah Folkman. Subsequently, A.4.6.1 was humanized and is today referred to as Bevacizumab (118).

Bevacizumab was initially tested as a monotherapy in a randomized, double-blind, phase 2 trial with 116 patients having metastatic renal carcinoma in a dose-escalation study (119). Despite providing a

significant disease progression-free survival (PFS) benefit as compared with the placebo-administered group, Bevacizumab failed to prolong overall survival (OS). Following this initial set back, Bevacizumab was assessed in combination with the standard chemotherapy (IFL; irinotecan, bolus fluorouracil, and leucovorin) in a phase 3 study with much larger number of previously-untreated metastatic colorectal cancer patients (120). In combination with IFL, Bevacizumab not only improved PFS but also prolonged overall survival of patients by approximately 5 months (30%) as compared with the control arm. This resulted in the US FDA approval for the first anti-angiogenic therapy for previously untreated metastatic colorectal cancer patients in 2004 (121, 122). Subsequent studies revealed clinical benefits of Bevacizumab to the patients of different cancer types. So far, Bevacizumab has received more than 10 FDA approvals for six cancer entities including cervical, colorectal, non-small cell lung, ovarian, renal cell cancer, and glioblastoma multiforme (108). Till date, more than two million patients have been treated with Bevacizumab, making it one of the most widely used agents in the field of oncology (106).

Clinical introduction of Bevacizumab as a first-line treatment for metastatic colorectal cancer paved the path for the development of numerous therapeutic strategies to target VEGF/VEGFR signaling including multiple receptor tyrosine kinase (RTK) inhibitors (Axitinib, Regorafenib, Sorafenib, Sunitinib, etc.), antibody-mediated targeting of VEGFR2 (Ramucirumab) and VEGF (Ranibizumab), recombinant fusion protein mimetic to capture VEGF (Aflibercept), and anti-VEGF aptamer (Pegaptanib) (123, 124). Although, most agents provided a PFS advantage as monotherapy, they failed to yield a long-term OS benefit (125). Yet, in combination with chemotherapy, anti-angiogenic drugs yielded overall survival benefits ranging in orders of weeks to months (50, 126). These clinical observations were somewhat paradoxical. How did the chemotherapeutic drugs reach cancer cells in the absence of blood vessels? This paradox was partly explained by the concept of “vessel normalization” by Rakesh Jain (127). Often, tumors secrete a plethora of pro-angiogenic signals to stimulate uncontrolled vascular expansion, thereby resulting in tortuous vessels that are chaotic and not fully functional. Following the administration of anti-angiogenic therapy, some of these abnormal vessels are pruned to yield a relatively better-perfused normalized intratumoral vasculature. Treatment with anti-angiogenic therapies can therefore enhance the efficacy of chemotherapy by boosting drug delivery (128, 129). Concomitantly, in preclinical studies, application of judicious amounts anti-VEGF or anti-VEGFR2 therapy resulted in the pruning of leaky and immature vessels (130). These morphologically ‘normal’ vessels were indeed better perfused and manifested lower interstitial fluid pressure, reduced intratumoral hypoxia, and elevated delivery of macromolecules (131).

Despite successful preclinical evaluation, low-dose administration of anti-VEGF/VEGFR therapies in clinics unexpectedly resulted in sustained reduction in the uptake of cytotoxic and targeted therapy (132, 133). Unlike preclinical experimentation, calibrating the regimen of antibodies targeting VEGF/VEGFR posed a big challenge for clinicians. Eventually, the first clinical proof-of-concept demonstration for vessel normalization was shown in phase I clinical trial with glioblastoma patients treated with cediranib (a small molecular RTK inhibitor against pan-VEGFR) (134). High-resolution

magnetic resonance imaging (MRI) illustrated that cediranib administration rapidly normalized vessels as marked by reduced leakiness and alleviation of local edema (135). Yet, the normalization effect of cediranib was transient and was limited to a few weeks. A randomized phase III clinical trial comparing cediranib, either as a monotherapy or in combination with lomustine versus lomustine in a cohort of patient with recurrent glioblastoma failed to meet its primary endpoint criteria of PFS and OS prolongation (136, 137). Mechanism-based future studies will answer the dichotomy between results from preclinical and clinical experimentation and hopefully, shed more light on the concept of vessel normalization and how to best combine anti-VEGF/VEGFR therapies with cytotoxic chemotherapy.

1.4.3. Second generation anti-angiogenic therapy

Even though VEGF/VEGFR-targeting drugs became first clinically-accepted anti-stroma therapy for multiple cancer entities, they largely failed to achieve the expected benefit of starving cancer to death (138). By curbing sprouting angiogenesis, anti-VEGF/VEGFR therapies leave behind a normalized vascular network that could successfully sustain tumor growth (50, 139). Subsequent global research efforts were made to identify molecules that can impact the later stages of vessel remodeling and maturation, and targeting such factors could potentially synergize with anti-VEGF/VEGFR therapies. The Angiopoietin/Tie signaling is one of the prominent regulatory circuits that control vessel maturation (51). While the constitutive Ang1-Tie2 signaling axis maintains blood vessels in quiescence, Ang2, a contextual agonist, can destabilize established vessels to facilitate sprouting angiogenesis (140, 141). Unlike VEGF, Ang2 is almost exclusively expressed by endothelial cells and acts in an autocrine manner to mediate responsiveness of EC to any external challenge such as inflammation (142-144). Indeed, the gene expression of Ang2 is often found upregulated in tumor-associated vessels (141, 145). These observations presented Ang2 as a very promising therapeutic target which was hypothesized to synergize with anti-VEGF/VEGFR therapies, primarily attributed to their distinct roles during different stages of pathological vascular growth and maintenance (146).

Ang2-neutralizing drugs effectively suppressed the growth of human tumor xenografts, thereby bolstering clinical aspects of anti-Ang2 therapies (147, 148). Remarkably, the administration of anti-Ang2 drugs could prevent VEGF-stimulated neoangiogenesis in a cornea pocket experiment. Mechanistically, Ang2 neutralization resulted in a sharp decline in the number of proliferating EC and subsequently increased the count of apoptotic tumor cells. Experiments in Ang2-deficient mice revealed a crucial role of Ang2 during initial stages of tumor development, whereas Ang2 was found largely dispensable for growth of established tumors (149). Likewise, Double Anti-Angiogenic Protein, a chimeric trap to quench VEGF and angiopoietins, effectively delayed tumor growth and negated safety concerns related to blocking of constitutively expressed Ang1 (150). Trebananib, a peptibody interfering with interactions of Ang1 and Ang2 and their cognate receptor Tie2, in combination with chemotherapy successfully prolonged PFS for patients with recurrent ovarian cancer (151). Unfortunately, the PFS benefit did not translate into an advantage in OS (152). Similarly, the addition

of Trebananib to carboplatin and paclitaxel resulted in no improvement of either PFS or OS in patients with advanced ovarian cancer (153). More recently, Vanucizumab, a bispecific monoclonal antibody targeting VEGF and Ang2, failed to show improvement as compared with Bevacizumab group, thereby suggesting no additive benefit of targeting Ang2 as first-line therapy for patients with metastatic colorectal cancer (Clinical trial NCT02141295).

Overall, disappointing results of anti-angiogenic therapies either as monotherapy or in combination with chemotherapy in clinics forced academic and industrial researchers to revisit the underlying rationale for implementing anti-angiogenic therapies and to retrospectively assess putative resistance mechanisms that derailed the original aim of starving cancer to death. It is noteworthy that unlike cancer cell-targeted therapies which are given to a preselected subset of patients, anti-angiogenic therapies are often tested in an unrestricted cohort of patients (131, 154). It is anticipated that the informed selection of patients may likely improve the outcome of anti-angiogenic therapies. Hence, a concerted effort should be made to identify biomarkers that can reliably predict the outcome of a personalized combinatorial anti-stroma therapy.

1.4.4. Beyond angiogenesis, EC-derived signals promote metastasis

Apart from the obvious function of delivering nutrients and oxygen, vessel-lining endothelial cells secrete a plethora of growth factors and trophogens such as CCL2, IL6, IL8, CXCL12, and many more (3). These signals play crucial roles during organogenesis as well as in tissue repair and regeneration (2). Numerous preclinical observations led to postulation of the concept of a vascular niche, wherein EC-expressed and/or -secreted factors generate a conducive microenvironment for tumor progression (155-157). To attain rapid angiogenesis, tumor-associated EC display an increased level of plasticity, which is coupled with remodeling of the underlying tissue matrix. Basement membrane, consisting of laminins, fibronectin, collagens, and hyaluronan, serves as a reservoir for various angiocrine molecules that can rapidly be released by proteases like matrix metalloproteinases (MMPs), a disintegrin and metalloproteinases (ADAMs), etc (158, 159). Under hypoxic conditions, EC exhibited enhanced expression and activity of MMP2 and this resulted in increased cell migration (160). Consistently, the presence of MMP2 and MMP9 mediated the angiogenic switch and intervention with MMP inhibitors could impair induction of angiogenesis, thereby delaying tumor growth (161, 162).

Another fundamental function of blood vessels is regulating the infiltration of immune cells (163, 164). Firstly, EC actively regulate surface presentation of adhesion molecules such as ICAM1, VCAM1, and P-selectin to facilitate immune cell trafficking (165, 166). Secondly, activated EC secrete inflammatory cytokines including type I interferon, IL6, IL8, CCL2, CSF1, thereby orchestrating a coordinated immune response to a challenge like tissue injury and cancer (167, 168). Thirdly, relatively underappreciated, EC express decoy receptors for cytokines which allow to buffer potential surges in circulating levels of cytokines (169, 170). Therefore, endothelium, the largest surface in our body, plays a big role in

regulating hematopoietic response to an acute or chronic perturbation. Notably, intervening with anti-angiogenic therapies manifested in an altered immune milieu. Dual inhibition of Ang2 and VEGF reprogrammed tumor infiltrating macrophages from protumor (M2) to antitumor (M1) state, without major differences in total number of infiltrating leukocytes, therefore, strongly emphasizing on the role of EC beyond a passive barrier (171, 172). Concomitantly, stimulation with recombinant Ang2 led to upregulated expression of CCL2 in HUVECs. Consistently, *in vivo* Ang2-neutralization strongly reduced the number of tumor-infiltrating CCR2⁺ macrophages resulting in a strong survival advantage in combination with low-dose metronomic chemotherapy (173). Mechanistically, autocrine-acting Ang2 induced phosphorylation of STAT3 in EC which in turn, transcriptionally activated the expression of adhesion molecule ICAM1 and secretion of CCL2. Hence, Ang2 acts as a master endotheliospecific regulator of the local immune response and orchestrates an immune milieu for metastatic growth.

Metastasis is the fatal hallmark of cancer, yet, it is an extremely inefficient process with numerous intermediate rate-limiting steps. Primary tumors nurture the secondary organs via tumor-derived signals including extracellular vesicles. In 1889, Stephen Paget described the “seed and soil” hypothesis stating - “when a plant goes to seed, its seeds are carried in all directions; but they can only live and grow if they fall on congenial soil” (174, 175). Likewise, successful colonization of seeded single tumor cells heavily relies on the local microenvironment at a distant organ site (Fig. 3). Vascular cells form an essential component of the metastatic microenvironment (97, 176, 177). Recently, bone marrow EC were reported to facilitate metastatic colonization of disseminated tumor cells by inducing mesenchymal-epithelial transition at a secondary site (178, 179). Mechanistically, physical interaction of FUT3/6 on tumor cells with EC-expressed E-selectin resulted in activation of Wnt signaling and instigated stemness in adhered tumor cells. Further, these metastasis-initiating stem-like cells undertook coordinated growth to colonize in the bone. On the contrary, EC were also reported to express decoy receptor DARC (Duffy antigen receptor for cytokines) which not only reversed the cytokine flux induced due to the presence of growing primary tumor, but additionally kept seeded tumor cells dormant. Physical binding of EC-presented DARC and tumor cell-expressed KAI1 restricted proliferation and induced senescence in tumor cells (180, 181). Therefore, EC-derived signals act as a double-edged sword towards seeded tumor cells.

Notch signaling formulates a communication network during early embryonic vascular development and organogenesis (182, 183). Likewise, activation of notch signaling is frequently observed during tumor development (184). Recently, upregulated expression of activated Notch1 receptor (N1ICD) was reported in EC of the pre-metastatic niche (185, 186). Further, sustained N1ICD expression resulted in induced EC senescence and accompanying pro-inflammatory secretome, enhanced expression of VCAM1, and increased number of infiltrating neutrophils, thereby facilitated metastatic progression. In turn administration of either Notch1- or VCAM1-neutralizing antibody reduced the number of extravasating cells and prolonged survival of mice with ovarian cancer. Likewise, in a model of B-cell lymphoma, tumor-associated EC overexpress the Notch ligand Jag1 which physically binds to Notch receptors on lymphoma cells (187, 188). This direct contact enforces indolent CD44⁺IGF1R⁺Csf1R1⁻ cells

to more invasive CD44⁺IGF1R⁺Csf1R1⁺ cells. Apart from being more aggressive in their growth pattern, altered cells additionally manifested resistance to chemotherapy. Likewise, postsurgical adjuvant inhibition of endotheliospecific Ang2 impeded metastatic growth and altered the immune landscape at the metastatic site to inhibit colonization of disseminated tumor cells (173).

Despite the established role of the vascular niche in setting up a conducive soil to facilitate metastatic colonization, so far, most of the published research has been focused on individual candidate gene approaches and have largely been restricted to angiogenesis-related molecules. The past decade witnessed the emergence of the concept of angiocrine signals and their instructive role during different facets of pathophysiological processes. Going beyond angiogenesis, we have merely explored the tip of the iceberg when it comes to the angiocrine signals and it remains elusive how the angiocrine signals can mediate multi-directional crosstalk with different cellular constituents of the local tissue microenvironment thereby promoting tumor metastasis.

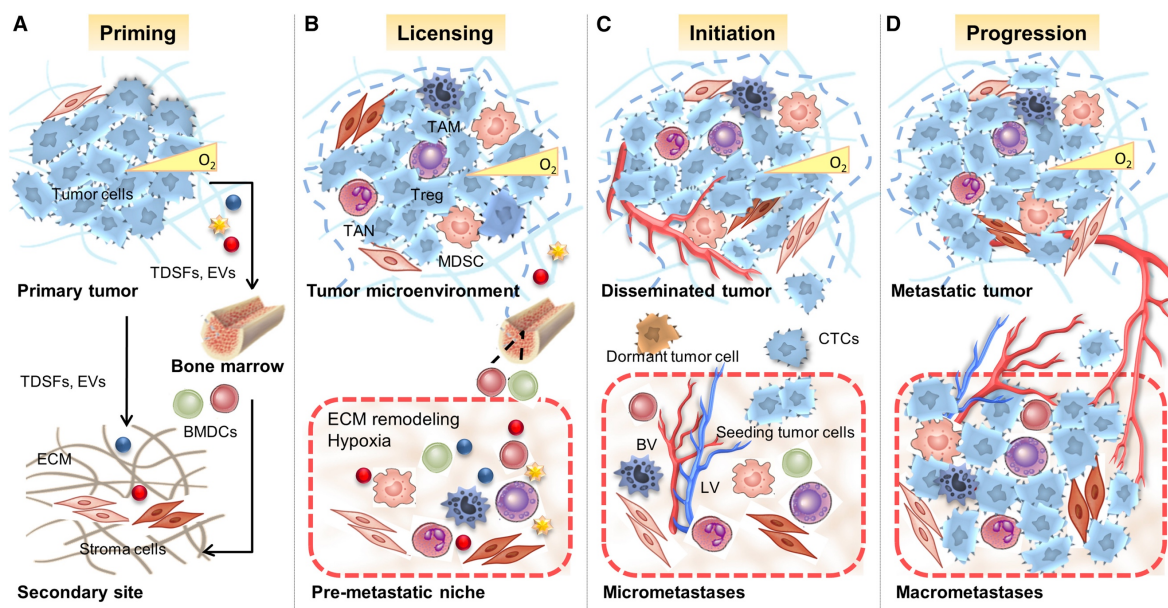


Figure 3. Evolution of the (pre-)metastatic niche during metastasis. (A) During the primary tumor development and growth, tumor cells secrete a plethora of factors including cytokines, and extracellular vesicles, to precondition foreign soil at a distant organ referred to as the pre-metastatic niche. (B) Systemic inflammation triggered due to primary tumor results in pro-tumorigenic suppressive myeloid and regulatory T-cells to infiltrate into secondary sites, thereby further generating a favorable environment for circulating tumor cells. (C) Upon arrival, the survival of single or clustered tumor cells rely on the status of the metastatic niche. In case of a conducive niche, seeded tumor cells colonize and proliferate to generate micrometastases. (D) Eventually, the expansion of seeded tumor cells results in macro-metastases. Adapted with permission from (189).

1.5. Aims of the study

The cells of blood vessels maintain physiological tissue homeostasis and play an instructive role during pathological perturbations. Yet, the cellular source of newly-formed blood vessels in adults and the molecular nature of EC-derived signals during tumor progression remain largely unknown. The present study was pursued to answer the following questions in the field of vascular biology –

- a. What is the cellular source of regenerating liver vasculature? The adult liver in mice regenerates within ten days following PHx, thereby allowing to trace newly-formed blood vessels. By employing myeloablative and non-myeloablative genetic tools, the current study was aimed to unambiguously uncover the origin of regenerating liver vasculature. The data is expected to explain one of the enigmatic controversies in the field - the existence of endothelial progenitor cells and their functional relevance to tissue repair and regeneration.
- b. How does the lung endothelium evolve during metastatic progression? What is the functional contribution of angiocrine signals within the metastatic microenvironment? Employing spontaneously metastasizing tumor models, the current work was aimed to establish the systems map of EC transcriptomic changes during lung metastasis progression. The aim will be to investigate the evolution of lung EC as disease progression and to functionally validate the identified candidate molecules in proof-of-principle gain-of-function and loss-of-function experiments. The generated dataset will be a unique resource to datamine for angiocrine signals that mediate multidirectional crosstalk within the metastatic microenvironment at different stages of disease progression.

2. Results and discussion

2.1. Endothelial cell fitness dictates the source of regenerating liver vasculature

2.1.1. Bone marrow-derived cells incorporate in the irradiation-damaged liver vasculature

To achieve aim 1 of my PhD research work, I systematically investigated the source of endothelial cell (EC) during liver vascular regeneration by employing 2/3rd partial hepatectomy (PHx). In adult mice, the liver is able to restore its original mass and structure within 10 days following PHx (45, 190). Therefore, it uniquely enabled us to trace EC in newly-formed blood vessels of the regenerating liver. Initially, bone marrow chimeras were generated where GFP⁺ Lin⁻Sca-1⁺Kit⁺ (LSK) bone marrow cells, which consist of hematopoietic stem cells and multipotent progenitor cells that are able to fully reconstitute the hematopoietic system, were transplanted into lethally-irradiated syngeneic WT recipients (Fig. 4A). One month later, bone marrow chimeric mice (Fig. 4B) were subjected to PHx to induce liver regeneration and the liver vasculature was analyzed 10 days following PHx. In line with a previous study (75), a fraction of GFP⁺ cells was found incorporated into the liver vasculature (Fig. 4C, upper panel). Surprisingly though, GFP⁺ EC were also detectable in livers of sham-operated mice (Fig. 4C, lower panel; Fig. 4E) suggesting that bone marrow-recruited cells had incorporated into the liver vasculature independent of the PHx-induced regenerative burst, possibly as a result of irradiation-induced vascular damage. The number of GFP⁺ EC in PHx mice was approximately 1.8 times higher as compared with the sham-operated mice (Fig. 4D). Yet, this observation could be attributed either to an increased recruitment of GFP⁺ bone marrow-derived mononuclear cell (BMDMC) or to a higher proliferation of bone marrow-derived cells following PHx. Numerically, to restore the lost liver mass, each remaining EC needs to proliferate 1.66 times post-PHx, suggesting that a higher number of observed GFP⁺ EC could be largely attributed to PHx-induced proliferation of liver EC.

To further dissect transcriptomic differences between resident and bone marrow-derived liver EC in irradiation-preconditioned bone marrow chimeric mice, a microarray analysis comparing YFP⁺ bone marrow-recruited and YFP⁻ resident liver EC was undertaken. Unambiguously, both YFP⁺ and YFP⁻ liver EC exhibited similar expression of multiple EC-specific markers (Fig. 5A), thereby, emphasizing that BMDMC had incorporated as *bona fide* liver EC post-irradiation. However, the bone marrow-derived EC retained expression of a few stem / myeloid-progenitor cell-specific genes (Fig. 5A), possibly indicating their cell of origin. In line with previous reports (191, 192), *Prom1* (CD133) was found enriched in the YFP⁺ liver EC as compared with the resident YFP⁻ liver EC. Further, the bone marrow-derived EC showed similar expression of cell cycle regulatory genes when compared with the resident liver EC (Fig. 5B, C), highlighting that both cell populations possess a similar proliferation capacity. Taken together, these data demonstrate that incorporated bone marrow-derived EC are functionally indistinguishable from the resident liver EC and therefore, both populations can physically contribute to vascular regeneration following a liver injury.

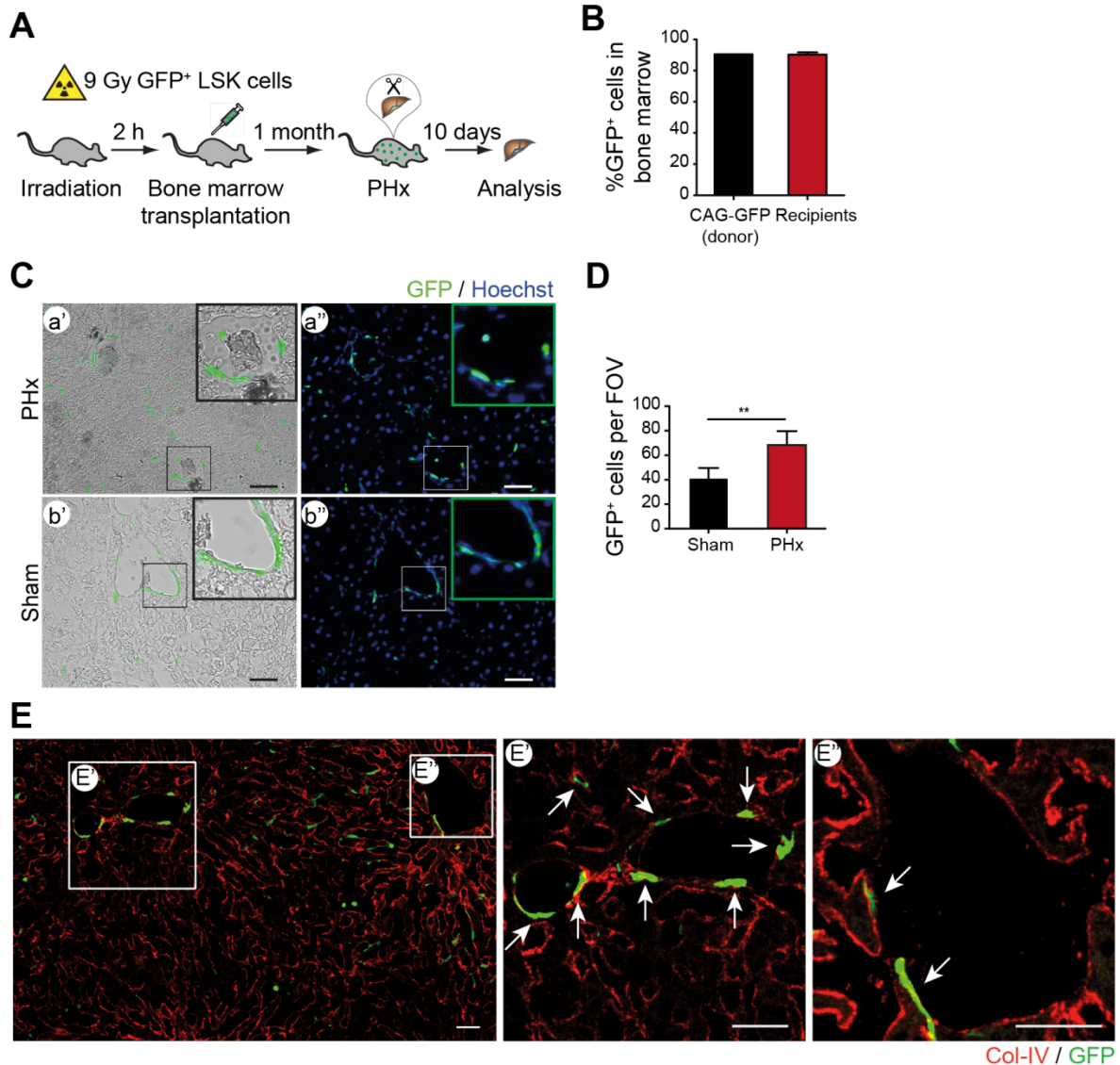


Figure 4. Irradiation-conditioned BM chimeras recruit BMDMC to the regenerating liver. (A) Experimental outline of PHx-induced liver regeneration in irradiation-conditioned GFP⁺ bone marrow transplanted mice. (B) Whole bone marrow cells were isolated from the CAG-GFP donor mice as well as the recipient mice, and were analyzed by FACS to evaluate the donor chimerism (mean ± SD, $n_{\text{donor}} = 1$ mouse, $n_{\text{recipient}} = 12$ mice). (C) Microscopic analysis of liver sections from sham-operated (lower panel – b', b'') and PHx mice (upper panel – a', a'') shows bone marrow-derived GFP⁺ cells integrated into the liver vasculature. Scale bars, 50 μm . (D) The plot shows the GFP⁺ cell count per field of view in the sham-operated and PHx mice (mean ± SD, $n = 6$ mice). (E) Representative images of liver sections of irradiation-conditioned GFP⁺ bone marrow transplanted sham-operated mice. (E', E'') Zoom-in images illustrating GFP⁺ cells incorporated into the liver vasculature. Arrows indicate GFP⁺ EC. Scale bars, 100 μm . **, $P < 0.01$ (two-tailed Student's *t* test).

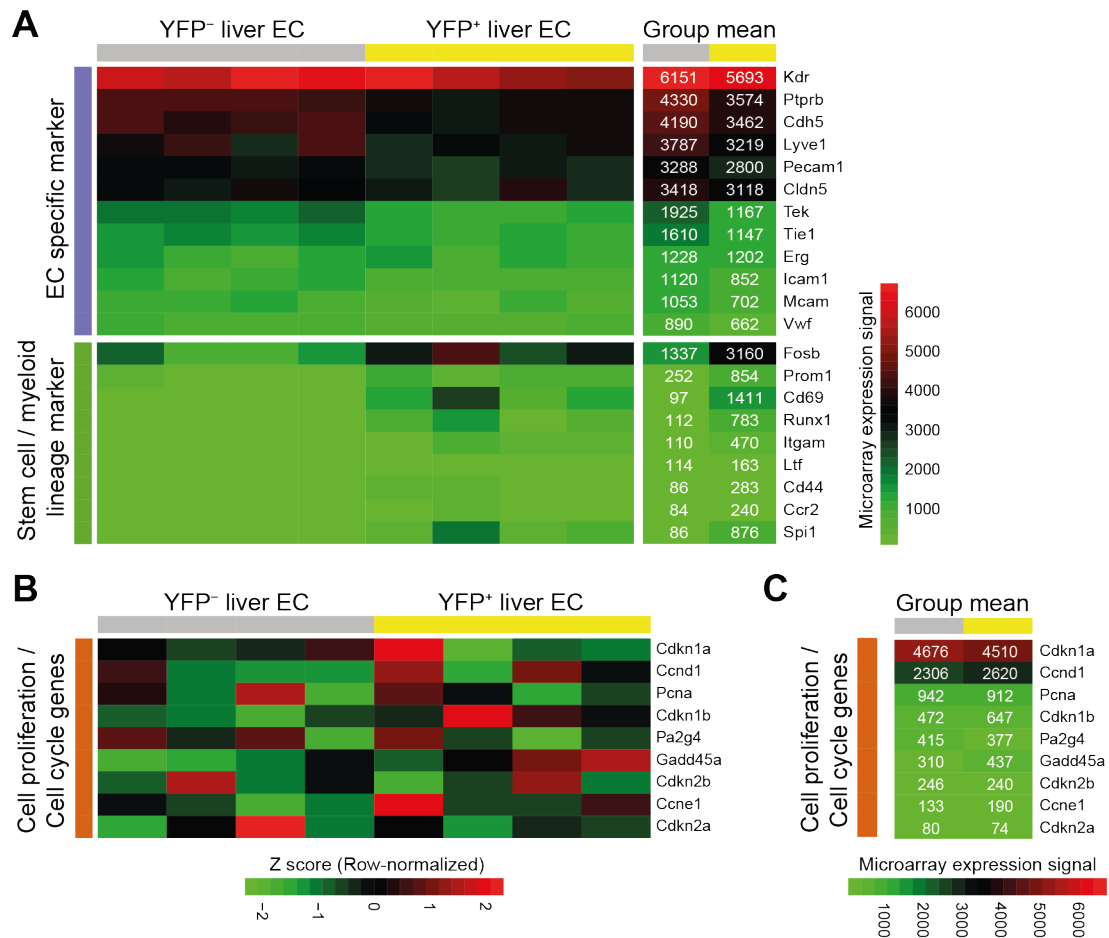


Figure 5. Bone marrow-derived EC are functionally indistinguishable from resident liver EC. (A) Microarray-based gene expression analysis of YFP⁻ resident liver EC and YFP⁺ bone marrow-derived liver EC was performed. Group mean heatmap shows the average of biological replicates (n = 4 mice). (B) The heatmap represents expression of cell cycle regulatory genes. (C) Group mean heatmap shows the average of biological replicates (n = 4 mice).

The majority of previous studies investigated the contribution of BMDMC in irradiation-conditioned bone marrow chimeric mice (54, 69, 193) and had concluded a strong contribution of bone marrow-derived cells to the recovering vasculature. However, the effect of irradiation on the liver vasculature has not been taken into consideration. To investigate why irradiation-based conditioning induced incorporation of bone marrow cells into the liver vasculature, WT mice were irradiated with 9 Gy, and a temporal analysis was performed on liver tissue. As early as 2h post-irradiation, strong phosphorylation of histone H2A.X (Ser139), a marker of double-strand DNA breaks, was detected in the nuclei of both hepatocytes and EC (Fig. 6A, B). Based on the phospho-histone H2A.X (Ser139) staining, I hypothesized that the observed DNA damage might result in EC apoptosis. Concurrently, liver EC were found positive for the apoptotic marker cleaved caspase-3 (CC3) following 9 Gy irradiation (Fig. 6C, D). These results are fully in line with a previous study (194), suggesting that EC are sensitive to irradiation exposure.

To further validate our observations, quantitative-PCR (q-PCR) analysis of *Bax*, an apoptotic activator, was performed to compare the effects of irradiation and PHx on liver tissue. In concordance with the immunofluorescence staining, livers of irradiated, but not partially hepatectomized mice, displayed a strong increase in the gene expression of *Bax* when compared with non-irradiated and partially hepatectomized mice (Fig. 6E). Whilst irradiation induced *Bax* gene expression as early as 2 h following whole-body irradiation, mice that underwent PHx never displayed any alteration in the expression of *Bax*, thereby, illustrating underlying differences between the two challenges. The data clearly suggest that irradiation damages liver EC while PHx induces proliferation burst without causing any severe compromise of endothelial health.

Interestingly, *Icam1* expression was highly upregulated in the livers of irradiated mice as compared with the PHx group (Fig. 6F). It was previously demonstrated that apoptotic EC upregulate *Icam1* expression, resulting in enhanced bone marrow-derived cell recruitment and vascular incorporation (195, 196). It was shown that bone marrow-derived cells contributed up to 12% of total EC within macrometastases mediating the angiogenic switch (195). Thus, the results demonstrate that irradiation-induced EC double-strand DNA breaks and apoptosis led to impaired endothelial self-repair. Consequently, transplantation of healthy bone marrow into a pre-irradiated host resulted in BMDMC recruitment and incorporation as *bona fide* liver EC to restore the injured endothelium.

The observed induction of phosphorylated histone H2A.X and cleaved caspase-3 post-irradiation clearly shows that whole-body irradiation had caused catastrophic damage to the liver vasculature, which led to an emergency recruitment and incorporation of bone marrow-derived cells for tissue repair and rejuvenation of organ function. These data hint at a reparative role of bone marrow cells following irradiation damage. More recently, bone marrow-derived monocytic cells were reported to mediate recovery of the nervous system following focal cranial irradiation (197). Similar to our observations in the case of liver, incorporation of bone marrow-derived cells enhanced brain recovery including improved neurocognitive functionality, thereby providing critical regenerative drive following irradiation. Notably, irradiation was reported to cause permanent damage to the bone marrow niche which in turn limits the engraftment potential of infused hematopoietic stem cells (198). Intriguingly, simultaneous infusion of LSK and bone marrow stromal cells remarkably improved the number of functional hematopoietic stem cells and ameliorated irradiation associated side effects such as neutropenia and humoral immunodeficiency. Taken together, the current data, along with recently published reports, strongly emphasize on irrevocable damage caused by irradiation which warrants an emergency response to regain physiological homeostasis. These findings will have crucial implications on cancer patients undergoing stereotactic radiotherapy and/or hematopoietic stem cell transplantation and will warrant further clinical investigation.

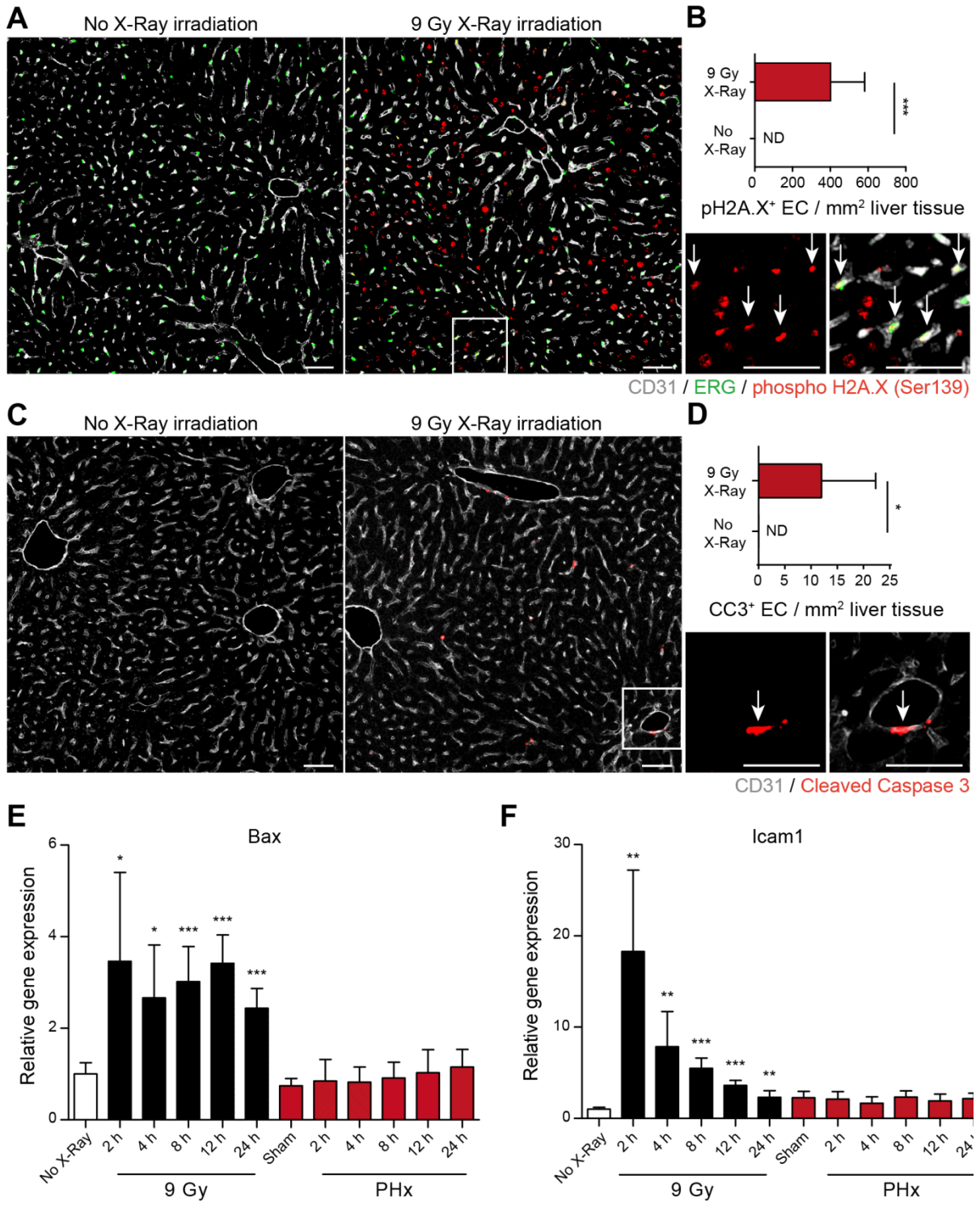


Figure 6. Irradiation-based myeloablation induces EC injury. (A) Representative images of liver sections of control or irradiated mice co-stained with phospho H2A.X (Ser139), CD31 (EC-specific surface marker) and ERG (EC-specific nuclear marker). Zoom-in images are shown on the right. Arrows indicate phospho H2A.X (Ser139) positive EC. Scale bars, 50 μ m. (B) The plot shows the count of pH2A.X⁺ EC per 1 mm² of liver tissue (mean \pm SD, n = 6 mice). (C) Representative images of liver sections of control or irradiated mice co-stained with cleaved caspase 3 (CC3) and CD31 (EC-specific surface marker). Zoom-in images are shown on the right. Arrows indicate CC3⁺ EC. Scale bars, 50 μ m. (D) The plot shows the count of CC3⁺ EC per 1 mm² of liver tissue (mean \pm SD, n = 6 mice). (E, F) Q-PCR analysis of mRNA expression of *Bax* (E) and *Icam1* (F) in livers of mice after irradiation or PHx (mean \pm SD, n = 5-6 mice for each time point). ND = non-detectable; *, P<0.05; **, P<0.01; ***, P<0.001 (two-tailed Student's *t* test).

2.1.2. BMDMC do not incorporate in the intact vasculature during liver regeneration

To circumvent the limitations of irradiation, the contribution of BMDMC to vascular expansion following PHx was further analyzed in non-myeloablative models, (1) using a forward fate mapping approach with bone marrow chimera in *Rag2*^{-/-} *γ c*^{-/-}*Kit*^{W/W^v} animals, and (2) employing a reverse fate mapping approach in *VECad-Cre*^{ERT2} *\times Rosa-YFP*^{f/f} mice. First, YFP⁺ LSK cells were transplanted into *Rag2*^{-/-} *γ c*^{-/-}*Kit*^{W/W^v} mice. These mice lack T and B cells (*Rag2*^{-/-}), NK cells (*γ c*^{-/-}, common gamma chain of the IL2R), and exhibit an impaired self-renewal capacity of hematopoietic stem cells (*Kit*^{W/W^v}). With age, these mice manifest a deficient hematopoietic compartment largely due to reduced HSC numbers in bone marrow. They are thereby able to accept ectopic HSC grafts without any prior irradiation (199) (Fig. 7A). 2 months old *Rag2*^{-/-} *γ c*^{-/-}*Kit*^{W/W^v} mice were engrafted with approximately 5000 YFP-labeled LSK cells, and allowed for the hematopoietic system to attain homeostatic equilibrium (Fig. 7C). Thereafter, bone marrow chimeric mice were subjected to PHx to induce liver regeneration. The regenerated livers of *Rag2*^{-/-} *γ c*^{-/-}*Kit*^{W/W^v} mice showed a similar vascular microstructure as wild-type control mice 10 days post-PHx, suggesting that liver regeneration was not impaired in *Rag2*^{-/-} *γ c*^{-/-}*Kit*^{W/W^v} transgenic mice (Fig. 7B).

To precisely evaluate the contribution of YFP⁺ BMDMC to vascular regeneration, I undertook an indexed analysis where the YFP⁺ EC ratio of both, the resected and the regenerated liver lobes of an individual mouse was analyzed. This allowed us to overcome the differences in bone marrow chimerism and have a definitive assessment of the bone marrow contribution to regenerating vasculature. In contrast to irradiation-conditioned bone marrow chimeras, the percentage of YFP⁺ EC amongst total liver EC was found unaltered before and 10 days after PHx (Fig. 7D), indicating that YFP⁺ BMDMC did not physically integrate into the regenerating liver vasculature following PHx. Overall, these data demonstrate that bone marrow-derived cells did not directly incorporate to the regenerating liver vasculature following PHx under non-vascular-damaging conditions. Nevertheless, the present data cannot exclude a potential role of paracrine signals derived from infiltrating hematopoietic cells towards liver regeneration.

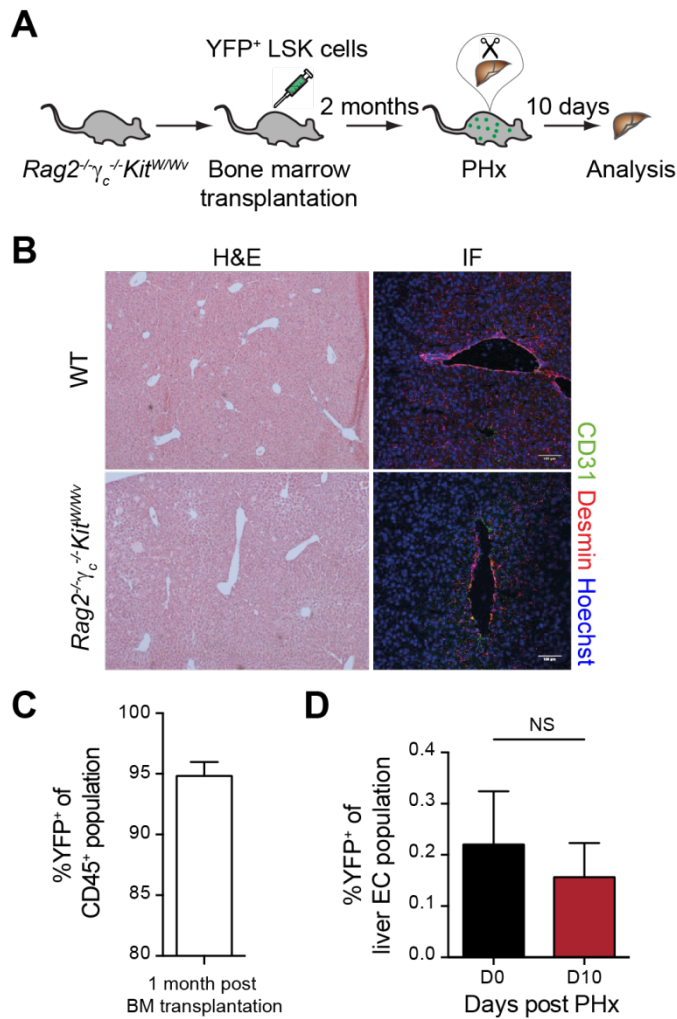


Figure 7. BM cells do not contribute to the regeneration of liver vessels in non-myeloablative chimeric mice.

(A) Experimental outline for transplantation of LSK cells into *Rag2*^{-/-}*γc*^{-/-}*Kit*^{W/Wv} mice. (B) Partial hepatectomy was performed on both WT and *Rag2*^{-/-}*γc*^{-/-}*Kit*^{W/Wv} mice. IHC and IF analysis of the livers of WT and *Rag2*^{-/-}*γc*^{-/-}*Kit*^{W/Wv} mice post-PHx, indicate normal liver regeneration in *Rag2*^{-/-}*γc*^{-/-}*Kit*^{W/Wv} mice. Scale bars, 100 μm. (C) FACS analysis of donor chimerism in CD45⁺ cells from peripheral blood of *Rag2*^{-/-}*γc*^{-/-}*Kit*^{W/Wv} recipients (mean ± SD, n = 4 mice). (D) The percentage of YFP⁺ EC in the livers of *Rag2*^{-/-}*γc*^{-/-}*Kit*^{W/Wv} mice before and 10 days after PHx was analyzed by FACS (mean ± SD, n = 4 mice). NS = non-significant (two-tailed Student's *t* test).

After ruling out the direct contribution of BMDMC in a non-irradiation conditioned preclinical model, the contribution of terminally differentiated resident EC to the regeneration of liver vasculature upon PHx was investigated. To this end, I applied a reverse fate mapping strategy with *VECad-Cre*^{ERT2}*xRosa-YFP*^{β/β} mice, in which transient tamoxifen administration resulted in permanent YFP labeling of the adult vasculature (Fig. 8A). Consistent with a previous report (200), the *VECad* promoter was specifically active in endothelial cells and silenced in the hematopoietic compartment of adult mice. The tamoxifen administration in adult *VECad-Cre*^{ERT2}*xRosa-YFP*^{β/β} mice successfully labeled the liver vasculature with YFP (Fig. 8B) with close to 90% labeling efficiency. However, neither LSK cells in the bone marrow nor mononuclear cells in the peripheral blood were YFP-labeled (Fig. 8B), and exhibited a similar technical background as compared with oil-administered mice. Following a wash-out period of 4 weeks after tamoxifen administration, these mice were subjected to PHx to induce liver regeneration. There were no significant changes in the frequencies of YFP⁺ liver EC while performing an indexed analysis comparing resected and regenerated liver lobes of six individual mice (Fig. 8C).

Additionally, I investigated the proliferation potential of resident liver EC with EdU administration during the angiogenic phase of liver regeneration. Labeling of proliferating cells with EdU revealed YFP⁺ resident EC to be proliferation efficient as they constituted up to 95% of EdU⁺ liver EC population (Fig. 8D). In concordance with bone marrow chimera in *Rag2*^{-/-}*γc*^{-/-}*Kit*^{W/W^v} mice, the data demonstrate that liver vasculature depended on differentiated resident EC during PHx-induced liver regeneration. Likewise, resident EC were previously reported to mediate adult neovascularization following cardiac injury (201) and during tumor progression (202, 203). Interestingly, a subset of liver EC, co-expressing CD157 and CD200, were recently identified as tissue-resident vascular endothelial stem cells that are capable of local clonal expansion and thereby can support neovascularization during liver repair (204). In liver, vascular stem cells reside in the peri-portal region and rapidly expand following an irradiation challenge. Future studies will be required to explore any potential impact of bone marrow cells on the health of liver vascular stem cells. Similar findings have recently been reported during large vessel regeneration in an aortic injury model (205). Thus, under non-vascular-damaging conditions, the vascular regeneration proceeds exclusively by the expansion of preexisting tissue resident EC.

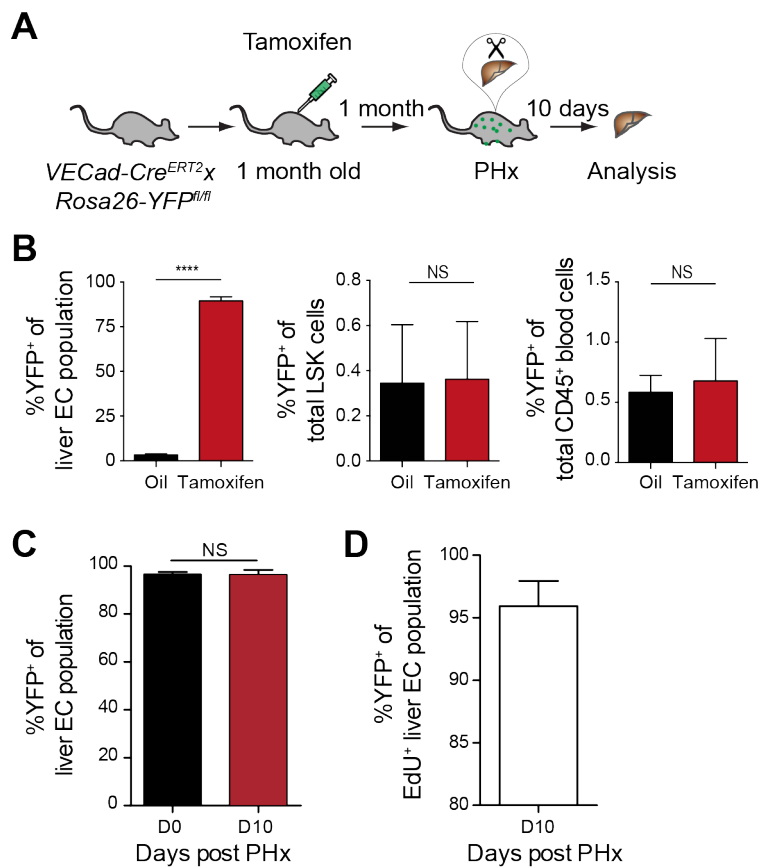


Figure 8. Regeneration of liver vasculature relies on preexisting EC. (A) Experimental outline of the *VECad-Cre*^{ERT2}*xRosa-YFP*^{fl/fl} genetic labeling model. (B) *VECad- VECad-Cre*^{ERT2}*xRosa-YFP*^{fl/fl} mice were transiently administered with either oil or tamoxifen. After a resting period of one month, the frequency of YFP⁺ cells amongst liver EC, LSK cells in the bone marrow, and circulating immune cells in the peripheral blood were analyzed by FACS (mean ± SD, n = 4 mice). (C) The frequency of YFP⁺ EC in livers of the same *VECad-Cre*^{ERT2}*xRosa-YFP*^{fl/fl} mouse before and 10 days after PHx was analyzed by FACS (mean ± SD, n = 6 mice). (D) The proportion of YFP⁺ cells amongst the total proliferated liver EC (as labeled by EdU) post-PHx (mean ± SD, n = 6 mice). ****, P<0.0001; NS = non-significant (*two-tailed Student's t test*).

2.1.3. Liver neovascularization during chronic liver damage

To substantiate the findings from acute PHx-induced liver regeneration in chronic liver damage models, liver neovascularization was further analyzed in *VECad-Cre^{ERT2}xRosa-YFP^{fl/fl}* mice after either repeated intraperitoneal administration of carbon tetrachloride (CCl₄) or a single intravenous injection of empty replication-deficient adenovirus. First, *VECad-Cre^{ERT2}xRosa-YFP^{fl/fl}* mice with YFP-labeled EC were injected thrice a week with either oil or CCl₄ to induce liver injury over a period of four weeks. Repeated treatment with CCl₄ induced a strong increase in plasma amounts of Alanine transaminase (ALT) and Aspartate transaminase (AST) as compared with oil administered mice, indicating a severe liver damage (Fig. 9A). Repeated insults with CCl₄ was reported to result in liver fibrosis which is marked by excessive deposition of extracellular matrix including collagen, and fibrinogen (206, 207). Following a recovery period of two weeks after the last CCl₄ treatment, Sirius red staining was performed on the liver sections of oil- and CCl₄-treated mice, which indeed showed a strong deposition of collagen, an indication of liver fibrosis (Fig. 9B). However, flow cytometry analysis revealed no significant changes in the frequencies of YFP⁺ liver EC between mice treated with either oil or CCl₄ (Fig. 9C), suggesting no incorporation of BMDMC during liver repair.

Next, *VECad-Cre^{ERT2}xRosa-YFP^{fl/fl}* mice with labeled EC were injected with 10¹¹ viral particles of empty replication-deficient adenovirus. This causes an early cytopathic effect on hepatocytes and a secondary adaptive immune response against infected hepatocytes during later stages of the experiment (208, 209). Consistently, adenovirus administration resulted in enhanced plasma ALT/AST values (Fig. 9D), highlighting liver damage over a prolonged time frame. After a recovery period of six weeks, plasma ALT/AST values subsided, thereby displaying a complete clearance of infected hepatocytes and regain of functional homeostasis. Similar to the CCl₄ challenge, flow cytometry analysis revealed no significant alterations in YFP positivity of liver EC when comparing adenovirus-infected with PBS-injected control mice (Fig. 9E). Thus, the data from two mechanistically different chronic liver damage models coherently demonstrate that intact endothelium is self-sufficient for tissue repair and for regaining physiological homeostasis.

It is noteworthy that unlike partial hepatectomy where every cellular population in liver needs to proliferate to regain the lost mass and to re-establish the physiological equilibrium, in the case of chronic damage models, it is primarily hepatocytes that are impacted either metabolically by hepatotoxins or due to immune cell-mediated clearance of adenovirus-infected host cells. Therefore, recovery following a chronic abuse does not involve a large expansion of liver EC numerically, and can possibly be achieved by the proliferation of differentiated remaining cells. Hence, it is not surprising that in a chronically damaged liver, the liver vasculature is self-sufficient and is fully capable of reestablishing functional homeostasis following an injury.

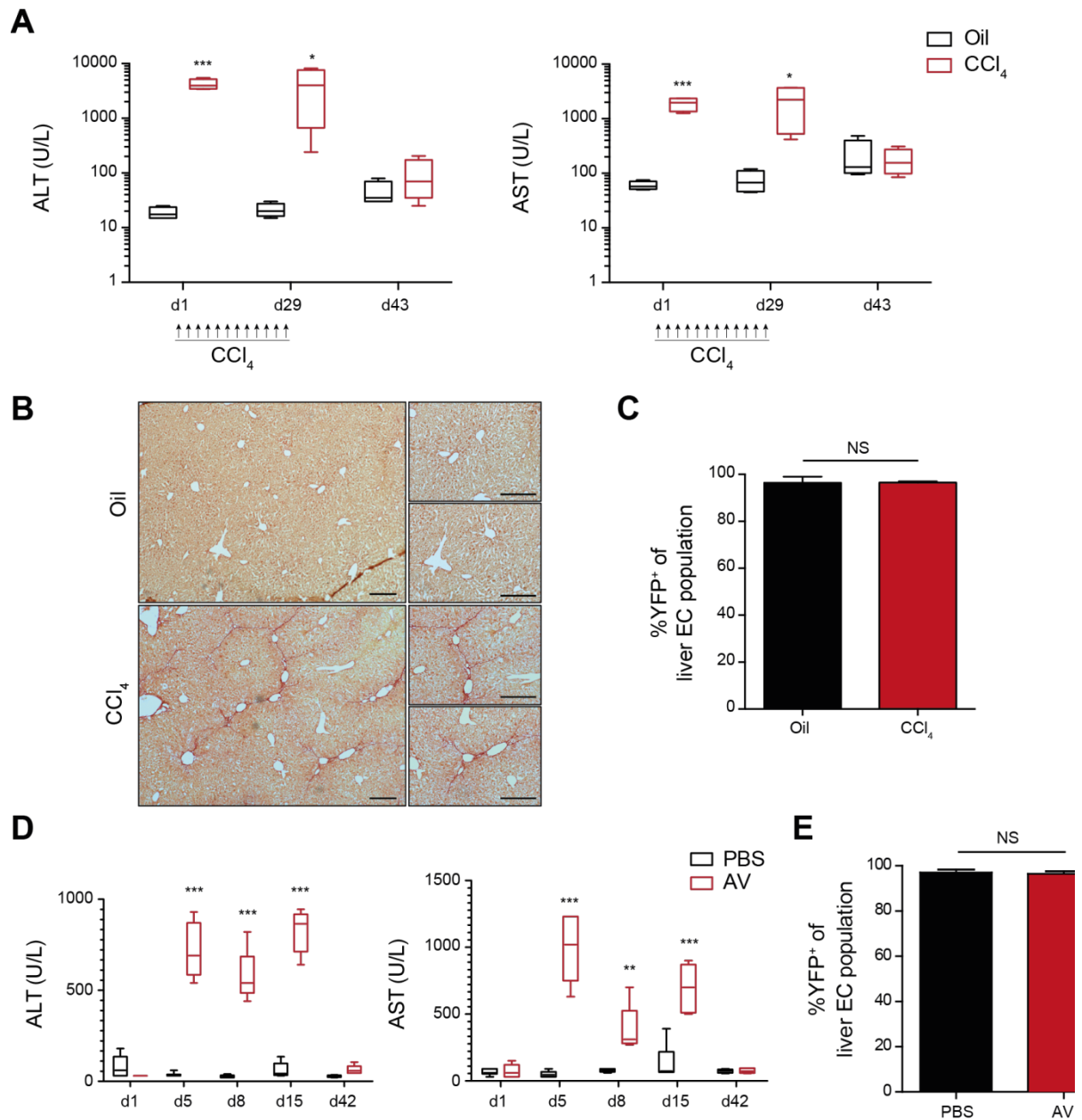


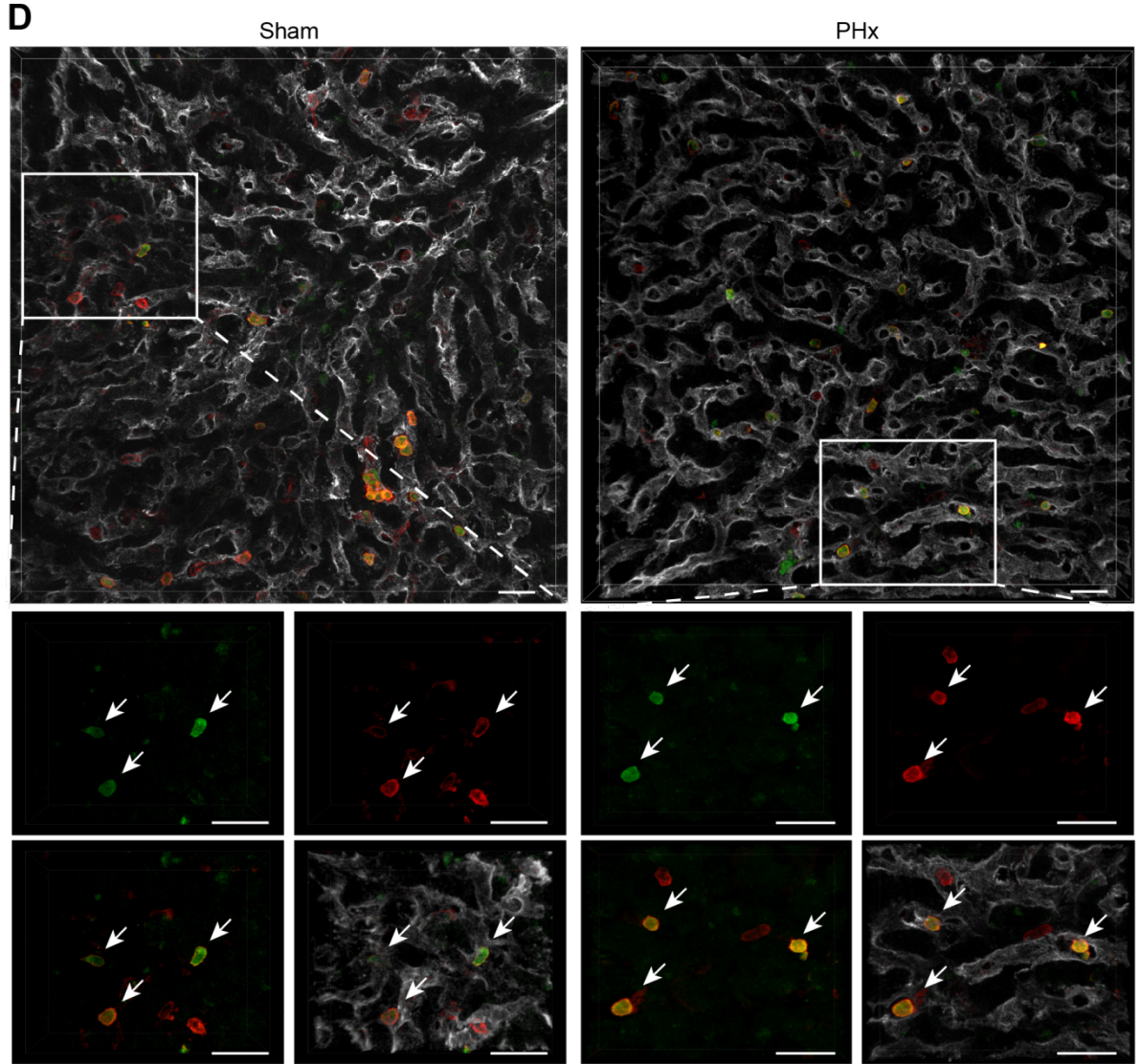
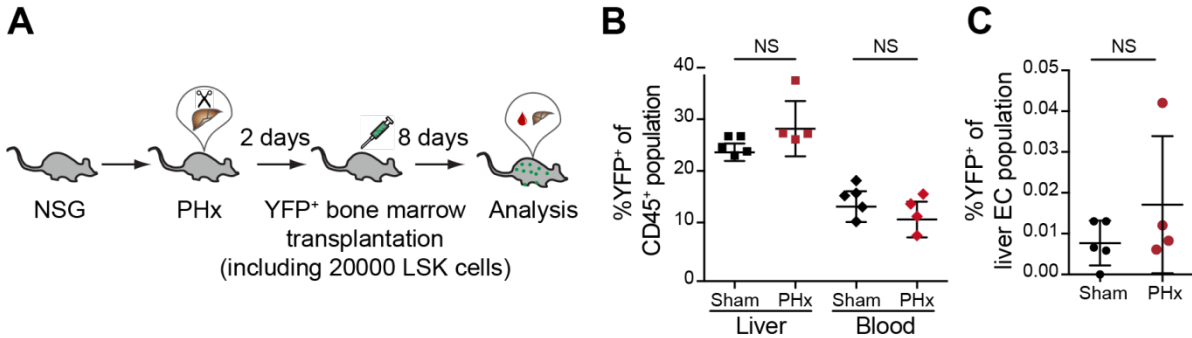
Figure 9. Liver neovascularization during chronic liver injury. (A-C) *VECad-Cre^{ERT2}xRosa-YFP^{f/f}* mice with labeled liver EC were repeatedly administered with carbon tetrachloride (CCl₄) over a period of four weeks. (A) The plots show blood plasma ALT/AST levels over the course of the experiment. (B) Sirius red staining was performed on liver sections of mice treated with either oil alone or with CCl₄. Scale bars, 200 μm. (C) The frequency of YFP⁺ EC in the livers of *VECad-Cre^{ERT2}xRosa-YFP^{f/f}* mice was analyzed by FACS (mean ± SD, n = 4 mice). (D, E) *VECad-Cre^{ERT2}xRosa-YFP^{f/f}* mice with labeled liver EC were intravenously injected with 10¹¹ viral particles of empty replication-deficient adenovirus. (D) The plots show blood plasma ALT/AST levels over the course of the experiment. (E) The frequency of YFP⁺ EC in the livers of *VECad-Cre^{ERT2}xRosa-YFP^{f/f}* mice was analyzed by FACS (mean ± SD, n = 6 mice). *, P<0.05; **, P<0.01; ***, P<0.001; NS = non-significant (two-tailed Student's *t* test).

2.1.4. Bone marrow-based cellular therapies fail to promote liver vascular regeneration

Bone marrow-derived cells have previously been reported to constitute approximately 25% of total liver EC following PHx (74-76). Considering ever-increasing number of patients with chronic liver diseases and a severe shortage of donors for liver transplants, these compelling preclinical observations have stimulated clinical stem cell therapeutic approaches for patients with end-stage liver disease. Initial case studies and proof-of-concept trials with the administration of autologous stem cell grafts showed improvement in liver function and accelerated hepatic regeneration (80, 81). However, a subsequent randomized controlled trial involving 58 patients with decompensated alcoholic liver disease resulted in no additional benefit from autologous bone marrow mononuclear cell transplantation combined with standard medical therapy (SMT) as compared with SMT alone (88). Likewise, a recently-concluded phase 2 clinical trial (REALISTIC) with 81 randomly-assigned compensated liver cirrhosis patients concluded that addition of granulocyte-colony stimulating factor (G-CSF) and autologous hematopoietic stem-cell infusion neither improved liver dysfunction nor ameliorated fibrosis as compared with standard care alone (89).

To recapitulate conditions of the REALISTIC clinical trial in our preclinical mouse models, and to quantitatively assess the physical contribution of bone marrow-based cellular therapies to liver vascular regeneration, I employed either a direct infusion of ectopically-harvested bone marrow cells or administration of G-CSF to mobilize endogenous BMDMC during the angiogenic phase of liver regeneration. To this end, YFP-labeled bone marrow cells, consisting of approximately 20000 LSK cells, were injected via tail vein into the NOD-scid gamma (NSG) mice on day 2 after PHx (Fig. 10A), i.e., prior to proliferation of liver EC. In line with a previous report (210), the NSG mice successfully accepted the allograft as there were approximately 15% YFP⁺ cells amongst total circulating CD45⁺ leukocytes in the peripheral blood on day 10 following PHx (Fig. 10B). Circulating YFP⁺ cells could infiltrate into the liver tissue as they constituted around 25% of the CD45⁺ population in the livers of BM-transplanted NSG mice (Fig. 10B). Yet, when comparing the livers of PHx and sham-operated animals, there was no significant incorporation of YFP⁺ cells among total liver EC (Fig. 10C).

High-resolution immunofluorescence analysis revealed that there were YFP⁺ cells found in the liver tissue, however, they exclusively maintained their hematopoietic identity as marked by CD45 positivity (Fig. 10D, E). Additionally, most of the YFP⁺ cells remained spherical in morphology, thereby negating their possible contribution to the Kupffer cell compartment. Recently, Kupffer cells were reported to be of yolk sac origin with a minimal contribution from bone marrow-derived cells (211, 212). In-depth image analysis failed to identify a significant number of YFP⁺ liver EC in the regenerated liver clearly suggesting that the infused bone marrow cells do not directly contribute to the regeneration of the liver vasculature. These data strengthen the hypothesis that adult vasculature is self-sufficient for liver recovery.



E

	YFP ⁺ (n ± SD)	YFP ⁺ CD45 ⁺ (n ± SD)	YFP ⁺ EC (n ± SD)
Sham	249 ± 66.57	248 ± 65.91	0.8 ± 0.84
PHx	245 ± 64	244 ± 64	0.25 ± 1

Figure 10. Infused BM cells do not incorporate into the regenerating liver vasculature. (A) Experimental outline of PHx-induced liver regeneration in NSG mice. Prior to the angiogenic phase (on day 2 post-PHx), mice were infused intravenously with YFP-labeled bone marrow cells as a regenerative cellular therapy. (B) The frequency of YFP⁺ hematopoietic cells (CD45⁺) in the liver and the peripheral blood of sham-operated and PHx mice was analyzed by FACS (mean \pm SD, n = 4-5 mice). (C) The ratio of YFP⁺ EC in the livers of sham-operated and PHx mice was analyzed by FACS (mean \pm SD, n = 4-5 mice). (D) Representative images of liver sections of sham-operated and PHx mice co-stained with YFP, CD45, and liver EC-specific marker (Lyve-1/Col-IV). Zoom-in images are shown at the bottom. Arrows indicate YFP⁺ cells. All traced YFP⁺ cells were positive for CD45 but negative for EC markers. Scale bars, 25 μ m. (E) Shown are the absolute numbers of YFP⁺ cells, YFP⁺ hematopoietic cells and YFP⁺ EC counted per 1 mm² of the liver tissue of sham-operated and PHx mice (mean \pm SD, n = 4-5 mice). NS = non-significant (*two-tailed Student's t test*).

In order to expand and mobilize endogenous BMDMC, Neulasta (PEGylated G-CSF), a clinically-approved agent for mobilizing hematopoietic progenitor cells (213), was injected in wild type mice on day 2 following PHx (Fig. 11A). There was a strong increase in the number of circulating LSK cells in G-CSF-injected mice as compared with saline-injected control mice (Fig. 11B). Circulating liver EC progenitors were reported to express CD133 (73), and the infusion of CD133⁺ BMDMC could accelerate liver regeneration (75). Yet, no significant expansion or recruitment of CD133⁺ liver EC was observed when comparing PHx with sham-operated mice, following G-CSF administration (Fig. 11C). High-resolution 3D image analysis revealed that CD133 staining in the liver tissue was exclusively restricted to epithelial cells of bile ducts (Fig. 11D). CD133⁺ multipotent stem / progenitors were previously reported to reside in peribiliary glands and give rise to hepatocytes and cholangiocytes to facilitate liver repair (214, 215). However, I could not detect a CD133⁺ fraction of the liver EC in both sham-operated and PHx mice. Therefore, the data negate any possible contribution of mobilized endogenous multipotent progenitor cells to liver vascular regeneration.

Overall, these data recapitulate the observations from the REALISTIC trial as neither direct infusion of bone marrow cells in NSG mice, nor G-CSF-mediated mobilization of progenitor cells in wild-type mice showed any BMDMC contribution to the regenerating liver vasculature. The data clearly suggest that stem cell infusion/mobilization therapies do not physically contribute to the regeneration of liver vasculature in mice with healthy remaining vasculature. Yet, BMDMC might contribute through other mechanisms towards liver regeneration, e.g. by differentiating into other cellular compartments in the liver or by improving liver function via paracrine signals. Additionally, the present data do not allow for the exclusion of any plausible impact of the immune system in defining the success of BMDMC contribution towards liver parenchyma. Future studies involving stringent and mechanistic preclinical experimental approaches will need to address these questions to possibly establish a scientific rationale for bone marrow-derived stem cell therapies to interfere with liver dysfunction.

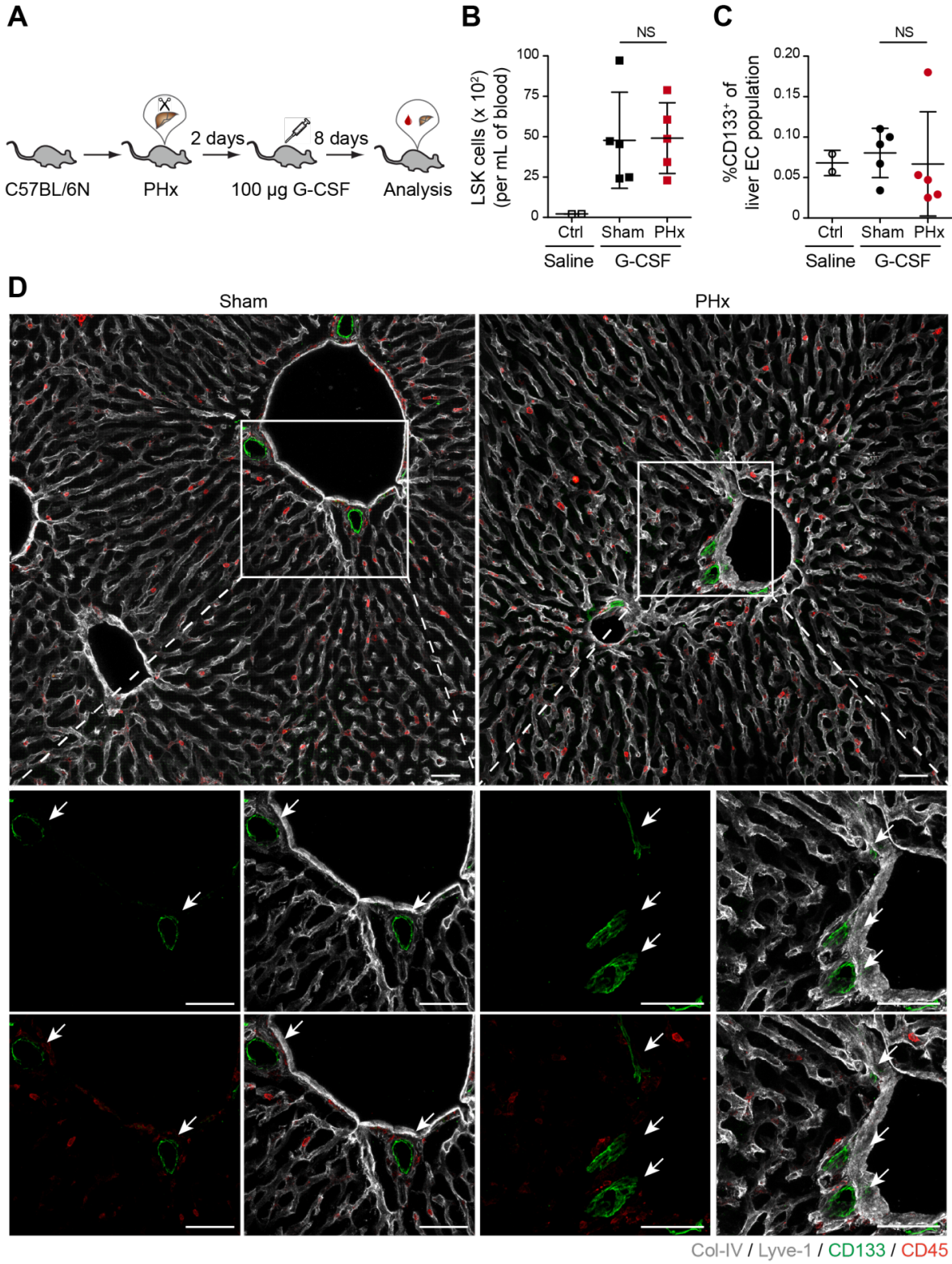


Figure 11. G-CSF mobilized BM cells do not incorporate into the regenerating liver vasculature. (A) Experimental outline of PHx-induced liver regeneration in C57BL/6N mice. Prior to the angiogenic phase (on day 2 post-PHx), mice were injected subcutaneously with 100 μ g G-CSF (as a regenerative therapy) to mobilize bone marrow-derived progenitor cells. (B) The frequency of circulating LSK cells in the peripheral blood of sham-operated and PHx mice was analyzed by FACS (mean \pm SD, n = 5 mice). Saline-injected mice served as controls. (C) The ratio of CD133⁺ EC in the livers of sham-operated and PHx mice was analyzed by FACS (mean \pm SD, n = 5 mice). Saline-injected mice served as controls. (D) Representative images of liver sections of sham-operated and PHx mice co-stained with CD133 (progenitor cell marker), CD45, and liver EC-specific marker (Lyve-1/Col-IV). Zoom-in images are shown at the bottom. Arrows indicate CD133⁺ cells. All traced CD133⁺ cells were negative for CD45 and EC markers. Scale bars, 50 μ m. NS = non-significant (*two-tailed Student's t test*).

2.2. Temporal multi-omics identifies LRG1 as a vascular instructor for early metastatic colonization

2.2.1. Modeling metastatic disease in mouse tumor models

Metastasis is estimated to cause more than 90% of cancer-related mortalities (216). Yet, only 25% of preclinical studies published in 2016 focused on metastasis, and the majority of studies employed primary tumor mouse models (217) (Fig. 12A). For modeling metastasis in rodents, primarily two different strategies have been exploited. First, experimental metastasis where tumor cells are systemically injected to home directly to a targeted organ (Fig. 12B). This allows for assessing the extravasation and colonization capabilities of tumor cells at a predetermined organ site. Second, spontaneous metastasis where tumor cells undergo the natural process of dissemination from a primary tumor, intravasation to enter the circulation, and extravasation to subsequently colonize at a secondary site (Fig. 12B). In the clinics, the majority of cancer patients undergo surgical resection of the primary tumor, and in certain cases, patients develop metastases after long periods of remission (218). Tumor cells can stay dormant and undetected at secondary sites for years and wait for a favorable trigger to eventually outgrow into macrometastases. Spontaneous metastasis models coupled with primary tumor resections truthfully reflect the clinical progression of metastasis; nevertheless, such models are exploited in a very small fraction of preclinical oncology studies (Fig. 12C). Overall, the lack of metastasis-focused research and usage of primitive metastasis models may partly explain why only 5% of oncology therapies were approved against the average 9.6% approval rate for all medical indications between 2006 and 2015 (219, 220).

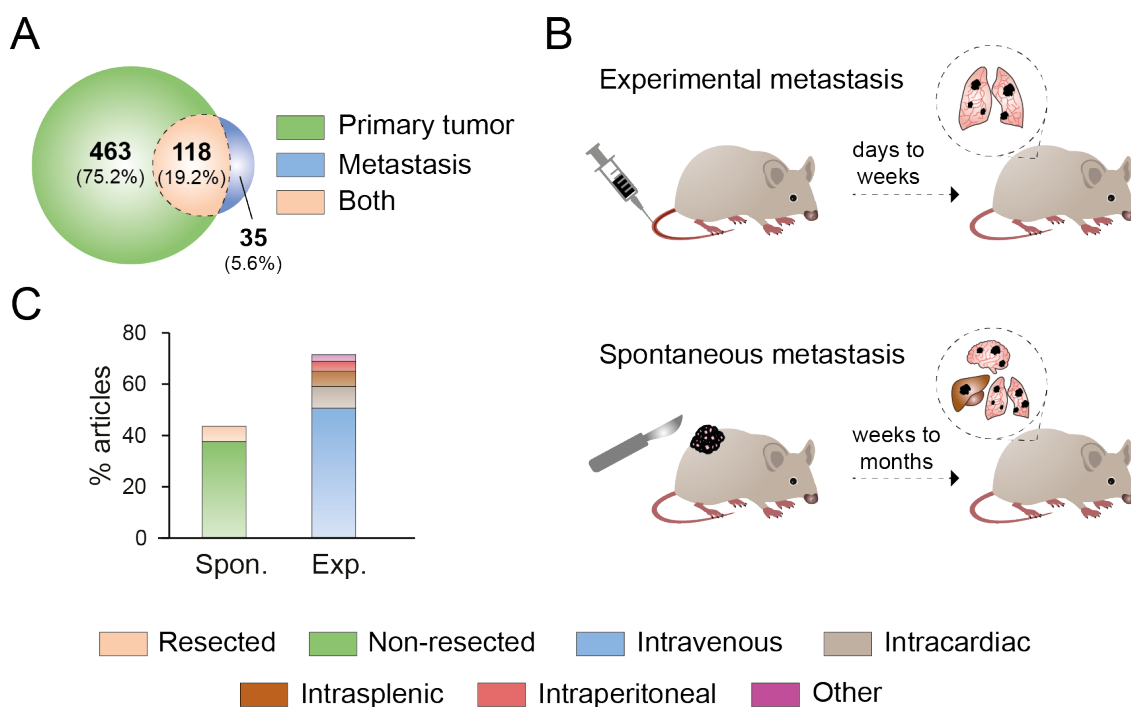


Figure 12. Mouse models to mimic spontaneous metastasis. 949 oncology research articles published between January and August 2016 in the interdisciplinary journals Cell, Nature, Science and the Proceedings of the National Academy of Sciences USA as well as in the cancer-specific journals Cancer Cell, Cancer Discovery, Cancer Research and Oncogene were retrieved and systematically reviewed for mouse tumor experiments. (A) Distribution of articles studying primary and/or metastatic disease ($n_{\text{mouse model}} = 618$). (B) In experimental metastasis models, tumor cells are systemically injected via diverse routes (intravenous (often through the tail vein), intracardiac, intrasplenic or intraperitoneal). These models are characterized by rapid and uniform formation of metastases but only capture late steps of the metastatic cascade (survival in the circulation and metastatic colonization). Spontaneous metastasis models truthfully recapitulate the natural course of metastatic disease, including initial steps such as tumor cell dissemination from the primary tumor. However, long latency may require the surgical resection of the primary tumor to allow sufficient time for metastatic progression. (C) Frequency distribution of different types of experimental and spontaneous metastasis models within the sub-cohort of all metastasis studies ($n_{\text{metastasis}} = 152$). The percentages add up to more than 100% because 23 studies employed multiple metastasis models. Sixty-seven studies utilized spontaneous metastasis models (58 non-resected, 9 resected), and 100 studies used experimental metastasis models (77 intravenous, 13 intracardiac, 9 intrasplenic, 6 intraperitoneal and 2 others).

2.2.2. Transcriptional evolution of lung EC during metastasis

In order to identify molecular changes of EC in the premetastatic and metastatic niche in an unbiased systems biology approach, I employed surgical preclinical metastasis models and transcriptionally profiled lung EC over time. A primary screen was performed by subcutaneously inoculating lung metastasizing tumor cells (Lewis Lung Carcinoma, LLC) in syngeneic immune-competent C57BL/6N mice. In the LLC model, metastatic colonization occurs frequently in lung and lymph nodes and to a lesser extent in diaphragm, liver, and spleen following primary tumor resection. At sequential stages of tumor progression, including control (d0), small primary tumor-bearing (d15), 1 wk post-primary tumor resection (d22), and metastasis-bearing (d36) (Fig. 13A), lung EC were isolated by fluorescence-activated cell sorting (FACS) for surface marker profile $\text{CD45}^{\text{LYVE1}^{\text{PDPN}^{\text{TER-119}^{\text{CD31}^{\text{+}}$ (Fig. 13B). Isolated lung EC were enriched for EC-specific genes as evaluated by quantitative PCR (Fig. 13C).

Total RNA was isolated from the sorted lung EC and used for bulk RNA-sequencing analysis to decipher global gene expression changes in lung EC during metastatic progression. Raw RNA-seq data were initially aligned to the mouse reference genome (mm10) and differential gene counts as normalized to the gene length and overall coverage was calculated per sample. Bulk RNA-seq data were examined for all possible contaminants including genes specific for different lung cell types such as epithelial cells, hematopoietic cells, lymphatic EC, and perivascular mural cells (Fig. 13D). All 16 samples exhibited high endothelial purity as monitored by the gene expression of numerous blood EC-specific genes. Following quality control, genes with Reads Per Kilobase of transcript, per Million mapped reads (RPKM) ≥ 1 in at least one of the samples were considered for further analysis.

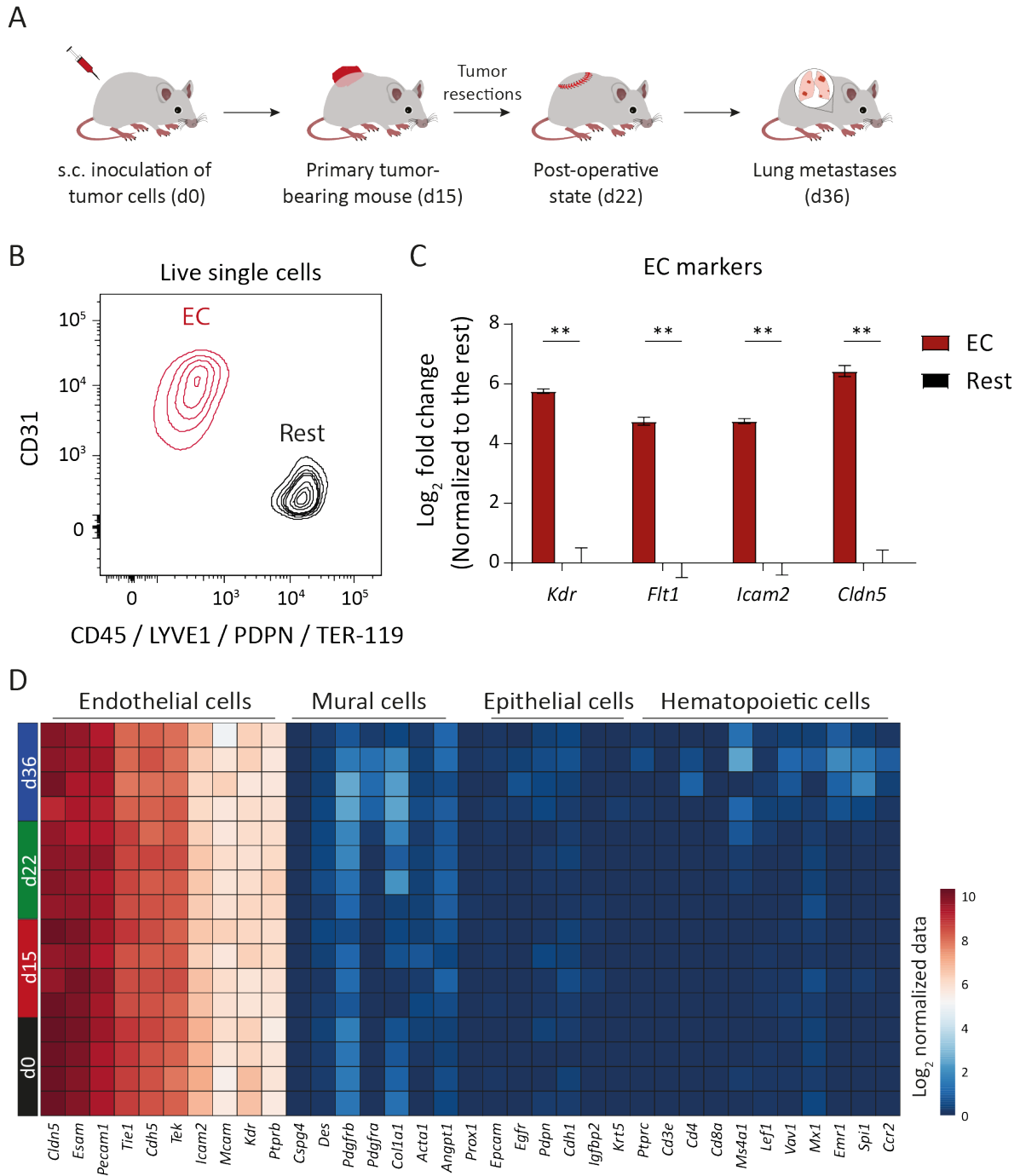


Figure 13. Temporal analysis of lung EC during tumor progression. (A) Schematic depiction of LLC spontaneous metastasis model, in which mice develop lung metastases following primary tumor resection. (B) Lung EC were isolated by FACS sorting. All live single cells were separated into EC (CD31⁺) and the rest of lung cells (CD31⁻CD45⁺LYVE1⁺PDPN⁺TER-119⁺). (C) Shown is the quantitative PCR analysis comparing EC and the rest of lung cells for EC-specific genes (mean \pm SD, n = 5 mice). **, P<0.01 (*two-tailed Mann-Whitney U test*). (D) RNA-seq data were examined for all possible contaminants including mural, epithelial and hematopoietic cells. Shown is the heatmap of Log₂ normalized data.

The principal component analysis revealed close proximity of biological replicates for each time point (Fig. 14A). Relatively wider distribution of d36 samples could be attributed to varying metastatic burden at this time point. With metastatic progression, lung EC manifested an overall transcriptional activation, which resulted in a strong increase in average Log_2 -fold change (FC) (Fig. 14B) and translated in a higher number of significantly upregulated genes at d36 as compared with d0 samples (Fig. 14C). Plotting significantly altered genes as a heatmap revealed distinct stage-specific gene signatures in lung EC as the disease progresses (Figs. 14D).

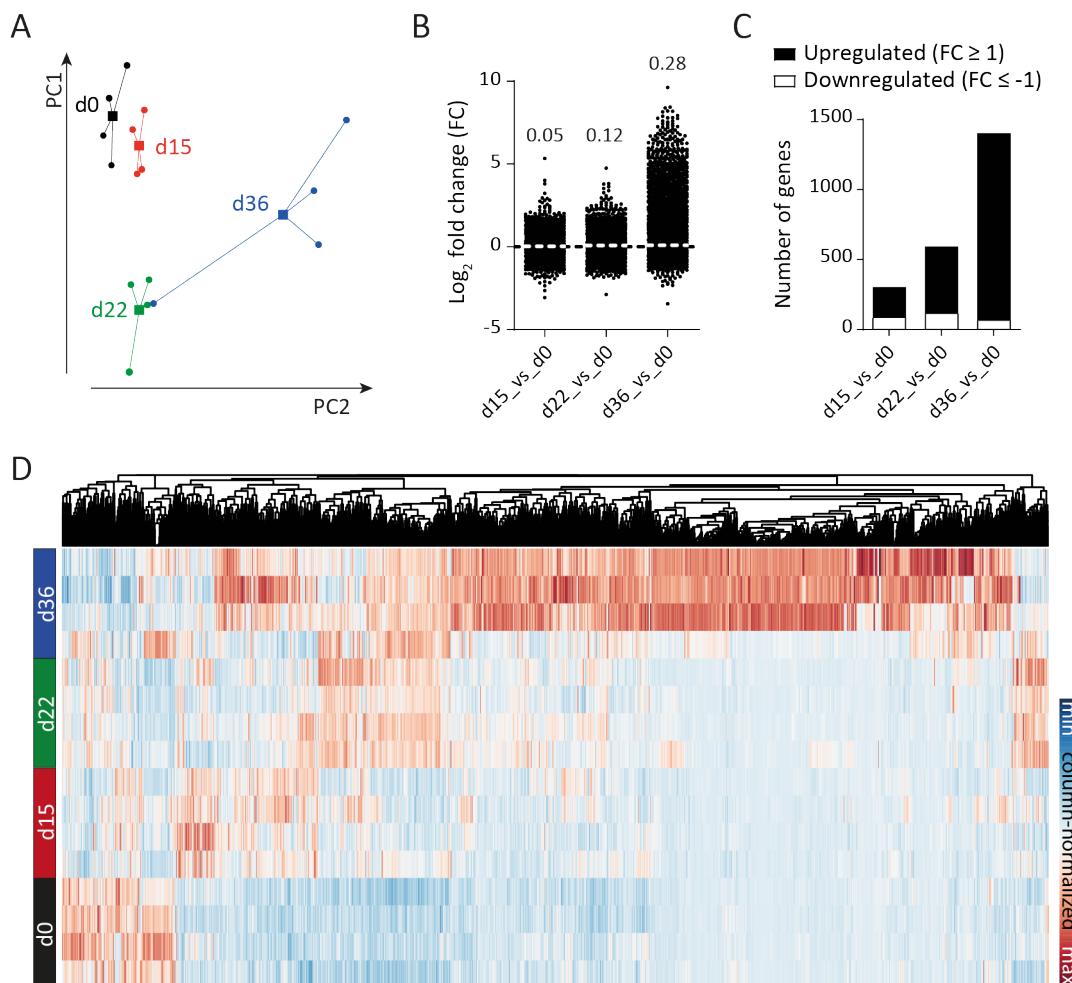


Figure 14. Transcriptomic evolution of lung EC during metastasis. (A) Principal component analysis of RNA-seq data of isolated lung EC ($n = 4$ samples for each time point). Circles and squares denote individual samples and centroid of each group, respectively. (B) Dot plot showing Log_2 fold change (FC) for genes with $\text{RPKM} \geq 1$ in at least one of the samples. The mean FC of all analyzed genes is indicated for each comparison. (C) Bar graph illustrating the number of significantly upregulated (\uparrow) and downregulated (\downarrow) genes in d15 (226 \uparrow , 89 \downarrow), d22 (480 \uparrow , 119 \downarrow), and d36 (1329 \uparrow , 71 \downarrow) lung EC as compared with d0. (D) Heatmap of all significantly regulated genes with $\text{FC} \geq 1$ or $\text{FC} \leq -1$.

To better understand the biological relevance of transcriptional changes in lung EC, gene set enrichment analysis (GSEA) and ingenuity pathway analysis (IPA) were performed. Significantly altered genes at d15 and d36 belonged to hallmark gene sets related to protein secretion, coagulation, inflammatory responses, hypoxia, and cellular proliferation (Figs. 15A, B). The presence of a primary tumor evoked a systemic inflammation (221, 222). This triggered a strong response from lung EC as evidenced by an inflammatory transcriptomic signature of lung EC (Figs. 15C, D).

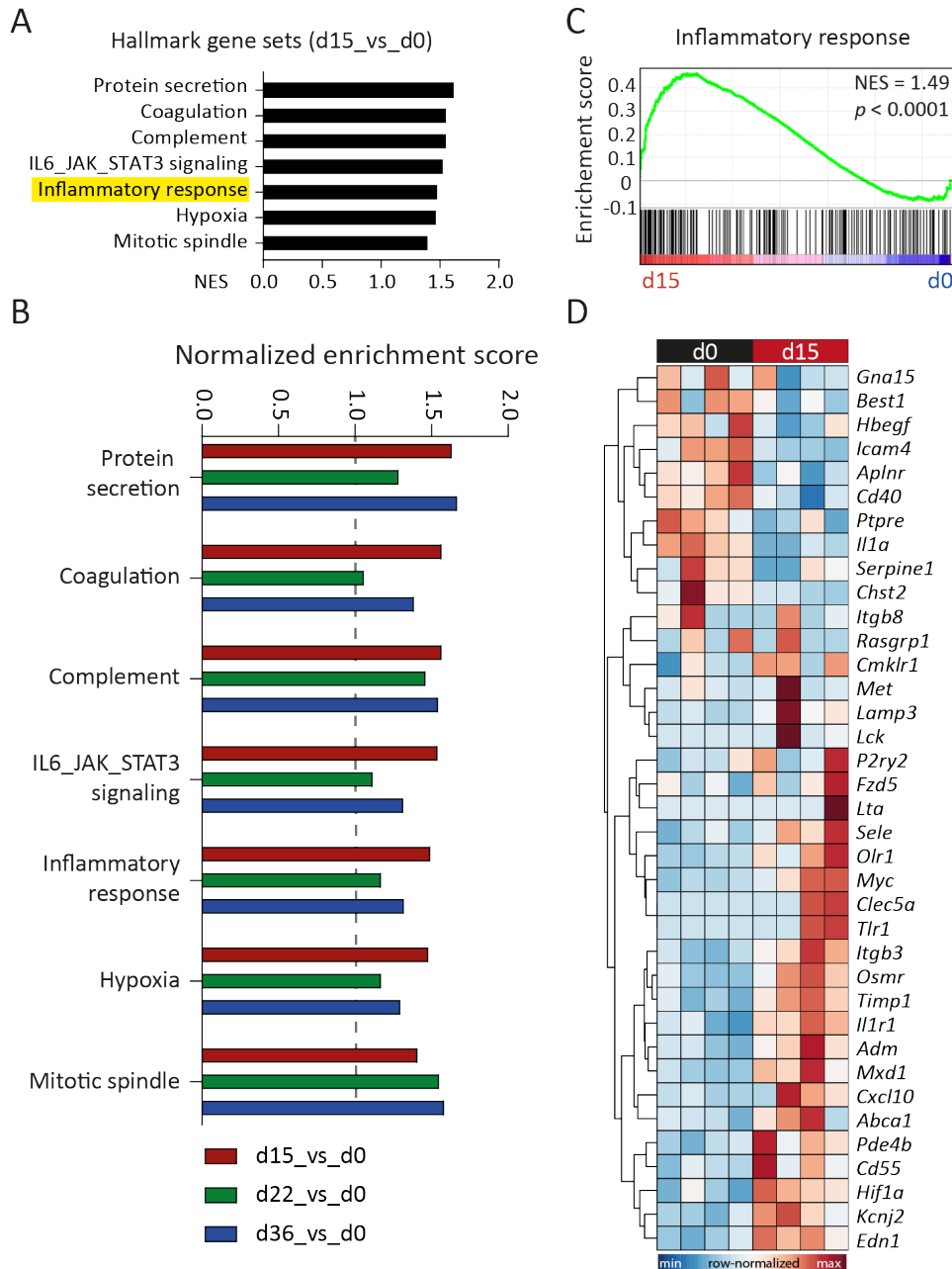


Figure 15. Lung EC show enrichment of genes related to inflammatory responses. (A) Gene Set Enrichment Analysis (GSEA) comparing d15 and d0 data sets. (B) Temporal comparisons of hallmark gene sets. (C) The inflammatory response gene set was found positively correlated with d15 time point. (D) Heatmap highlighting genes in the inflammatory response gene set. NES = normalized enrichment score.

Given that inflammation-related transcriptomic changes were observed in lung EC, a thorough analysis of the immune landscape in the lung was undertaken and correlated with systemic changes induced by the presence of a primary tumor. Infiltrating immune cells were analyzed both qualitatively by immunofluorescence (IF) staining and quantitatively by FACS. IF staining also provided the spatial information concerning the localization of infiltrating leukocytes.

A strong immune cell infiltration, particularly of myeloid cells, was observed in d15 lung tissue as compared with d0 (Figs. 16A, 17A, B). A sharp decline in infiltrating immune cells was observed in d22 specimens (Figs. 16A, 17A, B), suggesting subsided systemic inflammation following primary tumor resection. This was similarly reflected in the inflammatory gene set analysis of lung EC (Fig. 15B). Similar to d15, d36 lung witnessed a strong infiltration of leukocytes (Figs. 16A, 17A, B) with macrometastases outgrowth. Hence, the employed metastasis model truthfully captured the tumor cell-driven systemic alterations including initial myelopoiesis during primary tumor growth, rapid restoration of homeostasis following tumor resection, and finally myeloid cell expansion upon metastatic colonization.

Interestingly, CD11c⁺ antigen-presenting dendritic cells were significantly reduced in d36 as compared with d0 lung samples (Fig. 17A, B). Concomitantly, the population of CD8⁺ cytotoxic T-cells also shrank in d36 lungs as compared with d0 (Fig. 17C, D). These data hint towards an immune-suppressive, referred to the cold, microenvironment in d36 lungs, possibly as a result of growing macrometastases. These observations were in line with previous publications highlighting that the protumorigenic immune-suppressive microenvironment facilitates metastatic progression (223-225).

Surprisingly though, the immune cell infiltration in d36 lung tissue was mostly restricted to the adjacent normal tissue rather than the metastatic nodules (Fig. 16A). Classically, in tumor cell-centric research, scientists and clinicians have compared epithelial tumors to their adjacent tissue for histological, biochemical, and molecular analyses. This is quite justified as epithelial cells acquire distinct genomic and epigenomic traits to become neoplastic in nature. However, stromal cells often do not undergo any genomic or epigenomic alterations and are primarily driven by transcriptional and translational changes. Therefore, the data emphasize that metastasis possibly influenced the vascular compartment in the whole lung and not merely within tumorous regions. Yet, while analyzing the acquired bulk RNA-seq data, it should be kept in mind that the effects induced by the direct contact of tumor cells will possibly be diluted amongst the rest of the lung EC.

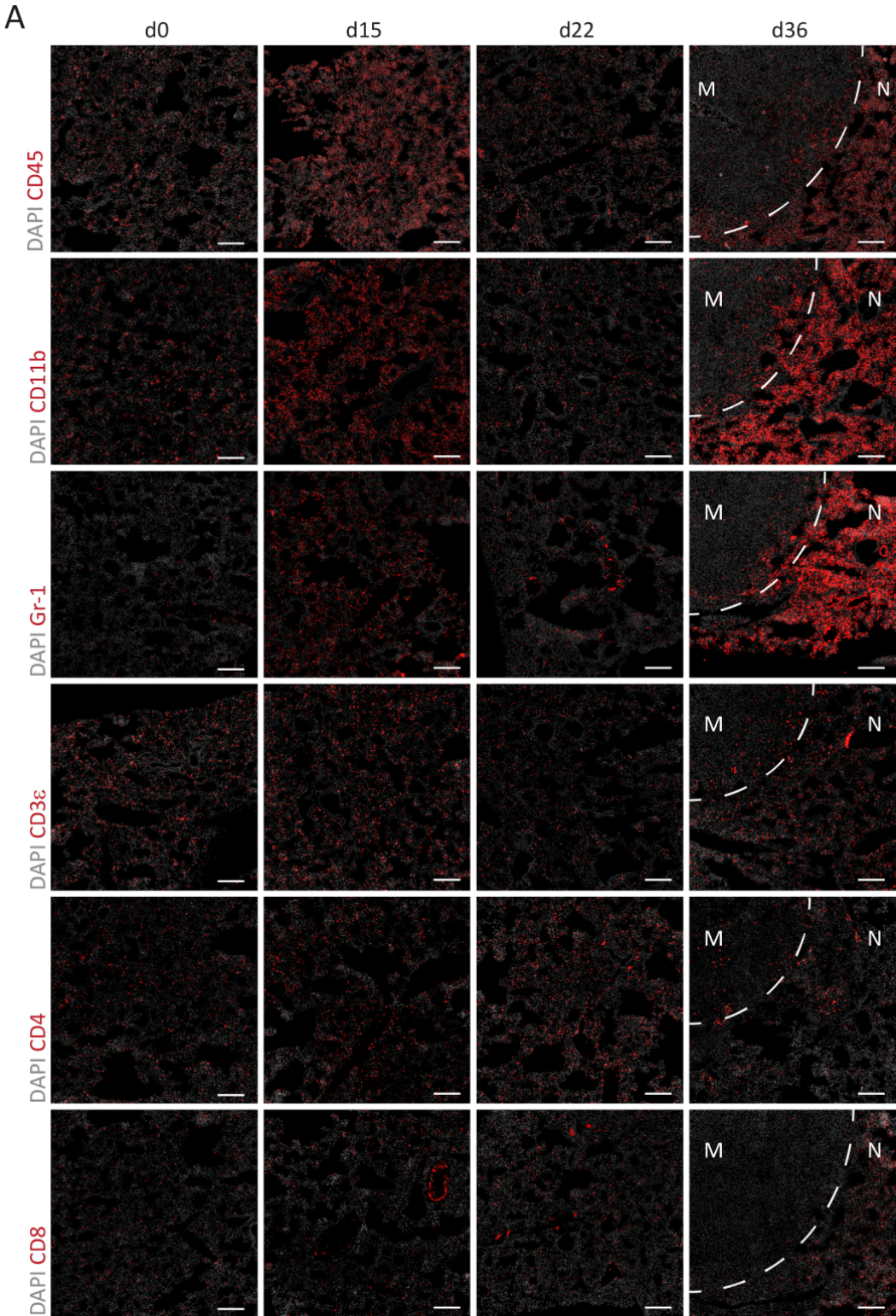


Figure 16. Presence of a primary tumor alters the immune landscape in the lung. (A) Immuno-fluorescence images showing infiltrating immune cells in the lung tissue. Scale bars = 200 μ m. M = metastatic nodule; N = normal adjacent tissue.

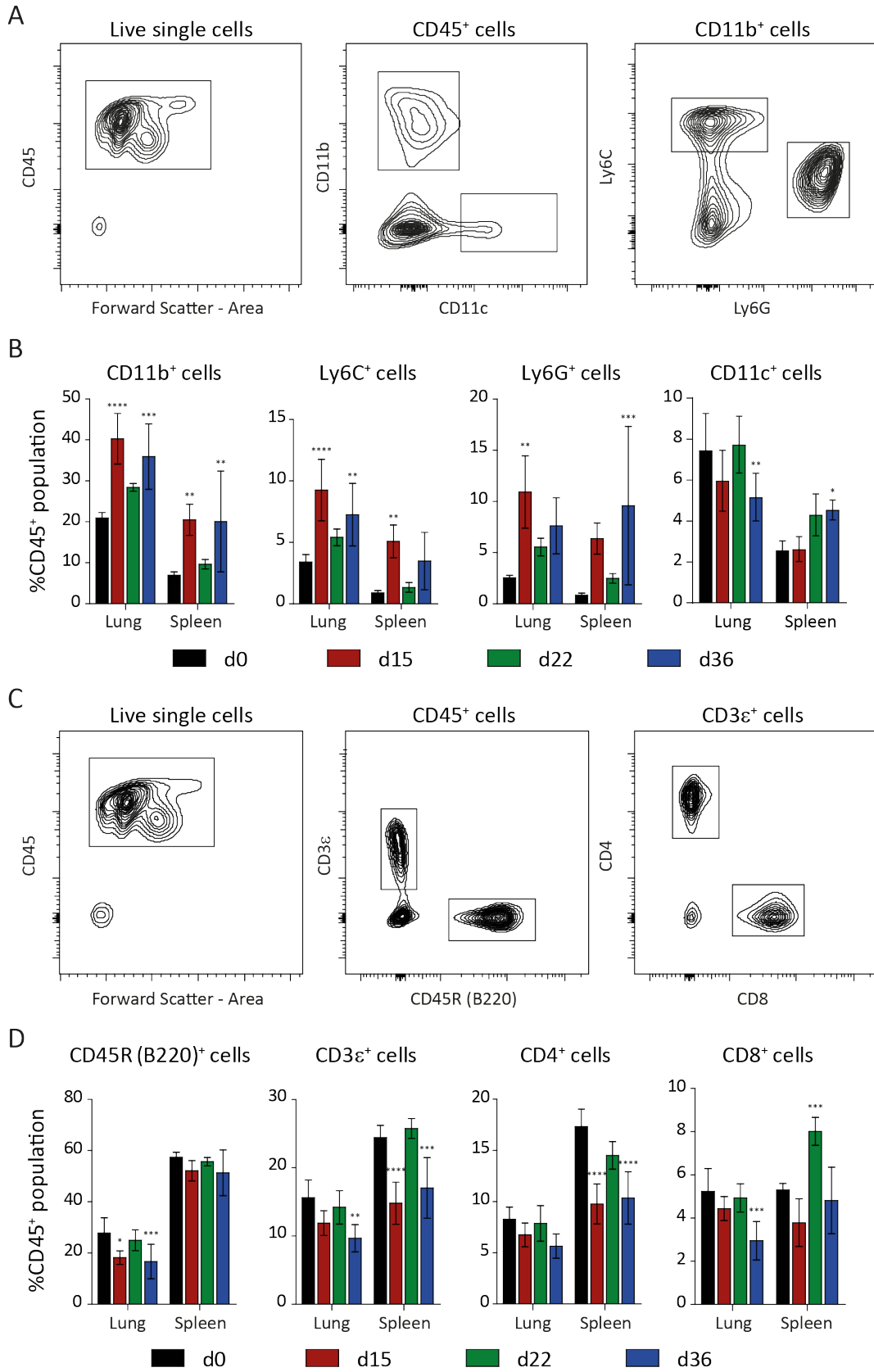


Figure 17. Immune-phenotyping of lung tissue during metastasis progression. Infiltrating immune cell populations were analyzed by flow cytometry at sequential stages of metastasis progression. Spleen tissue was simultaneously analyzed as the readout for systemic effects. (A) FACS schematics for gating different myeloid populations out of total leukocytes (CD45⁺). (B) Frequency of pan-myeloid (CD11b⁺), monocytic (Ly6C⁺), granulocytic (Ly6G⁺), and dendritic (CD11c⁺) cells of total leukocytes (mean \pm SD, n = 6-7 mice). *, P<0.05; **, P<0.01; ***, P<0.001; ****, P<0.0001 (2-way ANOVA with Bonferroni's multiple comparison test). (C) FACS schematics for gating different lymphoid populations out of total leukocytes (CD45⁺). (D) Frequency of B cells (CD45R-B220⁺), CD3e⁺, CD4⁺, and CD8⁺ T cells of total leukocytes (mean \pm SD, n = 6-7 mice). *, P<0.05; **, P<0.01; ***, P<0.001; ****, P<0.0001 (2-way ANOVA with Bonferroni's multiple comparison test).

2.2.3. *Lrg1* mediates EC responsiveness to tumor progression

A comparative gene ontology analysis of disease and bio-functions supported the immune-phenotyping data since leukocyte migration, activation and adhesion of myeloid cells were some of the key identified bio-functions (Fig. 18A). Additionally, the analysis unveiled disease stage-specific regulation of neovascularization-, cell viability- and metastasis-related gene sets (Fig. 18A).

Zooming-in on genes involved in EC development bio-function; multiple genes such as *Ccl2*, *Il6*, *Vcam1*, and *Mmp2* were found to be altered in a similar temporal manner as reported previously (173, 186) (Fig. 18B, D). Further, *Lrg1* was identified as one of the most differentially expressed EC-specific genes (Figs. 18B-D). *Lrg1* expression closely reflected the temporal pattern of systemic inflammation, thereby classifying *Lrg1* as an immediate endothelial response gene to tumor challenge. LRG1, Leucine-rich alpha-2-glycoprotein 1, was reported to modulate endothelial TGF β -signaling in the retinal vasculature (226). Mechanistically, in the presence of TGF β 1, LRG1 interacts with the accessory receptor Endoglin, thereby, switching the EC phenotype from quiescence-mediating ALK5 signaling to activation-inducing ALK1 signaling (226). This shift in TGF β -signaling was associated with retinal EC proliferation and migration and mediated pathological ocular angiogenesis. Concurrently, LRG1-neutralizing antibody restricted TGF β -signaling and attenuated ocular neoangiogenesis (226). Likewise, global deletion of *Lrg1* aggravated myocardial fibrosis with cardiac dysfunction following myocardial infraction. Interestingly, the heart phenotype was largely attributed to reduced capillary density and suppressed TGF β -signaling (227).

Indeed, upstream regulator analysis of the RNA-seq data revealed TGF β as the most significantly enriched z-score amongst d36 EC as compared with d0, clearly indicating a strong induction of TGF β -signaling with metastatic disease progression (Fig. 19A). Likewise, GSEA analysis confirmed the enrichment of subsequent downstream TGF β -signaling cascade during metastatic progression (Figs. 19B-C). Recently, employing comparative transcriptomic and epigenomic analysis of new-born and adult mice, it was discovered that SMAD6 and SMAD7, inhibitors of TGF β -signaling, were strongly upregulated in adults and potentially mediated acquisition of vascular quiescence (228). Therefore, altered TGF β -signaling and overall activation of lung endothelium during metastasis suggest a counter-regulation of the vascular maturation program (228).

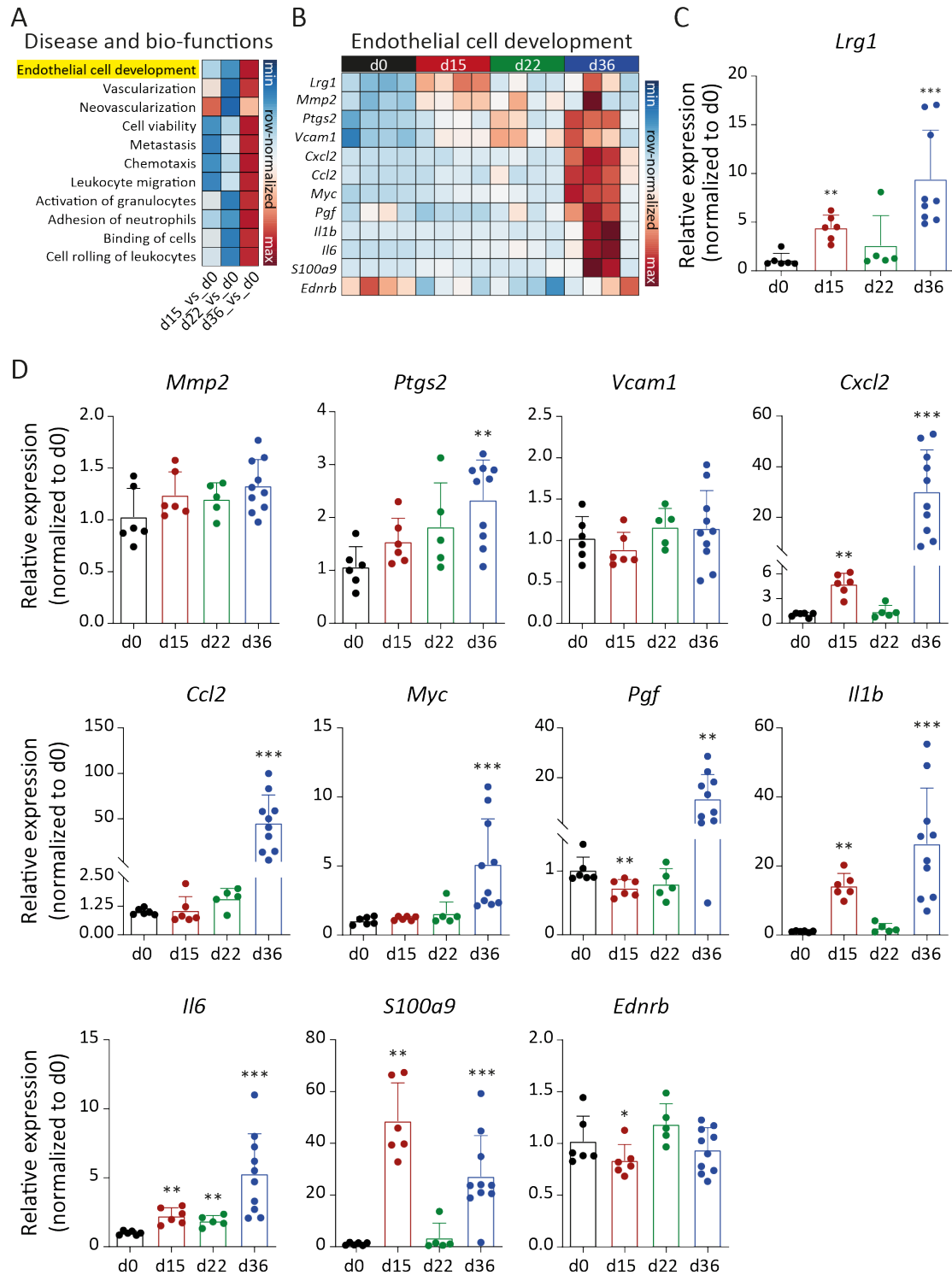


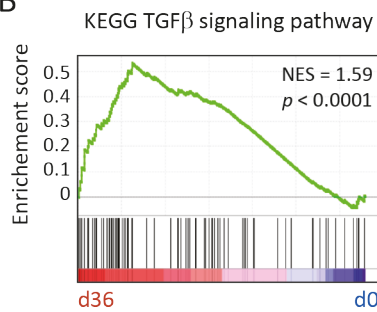
Figure 18. Expression kinetics of genes involved in the EC development gene set. (A) Comparison of disease and bio-functions was conducted using IPA. Correlation scores are shown for the selected disease and bio-functions. (B) Shown are genes involved in the EC development gene set. (C) qPCR quantitation of *Lrg1* expression in lung EC to validate RNA-seq data (mean \pm SD, $n = 5-9$ mice). (D) mRNA expression of genes during metastatic progression is shown (mean \pm SD, $n = 5-10$ mice). *, $P < 0.05$; **, $P < 0.01$; ***, $P < 0.001$ (two-tailed Mann-Whitney *U* test).

A

Upstream Regulators	d15_vs_d0*	d22_vs_d0*	d36_vs_d0*
TNF	4.218 (9.45 x 10 ⁻³²)	3.764 (2.56 x 10 ⁻²¹)	10.045 (3.42 x 10 ⁻⁷⁶)
IL1B	4.896 (4.87 x 10 ⁻²⁷)	4.44 (2.45 x 10 ⁻¹⁵)	9.516 (7.43 x 10 ⁻⁵⁶)
NFKB (COMPLEX)	3.712 (2.10 x 10 ⁻²⁰)	3.318 (1.16 x 10 ⁻⁹)	9.373 (6.57 x 10 ⁻⁴⁰)
VEGF	2.254 (2.16 x 10 ⁻¹⁴)	4.917 (1.63 x 10 ⁻²²)	7.855 (3.88 x 10 ⁻³⁹)
IFNG	5.239 (4.18 x 10 ⁻²⁷)	4.663 (8.55 x 10 ⁻¹⁴)	7.366 (1.16 x 10 ⁻⁵⁷)
TGFB1	0.011 (2.78 x 10 ⁻²⁸)	1.468 (9.39 x 10 ⁻²⁹)	7.214 (1.77 x 10 ⁻⁹⁴)
IL6	2.072 (6.85 x 10 ⁻²⁴)	3.257 (9.25 x 10 ⁻²³)	7.11 (2.03 x 10 ⁻⁶¹)
IGF1	2.578 (5.47 x 10 ⁻¹⁸)	2.336 (2.47 x 10 ⁻¹⁴)	6.542 (9.39 x 10 ⁻³⁷)
ERK	2.846 (5.47 x 10 ⁻¹⁷)	2.634 (3.51 x 10 ⁻⁷)	6.304 (1.34 x 10 ⁻²⁹)
STAT3	2.444 (4.31 x 10 ⁻¹⁴)	4.322 (1.36 x 10 ⁻⁹)	5.688 (8.44 x 10 ⁻³¹)
AP1	2.206 (2.06 x 10 ⁻¹⁵)	1.929 (8.29 x 10 ⁻⁹)	5.174 (1.69 x 10 ⁻¹⁹)
MAP2K1	2.529 (1.60 x 10 ⁻¹⁶)	2.772 (1.47 x 10 ⁻⁹)	5.003 (5.48 x 10 ⁻¹⁸)
JUN	1.771 (1.07 x 10 ⁻¹⁵)	1.836 (1.75 x 10 ⁻¹⁰)	4.817 (1.51 x 10 ⁻³⁵)
FAS	-0.344 (3.62 x 10 ⁻¹⁸)	0.354 (2.23 x 10 ⁻⁹)	-2.573 (6.81 x 10 ⁻²⁸)
DICER1	-0.539 (4.77 x 10 ⁻⁵)	-0.571 (6.66 x 10 ⁻⁵)	-2.817 (1.61 x 10 ⁻⁹)
CDKN1A	-0.512 (2.89 x 10 ⁻⁶)	-1.845 (4.96 x 10 ⁻³²)	-3.062 (6.96 x 10 ⁻⁴¹)
CTLA4	-1.633 (2.60 x 10 ⁻⁴)	-2.655 (1.76 x 10 ⁻⁷)	-3.087 (1.73 x 10 ⁻⁷)
KLF2	-2.573 (3.40 x 10 ⁻¹⁹)	-1.776 (2.06 x 10 ⁻¹⁴)	-3.39 (9.09 x 10 ⁻²³)
LET-7	-2.257 (7.10 x 10 ⁻⁴)	-3.856 (3.31 x 10 ⁻¹⁰)	-6.413 (1.92 x 10 ⁻²⁸)

* Values are presented as z-score (p-value).

B



C

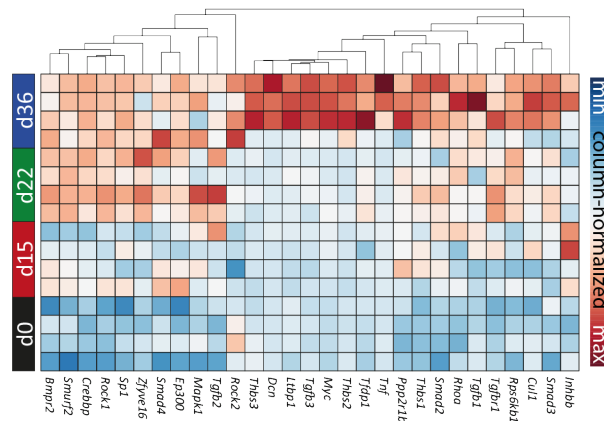


Figure 19. Upstream regulators of EC transcriptional changes. (A) Based on differential gene expression at different time points as compared with d0, putative upstream regulators were identified with IPA. Listed are the correlation scores (z-scores) and corresponding P-values for selected upstream regulators. (B) GSEA showing enriched TGFβ signaling in d36 as compared with d0. (C) Heatmap of genes involved in the TGFβ signaling gene set.

To investigate the spill of endothelial cell-derived secreted factors, a proteomic analysis of serum specimens at sequential stages of LLC tumor progression was undertaken. Consistent with the transcriptomic screen, LRG1 was one of the most abundant proteins differentially upregulated in d15 serum as compared with d0 specimens (Fig. 20A). Further supporting the bulk RNA-seq data, the serum levels of circulating LRG1 closely reflected the temporal pattern of mRNA expression in lung EC (Figs. 20A, B). In order to establish the clinical relevance of circulating LRG1 protein, a meta-analysis of several clinical retrospective studies was performed. Major criteria for the inclusion of a published article were the cohort size and parallel analysis of age-matched healthy volunteers. Given that different research groups employed different methods for estimating LRG1 levels in sera, data normalization was performed whereby cancer patients' data were computed relative to the cohort of healthy volunteers for each study. In full corroboration to our preclinical data, the meta-analysis revealed an upregulation of serum LRG1 levels for different human cancer entities as compared with corresponding cohorts of healthy volunteers, including colorectal, gastric, lung, ovarian, and pancreatic tumors (229-233) (Fig. 20C).

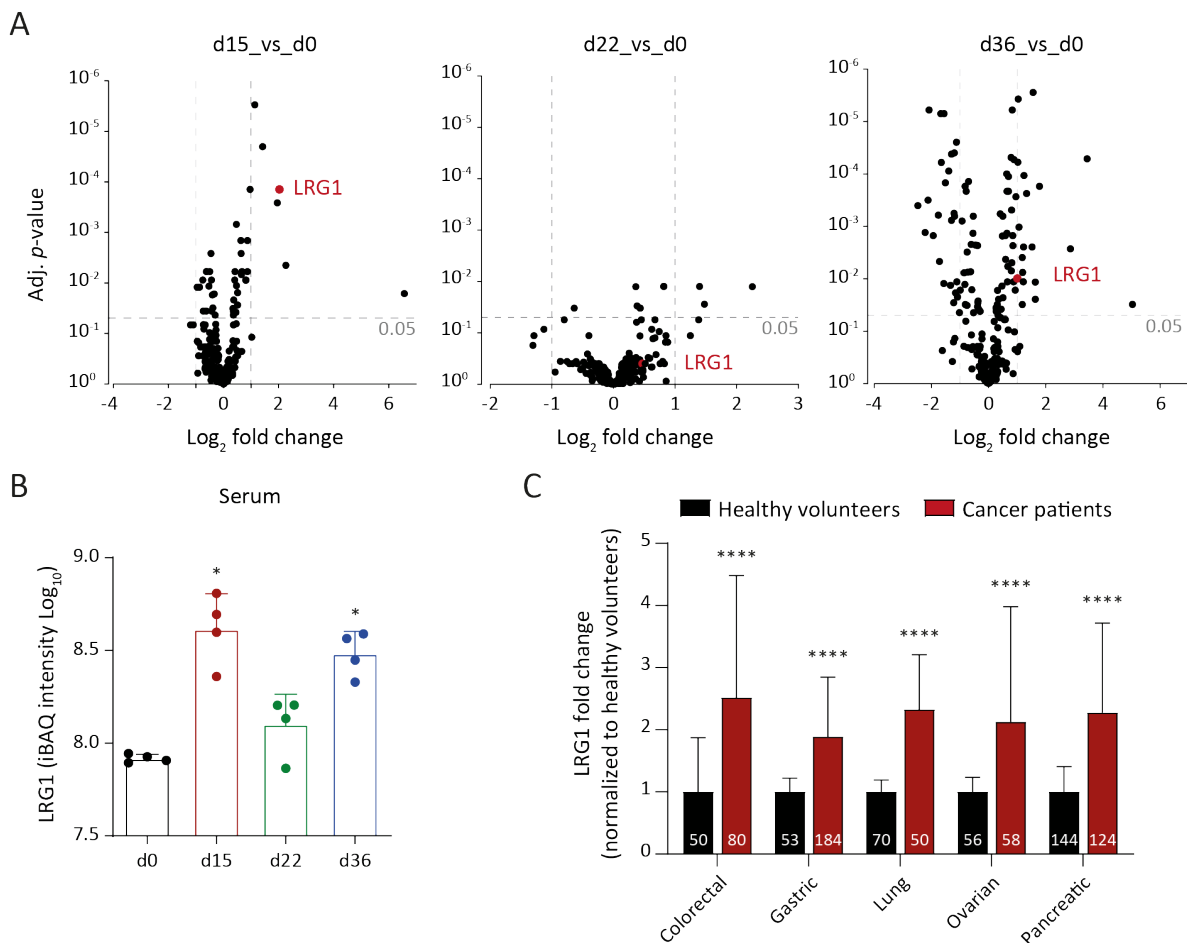


Figure 20. Proteomic analysis of serum during metastasis progression. (A) Volcano plots displaying FC and adjusted p-value for each identified protein in LC-MS analyses. The mean of 4 biological replicates is indicated. (B) Shown are iBAQ intensities of LRG1 protein in serum samples (mean \pm SD, n = 4 mice). *, P<0.05 (*two-tailed Mann-Whitney U test*). (C) LRG1 protein amounts in sera of cancer patients and healthy volunteers were retrieved from previously published articles (229-233). The bar graph shows relative LRG1 abundance normalized to the corresponding healthy cohort. Data normalization removes differences originating due to varying measurement techniques employed in different studies. The size of each sample cohort is indicated in the graph. ****, P<0.0001 (*multiple t-tests corrected with the Holm-Sidak method*).

Next, I wanted to validate the findings of the LLC screen in a second, less reductionist tumor model. Genetically-engineered mouse models (GEMMs) often develop spontaneous primary tumors of multifocal nature. A breast cancer GEMM for example develops primary tumors in multiple mammary pads, while a melanoma GEMM develops autochthonous tumors all over the dermis. Considering that it is experimentally almost impossible to resect all of these multi-focal primary tumors, it poses a major hurdle to undertake a metastasis experiment in GEMMs. To circumvent this caveat while conserving the natural tumor architecture, a GEMM-based syngraft strategy was employed for this project. Here, small bio-banked tumor fragments originally derived from primary breast tumors of a MMTV-PyMT (mouse mammary tumor virus-polyoma middle tumor-antigen) mouse were orthotopically implanted in the fourth mammary fat pad of syngeneic FVB/N mice (Fig. 21A). Unlike native GEMM, a focal primary tumor in GEMM-derived syngraft can be easily resected at an average size of 500 mm³ and spontaneous metastases can be traced in the absence of the primary tumor. In the MMTV-PyMT GEMM-derived syngraft model, metastases occur in the lungs and to a much lesser extent in lymph nodes approximately four weeks following primary tumor resections.

Similar to the LLC model, *Lrg1* was found upregulated in lung EC and in serum specimens during metastatic progression in the MMTV-PyMT GEMM-derived syngraft model (Figs. 21B, C). These data underline the systemic regulation of LRG1 during metastatic progression. However, unlike the LLC model, LRG1 levels did not subside following primary tumor resection in the MMTV-PyMT model, possibly due to varying kinetics of different mouse tumor models. Future work will need to include additional preclinical metastasis models for different cancer entities to explore the role of LRG1 across different carcinomas as well as sarcomas.

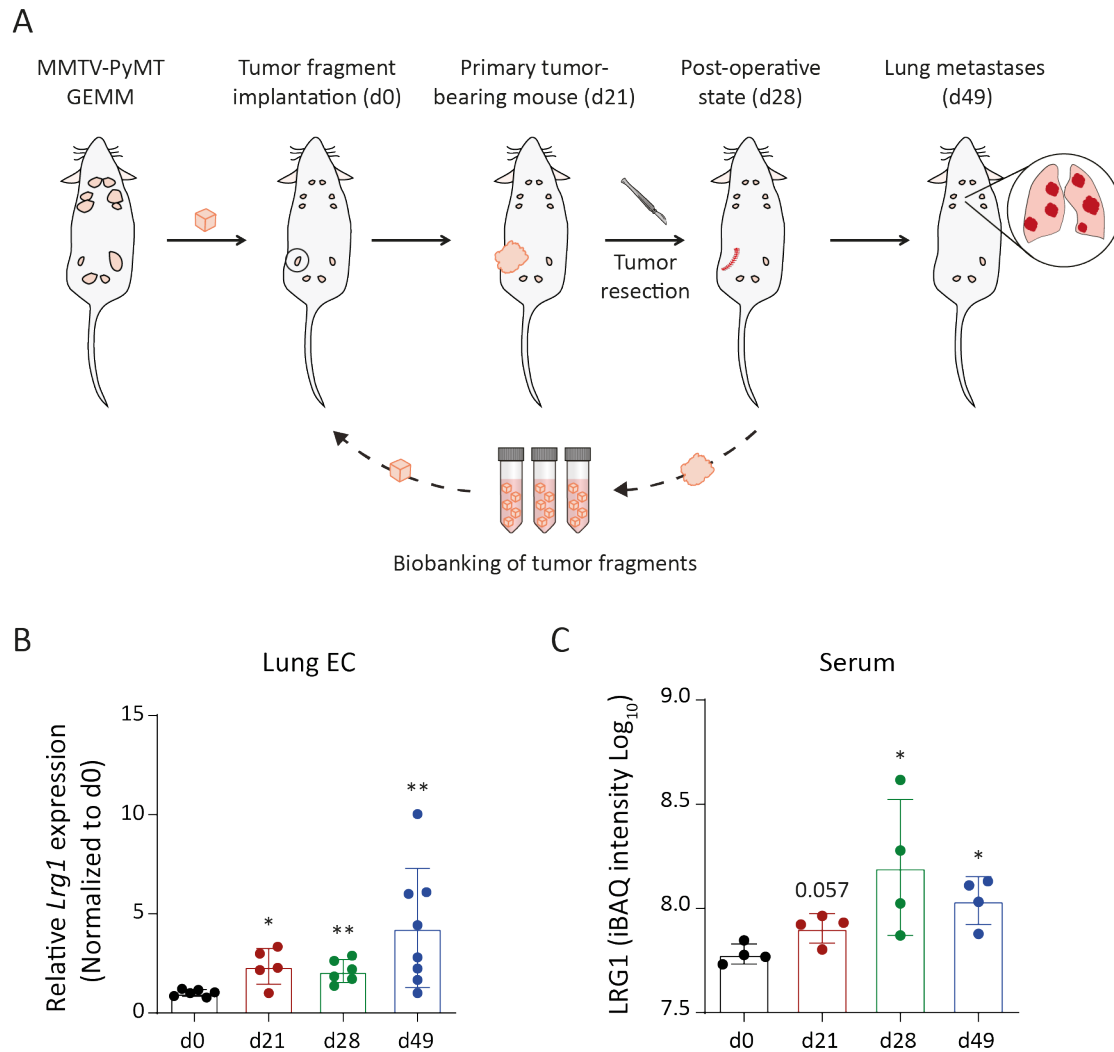


Figure 21. LRG1 is systemically upregulated in a breast (MMTV-PyMT) cancer model. (A) Tumors from a genetically engineered mouse model of breast cancer were fragmented into small pieces and bio-banked in liquid nitrogen for long-term storage. Individual tumor fragments ($\sim 10 \text{ mm}^3$ in volume) were surgically implanted in the fourth mammary pad of syngeneic FVB/N mice. Mice developed lung metastasis following primary tumor resection. (B) Dot plot showing *Lrg1* expression in isolated lung EC at sequential stages of tumor progression (mean \pm SD, $n = 5-8$ mice). *, $P < 0.05$; **, $P < 0.01$ (two-tailed Mann-Whitney *U* test). (C) Shown are protein levels (iBAQ intensities) of LRG1 in sera specimens (mean \pm SD, $n = 4$ mice). *, $P < 0.05$ (two-tailed Mann-Whitney *U* test).

2.2.4. Leukocyte-derived LRG1 is dispensable for tumor progression

To determine the primary source of circulating LRG1, *Lrg1* expression was compared amongst *in vitro*-cultured LLC cells, primary tumors, and d15 lung tissue. While LLC cells lacked endogenous expression of *Lrg1*, lung tissue displayed higher *Lrg1* expression as compared with primary tumor tissue (Fig. 22A). To further dissect the cellular source of *Lrg1*; EC, leukocytes, and CD31⁻CD45⁻ cells were isolated from both primary tumor and d15 lung tissue. qPCR analysis revealed that *Lrg1* expression was strongly enriched in the EC population (Fig. 22B). Nevertheless, infiltrating leukocytes did express detectable levels of *Lrg1* in primary tumors as well (Fig. 22B).

Next, to investigate the role of leukocyte-derived LRG1 in tumor progression, bone marrow (BM) chimeric mice were generated with either WT or *Lrg1*-KO BM cells (Figs. 22C-E). Here, whole BM cells, including 5000 Lin⁻Sca1⁺Kit⁺ cells, were intravenously infused in lethally irradiated host mice (Fig. 22C, D). Two months later, BM chimeric mice were subjected to LLC metastasis experiment. At the time of primary tumor resection, tumors were collected and analyzed for different vascular parameters. Lack of leukocyte-derived LRG1 did not affect primary tumor vasculature (Figs. 23A, B). There was no evidence of any major alterations in normalized vessel density or perivascular coverage using CD31 and Desmin co-staining. Elevated levels of LRG1 promote angiogenesis and its neutralization mediates vessel normalization in primary tumors (unpublished information shared by our collaborators). Lack of alterations in any intratumor vascular parameters clearly suggests that leukocyte-derived LRG1 is largely dispensable for primary tumor growth.

Following primary tumor resections, mice were closely examined for the experimental end-point criteria including weight loss, apathy, difficulties with breathing, hunchback, and other physical deformities. At the time of sacrifice, spleens were collected from all mice. A quantitative PCR analysis was performed to compute *Lrg1* gene expression. *Lrg1*-KO BM chimeras exhibited a strong decline in *Lrg1* gene expression certifying a successful BM chimerism as compared with WT BM chimeric mice (Fig. 22E). Similar to the primary tumors, *Lrg1* knockout in hematopoietic cells did not impact overall survival of mice when compared with the cohort of WT BM-chimeras (Fig. 22F), therefore indicating that leukocyte-expressed LRG1 is not required for metastasis.

It is noteworthy that LRG1 was previously reported to mediate granulocytic differentiation and was found to be packed in the granules of differentiating myeloid cells (234). LRG1 was released upon neutrophil activation and exhibited distinct biological properties crucial for microenvironmental modulation in bone marrow. It was also postulated that unlike EC where LRG1 provides proliferation cues, in the case of bone marrow microenvironment, LRG1 might be antagonistic to TGF β -signaling (235). Therefore, by antagonizing the inhibitory functions of TGF β -signaling on myeloid progenitors, LRG1 promotes myelopoiesis. Nevertheless, the present data suggest that EC represent the major cellular source of LRG1, and leukocyte-derived LRG1 is largely dispensable during metastasis.

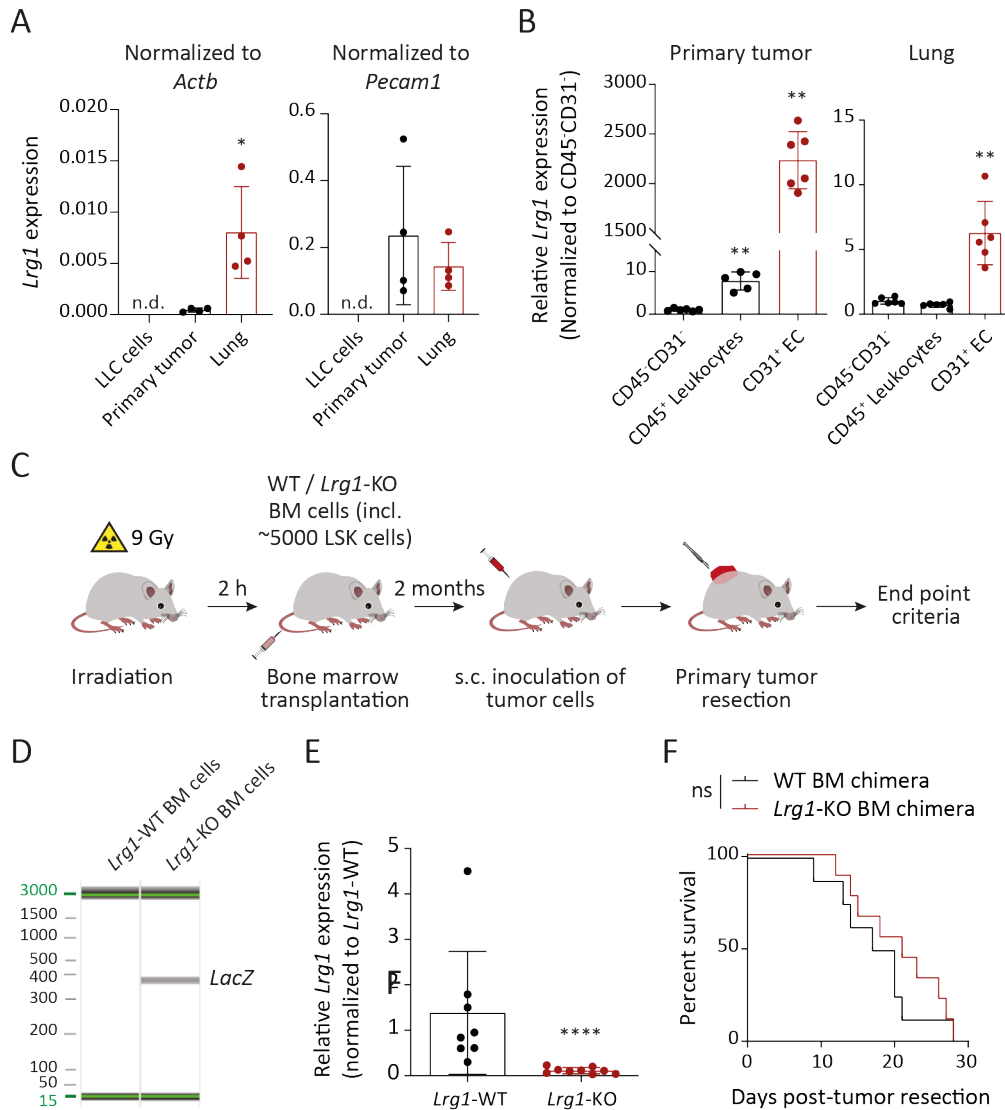


Figure 22. Leukocyte-derived LRG1 is dispensable for metastasis. (A) Comparison of *Lrg1* expression between *in vitro*-cultured LLC cells, primary tumor and d15 lung tissue (mean \pm SD, $n = 4$ mice). *, $P < 0.05$ (two-tailed Mann-Whitney *U* test). (B) EC, leukocytes, and CD31⁺CD45⁻ cells were isolated from primary tumors and d15 lung tissues. Dot plots show relative *Lrg1* expression in EC and leukocytes as compared with CD31⁺CD45⁻ cells (mean \pm SD, $n = 5-6$ mice). **, $P < 0.01$ (two-tailed Mann-Whitney *U* test). (C-F) BM chimeras, harboring an *Lrg1* knock-out in the hematopoietic compartment, were employed for the LLC spontaneous metastasis model. (C) BM cells were isolated from *Lrg1* global KO mice or wild-type littermates. Irradiation-preconditioned mice received an infusion of whole BM cells (including ~ 5000 Lin⁺Sca-1⁺Kit⁺ cells). 2 months later, the LLC metastasis experiment was initiated in BM chimeric mice. Following primary tumor resection, mice were closely observed for the experimental endpoint criteria. (D) Shown is a genotyping PCR for *LacZ* to ensure genetic knockout of *Lrg1* in the isolated BM cells. (E) Dot plot illustrating a strong decline in *Lrg1* expression amongst the whole splenocyte population (mean \pm SD, $n = 8-9$ mice). ****, $P < 0.0001$ (two-tailed Mann-Whitney *U* test). (F) LLC tumors were implanted in WT or *Lrg1*-KO BM chimeras. Kaplan-Meier graph showing overall survival of mice after primary tumor resection ($n = 8-9$ mice). The comparison was rendered non-significant (ns) according to Log-rank (Mantel-Cox) test. n.d. = non-detectable.

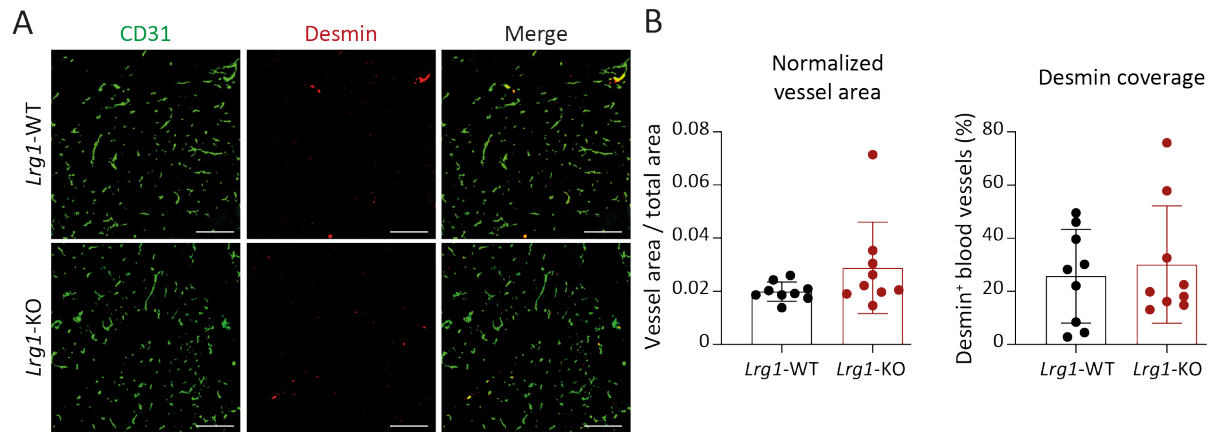


Figure 23. Lrg1-KO BM chimeras exhibit no apparent defects in primary tumor vasculature. (A-B) Primary tumor tissues were collected at the time of resection, and the intratumoral vasculature was analyzed. Representative immunofluorescence images (A), and corresponding quantitation (B) of normalized vascular area and desmin coverage show no differences between the two groups (mean \pm SD, $n = 9$ mice). Scale bars = 200 μ m. The comparison was rendered non-significant according to *two-tailed Mann-Whitney U test*.

2.2.5. Single-cell RNA-seq analysis reveals no changes in the vascular tree during metastasis

To gain insights into EC transcriptomic heterogeneity and to map *Lrg1* expression across EC subpopulations, single-cell RNA sequencing of lung EC isolated at sequential stages of tumor progression was conducted. The cellular heterogeneity was investigated both, within and between the samples by applying uniform manifold approximation and projection (UMAP) and graph-based clustering. Following biologically-supervised filtering to remove identified contaminants (Fig. 24A), 8,512 endothelial cells were annotated as capillary, arterial, venous, mesenchymal-like, and cycling populations based on the top 10 differentially-expressed genes in each cluster (Figs. 24B, C). All analyzed cells were *Cdh5* and *Cldn5* positive, emphasizing on their endothelial identity. Arterial cells were *Ednrb*⁺ and showed strong enrichment of *Kdr* (VEGFR2). Venous cells were *Nr2f2*⁺ (COUP-TFII) and displayed enhanced expression of *Vegfc* and *Dll1*. Interestingly, mesenchymal-like cells demonstrated a very similar gene expression pattern to the capillary cells however, they were enriched in mesenchymal genes such as *Plat*, *Mgp*, and *Fbln5*. Lastly, the cycling endothelial cells were identified by the elevated expression of *Cdk1*, *Birc5*, *Top2a*, and *Cks2* genes. Only 81 cells belonged to the cycling cluster which makes it difficult to draw any definite conclusions.

The cluster annotation was in line with the current knowledge of prominent vascular signaling families including Vegf-Vegfr, Ang-Tie, and Notch (Fig. 24D), and corroborated with recently published single-cell data of homeostatic lung and tumor EC (236, 237). Unexpectedly, the clustering of lung EC remained unaffected during metastasis progression (Fig. 24E) and there were no overt changes in the distribution of cells amongst the clusters (Fig. 24F), thereby negating any major restructuring of the vascular hierarchical network as metastatic disease progressed.

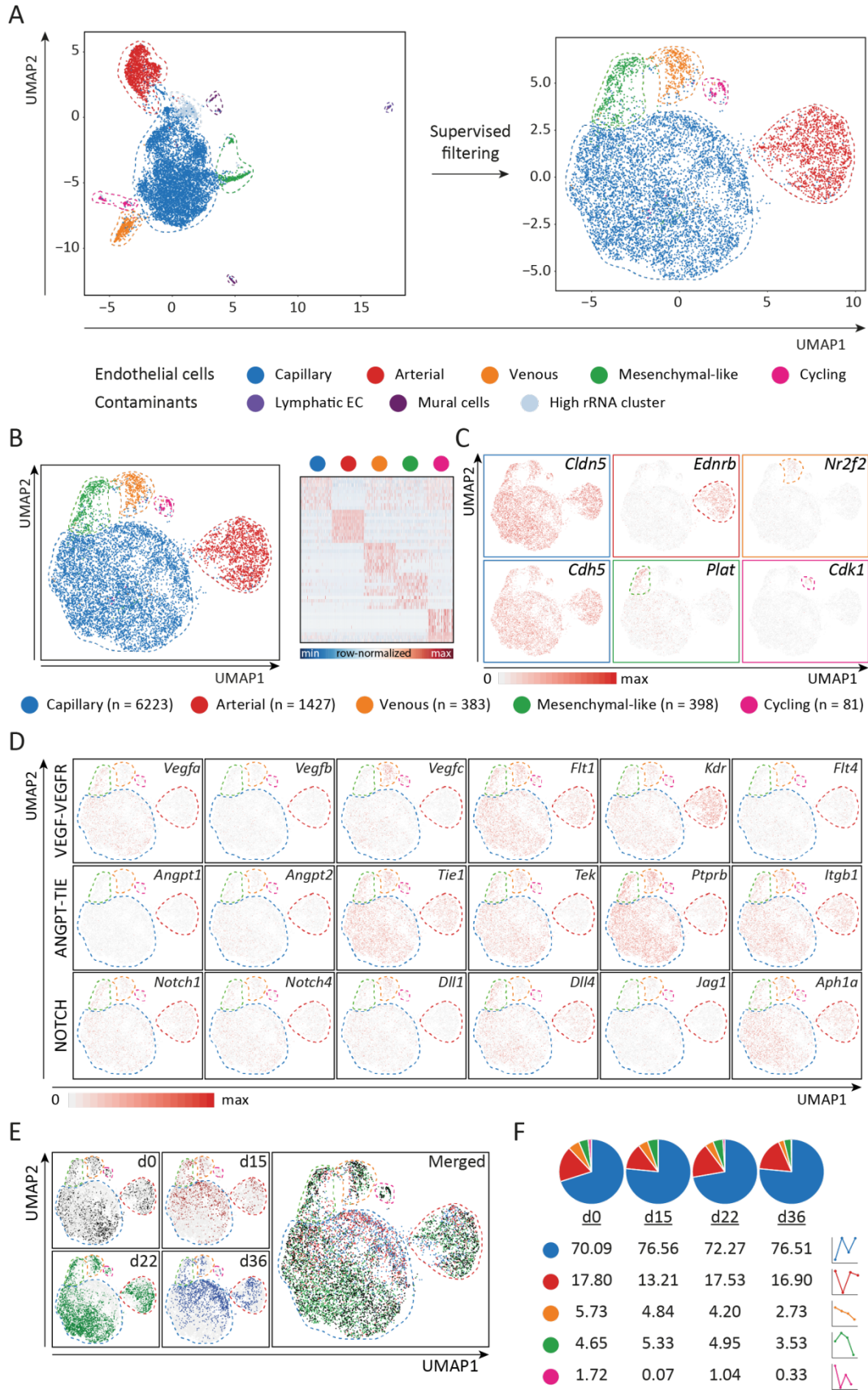


Figure 24. Single-cell analysis of lung endothelium during metastasis. (A) Following an unbiased clustering, biologically supervised filtering was performed, and contaminants including lymphatic EC, mural cells and cluster enriched in ribosomal genes were removed. (B) On the left, UMAP visualization of color-coded clusters of lung EC ($n = 8,512$ cells). On the right, gene signature of the capillary, arterial, venous, mesenchymal-like, and cycling subpopulations based on 10 most-upregulated genes. (C) Feature plots indicating enriched genes for each identified subpopulation. EC-specific *Cldn5* and *Cdh5* were uniformly expressed by all subpopulations. (D) Feature plots showing gene expression of vascular signaling families. Dotted lines mark EC subpopulations. (E) Plots showing cells of individual and merge of all four samples. (F) Pie charts representing frequencies of different EC subpopulations within the total cells analyzed for each time point. Trend lines display changes in each subpopulation as the disease progresses.

Approximately 60% of venous EC were found positive for *Lrg1* expression (Fig. 25A), attributing to the fact that LRG1 was initially identified as a marker for high-endothelial venules (238). Yet, *Lrg1*⁺ venous cells constituted merely 20% of total *Lrg1*⁺ cells, while the remaining 80% of *Lrg1*⁺ cells were uniformly dispersed amongst the other clusters (Fig. 25B). Temporal changes in the cluster-wise distribution of *Lrg1*⁺ cells reflected the altering frequencies of each subpopulation amongst the total number of EC. For example, with the disease progression, the frequency of venous cells declines and similarly does the contribution of venous cells to the total *Lrg1*⁺ cells. This hints towards the relevance of systemic upregulation in *Lrg1* gene expression irrespective of EC subpopulations.

Indeed, whilst the frequency of cells expressing *Lrg1* (Log_2 -normalized expression >0) remained largely unchanged between the samples, d15 and d36 witnessed a much higher fraction of total cells with elevated levels of *Lrg1* expression (Log_2 -normalized expression >2) (Fig. 25C). Given that the overall frequencies of subpopulations are not drastically different at various disease stages; the single-cell data, in full corroboration with the bulk RNA-seq data, highlighted a systemic upregulation of *Lrg1* expression throughout the lung EC in a tumor stage-specific pattern.

To investigate the effect of the primary tumor on different organ vasculature, EC were isolated from different organs including brain, heart, kidney, liver, and muscle from either wild-type or tumor-bearing mice. Quantitative PCR-based analysis revealed an upregulation of *Lrg1* expression levels across all examined vascular beds in d15 mice when compared with the resting vasculature (Fig. 25D). It is noteworthy that enhanced *Lrg1* expression across all vascular beds might have resulted in the observed increase in serum levels of LRG1. Remarkably, endothelium with its humongous surface area, approximately equivalent to a soccer stadium, functions as a signal amplifier in response to tumor-derived signals, thereby playing a pivotal role during tumor progression and metastasis. It remains unknown whether changes in *Lrg1* expression are induced directly by tumor cell-derived factors or indirectly as a consequence of systemic inflammation. Future research will focus on identifying the exact upstream mechanisms that underlie the expression of *Lrg1*.

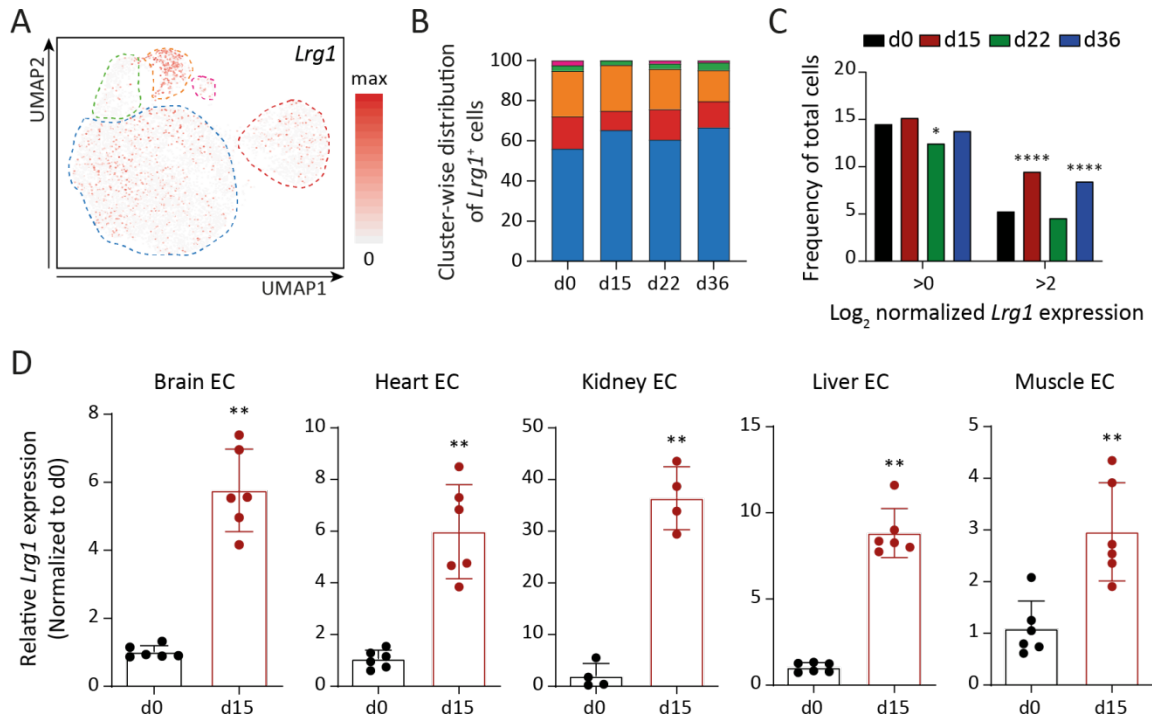


Figure 25. Vascular endothelial cells are the major source of *Lrg1*. (A) Feature plot displaying *Lrg1* expression across all analyzed lung EC. (B) Shown is the cluster-wise spread of *Lrg1*-expressing cells for each sample. (C) The graph highlights the frequency of *Lrg1*-expressing cells (\log_2 -normalized expression >0 or >2) amongst the total number of cells per sample. *, $P < 0.05$; ****, $P < 0.0001$ (two-sided Fischer's exact test). (D) *Lrg1* expression was analyzed in EC isolated from multiple organs of d0 and d15 mice (mean \pm SD, $n = 4-6$ mice). **, $P < 0.01$ (two-tailed Mann-Whitney U test).

2.2.6. Systemically elevated LRG1 facilitates metastatic colonization

To understand the function of LRG1 during metastatic progression, a systemic gain-of-function (GOF) experiment was set up. Here, LLC cells, which lack endogenous expression of *Lrg1* were transduced with a lentivirus to ectopically overexpress *Lrg1* (Fig. 26A). Afterward, mice were subcutaneously implanted with LLC-pLenti or LLC-Lrg1 tumors. LLC-Lrg1 primary tumors displayed a strong upregulation of *Lrg1* expression as compared with LLC-pLenti tumors (Fig. 26B). These primary tumors serve as an artificial source of circulating LRG1. Consecutively, LRG1 serum levels were also strongly elevated in LLC-Lrg1 tumor-bearing mice (Fig. 26C), thereby, providing a systemic GOF of LRG1.

In this established systemic GOF model, melanoma (B16F10) cells were intravenously injected once the primary tumors (LLC-Lrg1 or LLC-pLenti) reached an average tumor size of just 50 mm³ (Fig. 26D). Mice with systemic upregulation of LRG1 exhibited a strong increase in melanoma lung metastases (Fig. 26E), thereby demonstrating a pro-metastatic role of systemic LRG1. It should be noted that LLC cells do not metastasize by day 21, and often require much longer time periods to develop lung metastases.

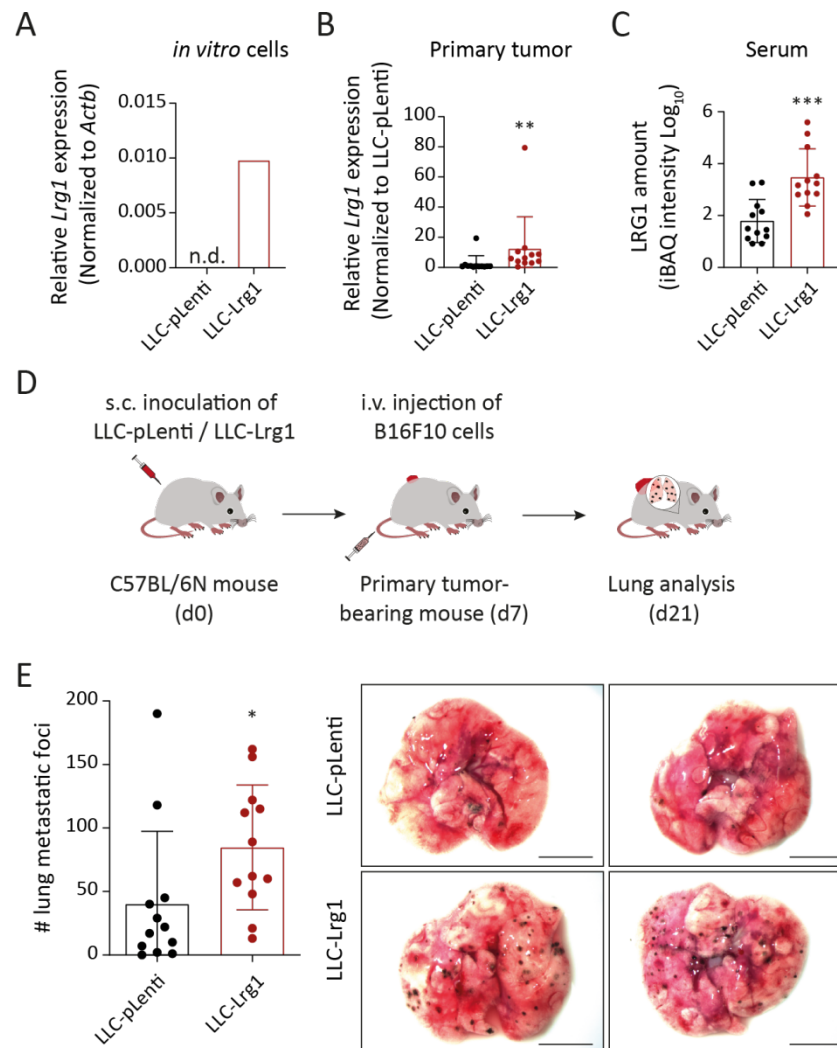


Figure 26. Elevated levels of LRG1 facilitate metastatic colonization. (A-C) Establishment of a systemic gain-of-function (GOF) experiment for LRG1. (A) qPCR comparison of LLC cells transduced with lentivirus overexpressing either empty vector (pLenti) or *Lrg1*. LLC-pLenti or LLC-Lrg1 cells were subcutaneously implanted in C57BL/6N mice. (B) Dot plot comparing *Lrg1* expression in the whole primary tumor tissue (mean \pm SD, n = 12 mice). **, $P < 0.01$ (two-tailed Mann-Whitney *U* test). (C) Shown are protein levels (iBAQ intensities) of LRG1 in sera of LLC (pLenti/Lrg1) tumor-bearing mice (mean \pm SD, n = 12 mice). ***, $P < 0.001$ (two-tailed Mann-Whitney *U* test). (D) Schematics of GOF of LRG1 coupled with an experimental melanoma metastasis assay. Briefly, *Lrg1*-overexpressing LLC (LLC-Lrg1) or control-LLC (LLC-pLenti) cells were subcutaneously inoculated in mice. 7 days later, melanoma (B16F10) cells were intravenously injected. (E) On the left, dot plot showing the number of melanoma metastases in the lung, and on the right, representative lung images (mean \pm SD, n = 12 mice). Scale bars = 5 mm. *, $P < 0.05$ (two-tailed Mann-Whitney *U* test). n.d. = non-detectable.

To further decipher the exact step of the metastatic cascade, LLC-pLenti and LLC-Lrg1 tumors were resected 24 h after intravenous injection of melanoma cells (Fig. 27A). There were no differences observed between the two groups suggesting that the pro-metastatic effect of systemic LRG1 was rapidly lost upon withdrawal of the source of LRG1 during metastatic colonization (Fig. 27B). To conclusively rule out any possible direct effect of LRG1 on tumor cell extravasation, mice were

preconditioned with a single injection of either LRG1-neutralizing antibody (anti-LRG1) or control-IgG prior to intravenous injection of melanoma cells (Fig. 27C). Consistent with the previous results, blocking LRG1 did not affect the extravasation of melanoma cells (Fig. 27D). Collectively, systemically elevated levels of LRG1 supported colonization of disseminated tumor cells.

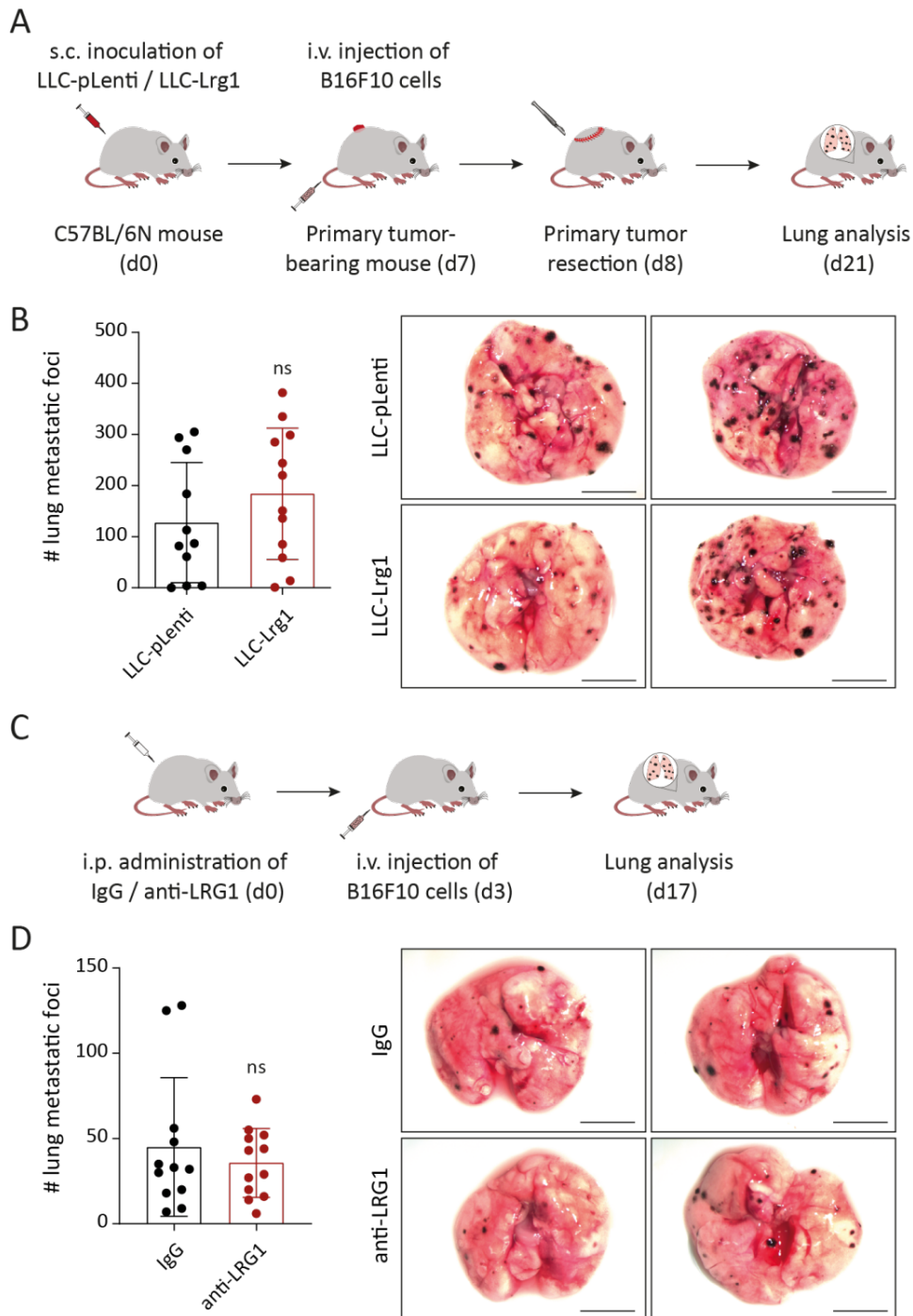


Figure 27. Systemic LRG1 does not affect extravasation of circulating tumor cells. (A) In addition to (Fig. 26D), primary tumors (the source of LRG1) were resected 24 hours after the intravenous injection of melanoma cells. (B) Quantitation of melanoma lung metastases is shown. The comparison was rendered non-significant (ns) according to *two-tailed Mann-Whitney U test*. On the right, representative lung images are displayed. (C) C57BL/6N mice were preconditioned with anti-LRG1 or control-IgG. 3 days later, melanoma cells were injected intravenously to initialize an experimental metastasis assay. (D) On the left, dot plot showing the number of melanoma metastases in the lung, and on the right, representative lung images (mean \pm SD, n = 12 mice). Scale bars = 5 mm. The comparison was rendered non-significant (ns) according to *two-tailed Mann-Whitney U test*.

2.2.7. LRG1 inhibition limits metastasis and prolongs overall survival

After validating a crucial role of systemic LRG1 in metastasis, next a monoclonal blocking antibody was employed to therapeutically target LRG1. Here, LRG1-neutralizing antibody 15C4 (provided by our collaborators) was administered during LLC metastasis assay in two clinically relevant therapeutic settings – short-term perioperative and long-term postsurgical adjuvant therapy (Fig. 28A). Perioperative therapy was initiated after LLC tumors had grown to an average size of 150 mm³ and therapy was discontinued 10 days post-primary tumor resection. This short-term treatment had no apparent effects on the primary tumor vasculature (Fig. 28B). Yet, perioperative therapy with anti-LRG1 yielded a significant overall survival advantage (Fig. 28C), fully confirming the pro-metastatic role of LRG1.

To circumvent any effect on primary tumor growth or early steps in the metastatic cascade such as intravasation and extravasation, an adjuvant therapy approach was employed wherein administration of anti-LRG1 or control-IgG was commenced 1-day after primary tumor resection until the experimental endpoint. Similar to the perioperative approach, long-term adjuvant therapy prolonged overall survival of mice by 8.5 days, which corresponded to an approximately 40% improvement over the control-IgG treated group (Fig. 28D). Remarkably, anti-LRG1 as a monotherapy offered a substantial overall survival advantage in a mouse model which has previously been reported to be refractory to anti-VEGF therapy (239, 240) and in which chemotherapy shows nearly no effect on lung metastatic burden (173). In conclusion, neutralizing LRG1 suppressed tumor cell colonization and provided a significant survival benefit in a clinically-relevant therapeutic window.

Recently, a phase I/IIa clinical trial with Magacizumab, a humanized version of anti-LRG1 employed in this study, has been initiated for patients with neovascular age-related macular degeneration. The preclinical data presented here validate LRG1 as a therapeutic target for oncology and warrant further clinical investigations to assess therapeutic potential of LRG1 for restricting metastasis.

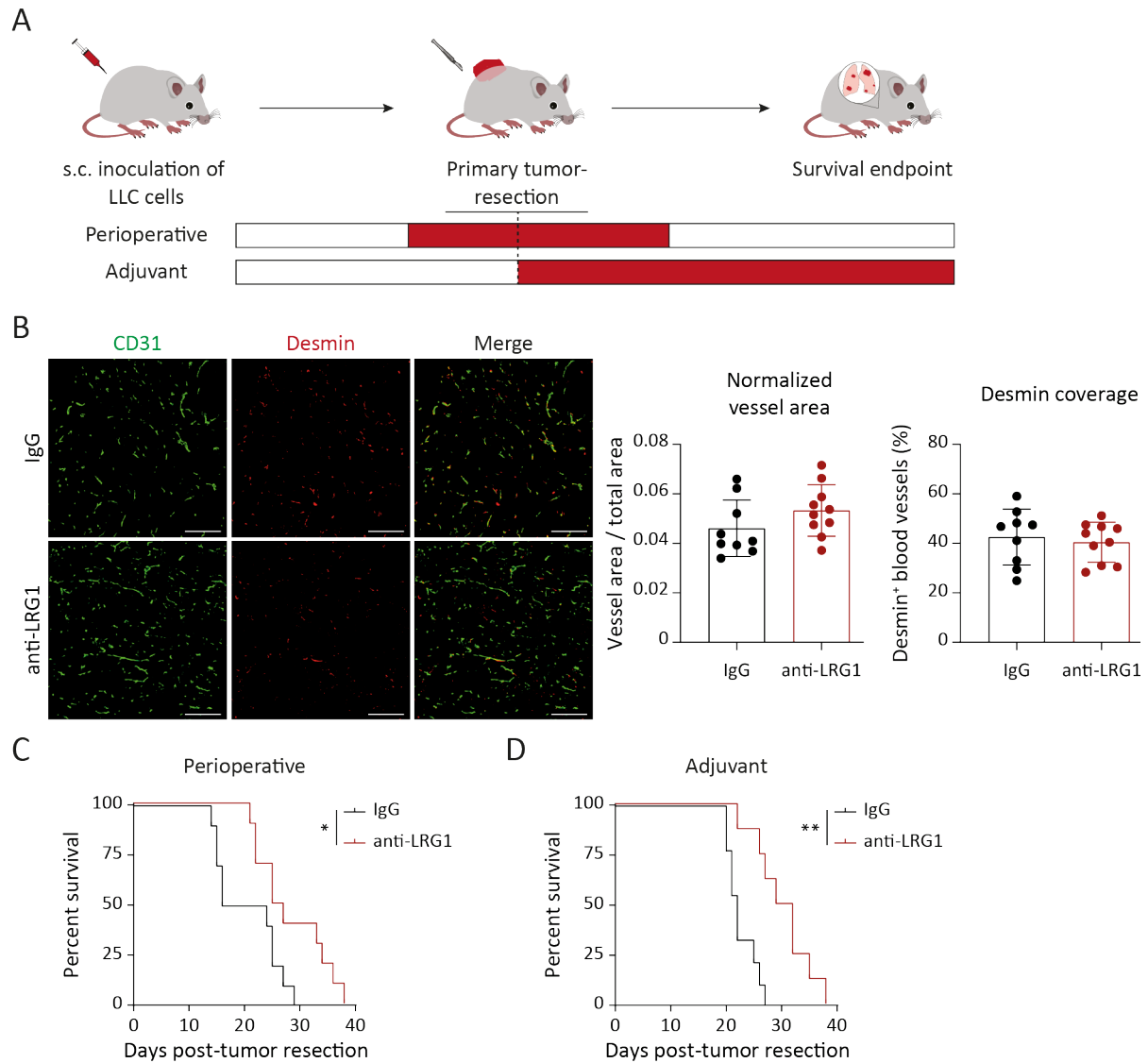


Figure 28. LRG1 neutralization inhibits metastasis. (A) Schematic of therapeutic assessment of LRG1 blocking in LLC metastasis model using two different strategies. (B) Perioperative administration of anti-LRG1 does not affect primary tumor vasculature. Representative immunofluorescence images of primary tumor sections stained with CD31 (EC-specific marker) and Desmin (pericyte-specific marker). Scale bars = 200 μ m. On the right, quantifications of normalized vessel area and Desmin coverage are shown (mean \pm SD, n = 9-10 mice). All comparisons were rendered non-significant according to *two-tailed Mann-Whitney U test*. (C-D) Kaplan-Meier graphs showing overall survival of mice after primary tumor resection when treated with control-IgG or anti-LRG1 in perioperative (C; n = 10 mice) or postsurgical adjuvant (D; n = 8-9 mice) setting (50 mg/kg twice per week). Mice with primary tumor regrowth were excluded from the analysis. *, $P < 0.05$; **, $P < 0.01$ (*Log-rank (Mantel-Cox test)*).

3. Conclusion

The emergence of organotypic vasculature and clinical pursuit of endothelial progenitor cells as a regenerative tool has pushed the field of vascular biology beyond the dogmatic boundaries of sprouting angiogenesis. Adoption of high-resolution spatial microscopy, cutting-edge preclinical murine experimental models, and next-generation sequencing tools have brought upon a technological revolution to expand our limited knowledge about intra- and inter-organ vascular diversity. The recently acquired knowledge enabled scientists to decipher the multicellular crosstalk within a tissue microenvironment, thereby allowing them to better understand the underlying angiocrine signals in health and disease. My doctoral research was primarily aimed - (i) at unambiguously define the cellular source of regenerating adult liver vasculature and (ii) at establishing the systems map of EC transcriptomic changes during lung metastatic colonization.

3.1. Bone marrow-derived cells harbor reparative potential and can physically integrate into the ailing liver vasculature

In line with previous reports (54, 57, 75, 76), the present study found a subset of BMDMC to physically incorporate into the liver vasculature in irradiation-preconditioned BM chimeric mice. Surprisingly, this effect was independent of PHx-induced regenerative burst. Detailed molecular analysis revealed that liver EC were particularly sensitive to X-ray irradiation and sustained apoptosis-inducing DNA damage as a consequence of irradiation exposure. Further, irradiation preconditioning caused catastrophic damage to liver EC, thereby warranting an immediate reparative action. The present data unveiled that the ailing liver vasculature, by upregulating *Icam1* expression, recruited BM cells for tissue rejuvenation. Subsequently, the application of an abdominal lead shield prevented the liver from irradiation exposure, and could successfully reverse the incorporation of BM cells (data shared by our collaborators). These data indicate that BM cells can differentiate into liver EC, which are morphologically and functionally indistinguishable from the preexisting resident EC (Fig. 29).

To evaluate the regenerative potential of the identified subset of BM cells following partial hepatectomy, two different clinically relevant strategies including G-CSF-mediated mobilization of endogenous BM stem cells, and intravenous infusion of ectopically harvested BMDMC, were applied. Following PHx, neither of the regenerative therapies displayed any direct benefit towards regenerating liver vasculature. The lack of any physical integration of BM cells in the preclinical experiments may partly explain why a recently concluded phase II clinical trial (REALISTIC), involving administration of G-CSF with or without CD133⁺ hemopoietic stem-cell infusion, failed to improve liver function or to alleviate fibrosis (89). The current study did not focus on plausible paracrine contributions of BM cells to stimulate different liver cell populations, and it remains to be investigated whether BMDMC can instigate liver resident stem cells, either vascular stem cells or oval cells, to accelerate tissue restoration following an injury.

3.2. Resident EC are proliferation-efficient and can restore liver vasculature

To circumvent the effects of irradiation and to unambiguously decipher the cellular source of newly-formed liver vessels post-PHx, the present study employed different non-myeloablative fate mapping tools. In the absence of irradiation, the remaining liver EC could restore the vascular network. In fact, adult quiescent EC actively proliferated during the angiogenic phase of liver regeneration. Similar to partial hepatectomy, liver EC could independently recover following chronic insults such as repeated administration of CCl₄ or adenovirus-mediated liver damage, without any physical contribution of BMDMC. Unlike irradiation, neither partial hepatectomy nor chronic liver damage models affected the fitness of resident liver EC. Hence, the remaining healthy vasculature could successfully restore the functional equilibrium in the liver (Fig. 29).

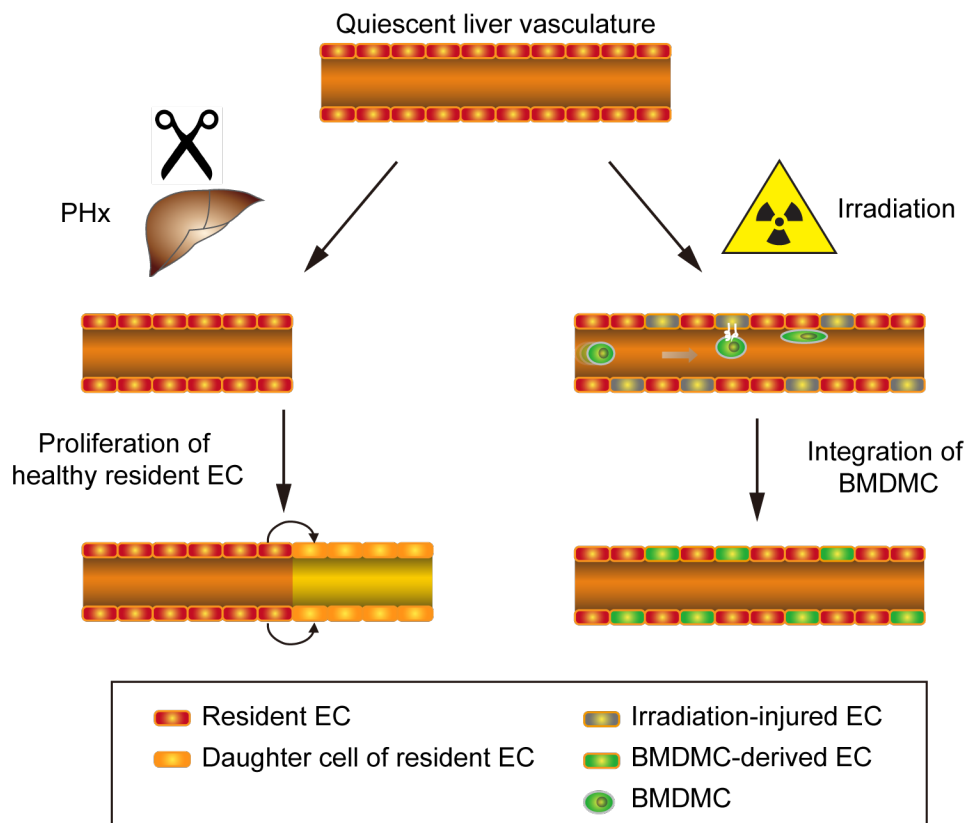


Figure 29. EC fitness dictates the source of regenerating liver vasculature. Under non-damaging conditions such as partial liver resection, healthy remaining resident endothelial cells can proliferate to restore the liver vascular network. However, in a previously-damaged liver, bone marrow-derived stem cells can accelerate the liver recovery by physically integrating into the regenerating vascular tree.

Taken together, by unraveling under which conditions BMDMC may contribute to vascular regeneration, the present study reconciles for many of the discrepancies in the published literature regarding the cellular source of liver neovascularization and concludes that both preexisting liver EC and BMDMC can act as a potential source of new vessels depending on the vascular fitness.

3.3. Temporal evolution of lung EC with metastatic progression

The primary aim of my doctoral project was to establish the systems map of metastatic lung EC. Employing postsurgical LLC spontaneous metastasis model, lung EC were isolated at sequential stage of metastatic disease (i.e., [i] control mice prior to tumor cell inoculation; [ii] mice at time of primary tumor surgery; [iii] mice one week after primary tumor surgery; [iv] mice at a later stage with overt metastases) and were transcriptionally profiled to generate a dynamic map of endothelial changes during lung metastatic colonization. Notably, the temporal approach with surgical removal of the primary tumor facilitated for the first time to formally discriminate between pre-metastatic and metastatic EC gene signatures. The resulting datasets will serve as a versatile tool in future studies to identify and functionally validate novel vascular regulators of early metastatic colonization.

In-depth bulk RNA sequencing analysis of lung EC was complemented with serum proteomics to identify novel angiocrine molecules. I prototypically datamined for secreted angiocrine factors and identified the TGF β pathway specifier LRG1 as an early EC-specific responsive signal that was tightly calibrated to the tumor challenge. Furthermore, transcriptomics at single-cell resolution mapped endothelial heterogeneity and spatial expression of angiocrine instructors in a tumor cell-seeded lung. The single-cell data added another layer of complexity by attributing spatial information, especially about the arterio-venous axis, which would be diluted in bulk RNA-seq analyses. Notably, the high-resolution expression analysis identified widespread regulation of *Lrg1* expression throughout the vascular tree. The vascular endothelium has a huge surface (estimated to be the size of the football field). As such, relatively small transcriptomic changes on a per cell level induced by relatively small primary tumors add up to result in systemic homeostasis altering changes that can proteomically be detected in the circulation. Therefore, the data indicate that primary tumors use the large surface of the body's vascular endothelium as an amplifier of tumor-induced systemically acting angiocrine signals such as LRG1. Additionally, retrospective clinical data revealed higher circulating levels of LRG1 are associated with multiple cancer entities, further bolstering the hypothesis that all organ endothelium contribute to the observed effects. Overall, the concept that the vasculature acts as an amplifier of tumor-induced instructive signals will guide fundamentally novel approaches towards studying systemic angiocrine signaling mechanisms, and also direct future strategies to identify novel prognostic and predictive biomarkers of disease involving the activated endothelium.

Lastly, LRG1 was functionally validated as a pro-metastatic molecule. Systemic upregulation of LRG1 was dispensable for extravasation but facilitated early-stage colonization of tumor cells at distant metastatic sites. Concomitantly, intervention with anti-LRG1 suppressed metastatic progression in

clinically relevant short-term perioperative and long-term postsurgical adjuvant regimens. Recently, a phase I/IIa clinical trial with Magacizumab, a humanized version of anti-LRG1 employed in this study, has been initiated for patients with neovascular age-related macular degeneration. Preclinical data presented here firmly support a crucial role of LRG1 in tumor metastasis and warrant further translational studies of LRG1 as a therapeutic target for metastasis.

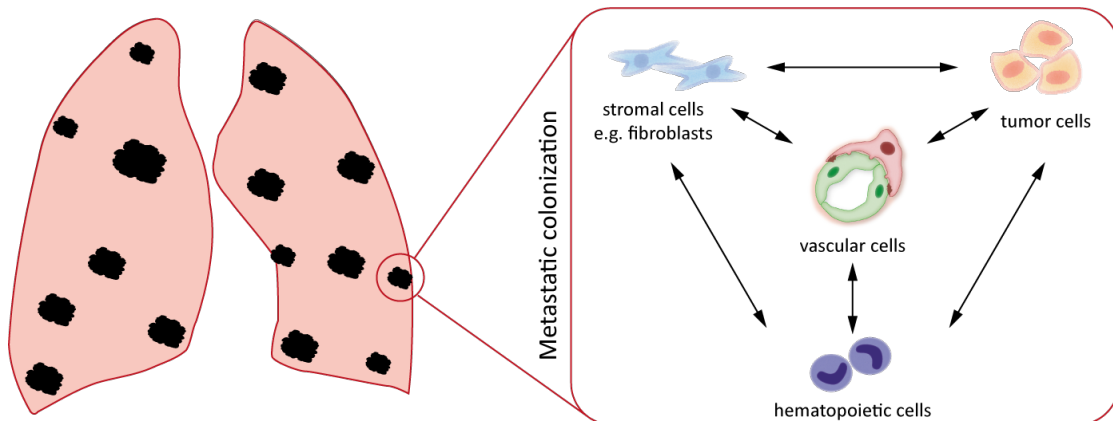


Figure 30. EC-derived angiocrine signals facilitate early metastatic colonization. EC interacts with different cellular components of a distant organ site to prepare a conducive microenvironment for supporting the colonization of disseminated tumor cells.

In conclusion, by establishing comprehensive datasets describing spatio-temporal evolution of metastatic lung EC, the present study provides a platform for future metastasis research and to investigate the multi-facet role of angiocrine signals in orchestrating a metastatic niche. Unexpected, yet, concept-changing finding that endothelium acts as an amplifier of tumor-induced instructive signals will further strengthen the gatekeeper role of blood vessels in maintaining physiological homeostasis.

4. Materials and methods

4.1. Materials

4.1.1. Chemicals

Table 1 Chemical suppliers

Company
AppliChem (www.applichem.com)
Carl Roth (www.carl-roth.de)
Gerbu (www.gerbu.de)
Merck (www.merk.de)
Roche (www.roche-applied-science.com)
Serva (www.serva.de)
Sigma-Aldrich (www.sigmaaldrich.com)

4.1.2. Cells

Table 2 Mouse tumor cell lines

Cells	Description	Company	Medium
LLC	Lewis Lung Carcinoma	ATCC	Dulbecco's Modified Eagle Medium (DMEM) + 10% FCS
B16F10	Melanoma cells	ATCC	Dulbecco's Modified Eagle Medium (DMEM) + 10% FCS

4.1.3. Cell culture reagents

Table 3 Cell culture reagents

Reagent	Company
Dimethylsulfoxide (DMSO)	AppliChem
Dulbecco's phosphate buffered saline (PBS)	PAA
Fetal Calf Serum (FCS, heat inactivated)	PAA
Penicillin/streptomycin (100x 10 ⁴ U/10mg/ml)	PAA
DMEM medium	Gibco
Trypan blue	Gibco

4.1.4. Growth factors, proteins and enzymes

Table 4 Growth factors, proteins and enzymes

Protein	Company
Proteinase K	Gerbu
RNase free DNase	Qiagen

4.1.5. Primers and Oligonucleotides

All primers were purchased from Eurofins.

Table 5 Genotyping primers

Genotype	Primer name	Sequence (5'-3')
<i>Chd5-Cre^{ERT2}</i>	Cre for	CAGGGTGTATAAGCAATCCC
	Cre rev	CCTGGAAAATGCTTCTGTCCG
	actin for	CAATGGTAGGCTCACTCTGGGAGATGATA
	actin rev	AACACACACTGGCAGGACTGGCTAGG
<i>RosaYFP^{KI}</i>	loxP1 for	CAGGCTATCACTGTGACACTGGTAC
	loxP1 rev	AAATACGCAGTTTCAGGGCTGGGA
	loxP2 rev	ACCAATTCGGGGAATCCTATTGGCA
<i>LacZ</i>	LacZ-for	TCCTGGTGGGAGAGGACTC
	LacZ-rev	GTCTGTCCTAGCTTCCTCACTG

4.1.6. TaqMan™ assays

All TaqMan™ assays were purchased from Applied Biosystems.

Table 6 TaqMan™ assays

Gene	Ordering number
<i>Kdr</i>	Mm01222421_m1
<i>Flt1</i>	Mm00438980_m1
<i>Icam2</i>	Mm00494862_m1
<i>Cldn5</i>	Mm00727012_s1
<i>Lrg1</i>	Mm01278767_m1
<i>Mmp2</i>	Mm00439498_m1
<i>Ptgs2</i>	Mm00478374_m1
<i>Vcam1</i>	Mm01320970_m1
<i>Cxcl2</i>	Mm00436450_m1
<i>Ccl2</i>	Mm00441242_m1
<i>Myc</i>	Mm00487804_m1
<i>Pgf</i>	Mm00435613_m1
<i>Il1b</i>	Mm00434228_m1
<i>Il6</i>	Mm01210733_m1
<i>S100a9</i>	Mm00656925_m1
<i>Ednrb</i>	Mm00432989_m1
<i>Actb</i>	Mm01222421_m1
<i>Pecam1</i>	Mm00438980_m1

4.1.7. PCR/RT-qPCR reagents, nucleotides and buffers

Table 7 PCR and RT-qPCR reagents, nucleotides and buffers

Reagent	Company
Direct PCR Lysis Reagent	PeqLab
DNase/RNase free H ₂ O	Gibco
Ethidium bromide	Roth
O'Generuler 100bp Plus DNA ladder	Thermo Fisher Scientific
RedTaq® ReadyMix™ PCR Reaction Mix	Sigma-Aldrich
TaqMan® Fast Advanced PCR Master Mix	Applied Biosystems
SYBR™ Green PCR Master Mix	Applied Biosystems

4.1.8. Antibodies

Table 8 Primary antibodies

Antigen	Reactivity	Species	Dilution	Conjugate	Company	Ordering number
CD3e	mouse	rat	1:150	APC-e780	eBioscience	47-0032
CD4	mouse	rat	1:400	FITC	BioLegend	130308
CD8a	mouse	rat	1:400	PE-Cy5	eBioscience	15-0081
CD11b	mouse	rat	1:200	PE-Cy7	eBioscience	25-0112
CD11c	mouse	Armenian hamster	1:400	PerCP	BioLegend	117326
CD16/32 (Fc-block)	mouse	rat	1:100	-	eBioscience	14-0161-86
CD19	mouse	rat	1:150	PerCP-Cy5.5	BioLegend	115534
CD31	human	mouse	1:200	APC-Cy7	BD Bioscience	563653
CD31	mouse	rat	1:100	-	BD Pharmingen	557355
CD45	human	mouse	1:100	APC	Stemcell Technologies	60018
CD45	mouse	rat	1:400	FITC	BD Pharmingen	553080
CD45	mouse	rat	1:200	PacOrange	Life Technologies	MCD4530
CD45	mouse	rat	1:100	-	Cedarlane labs (Biozol)	CL9446AP
CD45R (B220)	mouse	rat	1:200	PE-Cy7	eBioscience	25-0452
Gr1	mouse	rat	1:100	FITC	BD Pharmingen	553172
Gr1	mouse	rat	1:100	FITC	BD Pharmingen	553172
Ly6C	mouse	rat	1:400	APC-Cy7	Biolegend	128025
Ly6G	mouse	rat	1:400	PacBlue	Biolegend	127612
NG2	mouse	rabbit	1:100	-	Millipore	AB5320
F4/80	mouse	rat	1:100	PE	BioLegend	123110

Table 9 Secondary antibodies

Reactivity	Species	Dilution	Conjugate	Company	Ordering number
goat IgG	rabbit	1:5000	HRP	DAKO	P0160
mouse IgG	rabbit	1:10000	HRP	DAKO	P0260
rabbit IgG	goat	1:200	AF-488	Life technologies	A11070
rabbit IgG	goat	1:500	AF-546	Life technologies	A11071
rabbit IgG	goat	1:5000	HRP	DAKO	P0448
rat IgG	goat	1:200	AF-488	Life technologies	A21049
rat IgG	goat	1:200	AF-546	Life technologies	A11081

4.1.9. Staining reagents

Table 10 Staining reagents

Reagent	Company
Annexin V	eBioscience
Annexin V Binding buffer	eBioscience
CountBright™ Absolute Counting Beads	Thermo Fisher Scientific
Eosin Y solution	DAKO
Fluorescent mounting medium	DAKO
FxCycle - violet	Invitrogen
Histomount	Invitrogen
Hoechst Dye 33258, 1mg/ml	Sigma-Aldrich
Mayers' Hemytoxylin solution	Sigma-Aldrich
Normal goat serum ready-to-use	Zymed
Roti-Histofix 4% (pH 7)	Carl Roth
Tissue-Tek® O.C.T.™ Compound	Scigen

4.1.10. Kits

Table 11 Kits

Reagent	Company
Arcturus™ PicoPure™ RNA Isolation Kit	Applied Biosystems
Click-iT™ EdU Alexa Fluor Flow Cytometry Kit	Thermo Fisher Scientific
GenElute™ Mammalian Total RNA Purification Kit	Sigma-Aldrich
QuantiTect® Reverse Transcription Kit for cDNA Synthesis	Qiagen

4.1.11. Reagents for animal experimentation

Table 12 Reagents for animal experimentation

Reagent	Company
Bepanthen® eye cream	Roche
Histamine	Sigma-Aldrich
Ketavet	Pfizer
NaCl solution	Braun
Rompun	Bayer

4.1.12. Consumables

Table 13 Consumables

Consumable	Company
96 well plates	Steinbrenner Laborsysteme
384 well plates	4titude
Cannula (20G, 27G, 29G, 30G)	BD
Cell culture dishes (10cm)	TPP
Cell scraper	Corning
Cell strainer (40 µm, 100 µm)	BD Falcon
Cotton swab	Edeka elcos face
Countess™ cell counting chamber slides	Invitrogen
Cryotubes	Carl-Roth
FACS tubes	BD Falcon
Filter containing pipette tips	Sarstedt
Microscope cover glasses	VWR international
Microscope glass slides	Menzel-Gläser
Octenisept®	Schülke
Peel-A-Way™ Embedding Molds	Sigma-Aldrich
Pipette tips	Nerbe
Reaction tubes (0.5ml, 1.5ml, 2ml)	Eppendorf
Reaction tubes (15ml, 50 ml)	Greiner
Safety-Multifly® 21G	Sarstedt
Sealing foil	Applied Biosystems
Sterile pipettes	Corning
Syringes	Dispomed
Terumo® Syringe (1 ml, 5ml, 10 ml)	Terumo
Tissue culture 6 well/24 well plates	Sarstedt

4.1.13. Equipments

Table 14 Equipments

Equipment	Company
Agarose gel documentation system	Peqlab
Amersham™ Imager 600	GE Healthcare
Axio ScanZ7.1	Zeiss
BioRad gel casting system	BioRad
BioRad gel running system	BioRad
BioRad Western Blotting equipment	BioRad
Canto II	BD
Cell culture hood	Thermo Fisher Scientific
Cell culture incubator	Thermo Fisher Scientific
Centrifuge	Thermo Fisher Scientific
Countess™ automated cell counter	Invitrogen
Developing cassette Western Blot	Amersham Bioscience
Digital Electronic Caliper	Fine Science Tools
FACS Aria Fusion	BD
Freezing box	Thermo Fisher Scientific
Heating block	Eppendorf
iMark™ Microplate Reader	BioRad
Light cycler 480	Roche
Magnetic stand	Invitrogen
Microtome Hyrax C50	Zeiss
Multistep pipette	Eppendorf
Nanophotometer® N60	INTAS
Pipettes	ErgoOne
Power supply	BioRad
QIAxcel Advanced System	Qiagen
Scale	Ohaus
Special accuracy weighing device	Mettler Toledo
StepOnePlus Real-Time PCR System	Thermo Fisher Scientific
Shaver	Moser
Surgery and dissection tools	Fine Science Tools
Table centrifuge (5417R)	Eppendorf
Thermocycler	Applied Biosystems
UV transilluminator	Intas
Vortex	Neolab
Water bath	Julabo

4.1.14. Softwares

Table 15 Softwares

Software	Company
FACSDiva™	BD
Fiji	ImageJ
FlowJo	Miltenyi Biotec
Genepattern	Broad Institute
Gene Set Enrichment Analysis	Broad Institute
Graph Pad Prism (v5.0, v8.0)	Graph Pad
ImageQuant TL	GE Healthcare
Ingenuity Pathway Analysis	Qiagen
Light Cycler 480 software	Roche
Molecular Signature Database	Broad Institute
StepOne™ Software v2.1	Applied Biosystems
ZEN black	Zeiss
ZEN blue	Zeiss

4.1.15. Solutions and buffers

Table 16 Recipe for preparing solutions and buffers

Buffer		Composition
Acidified water	5% (v/v)	Acetic acid (glacial) in distilled water
	150 mM	NH ₄ Cl
Ammonium chloride potassium buffer (ACK)	10 M	KHCO ₃
	100 mM	Na ₂ EDTA
		adjust pH 7.2-7.4BD
FACS buffer	3% (v/v)	Fetal calf serum in PBS
	1.34 M	NaCl
	27 mM	KCl
Phosphate buffered saline (PBS)	200 mM	Na ₂ HPO ₄
	4.7 mM	KH ₂ HPO ₄
		adjust pH 7.4
Picro-sirius red solution	0.1% (w/v)	Sirius red F3B in saturated aqueous solution of Picric acid
	89 mM	Tris-HCL pH 7.5
Tris-Borate-EDTA buffer (TBE)	89 mM	NaCl
	1 mM	Tween-20
	10 mM	Tris/HCl, pH 7.5
Tris-Buffered Saline Tween-20 (TBS-T)	100 mM	NaCl
	0.1%	Tween-20

4.2. Methods

4.2.1. Mouse experiments

C57BL/6N, FVB/N, and NOD-scid gamma (NSG) mice were purchased from Charles River. CAG-GFP (chicken beta actin promoter and cytomegalovirus enhancer regulates expression of enhanced green fluorescent protein) mice were purchased from JAX laboratory. *Rag2*^{-/-}*γc*^{-/-}*Kit*^{W/W^v} mice were generated as described previously (199). C57BL/6 Rosa-YFP^{fl/fl} mice were crossed with C57BL/6 VECad-Cre^{ERT2} mice to specifically label EC upon tamoxifen application.

Male mice (8-10 weeks of age) were used for the liver experiments and female mice (8-10 weeks of age) were employed for all tumor experiments. All mice were housed on a 12 h light-dark cycle with free access to food and drinking water in SPF animal facilities. All animal experiments were approved by the institutional and governmental Animal Care and Use Committees (G220/11, G164/16, G231/16, G213/17, G219/17, G254/18, G196/18, G9/19, and G196/19 to H.G.A. from Regierungspräsidium Karlsruhe, Germany). All experiments were performed in accordance with the institutional guidance for the care and use of laboratory animals.

4.2.2. Cells

LLC and B16F10 cells (ATCC) were maintained according to ATCC standard culture instructions. LLC cells were transduced with lentivirus to overexpress either *Lrg1* or control vector pLenti. Stably transduced clones were selected with Puromycin. All cells were cultured at 37°C and 5% CO₂ and routinely tested for mycoplasma by PCR.

4.2.3. Tumor models

All mice were routinely checked for the experimental endpoint criteria.

LLC tumor model: LLC cells (1x10⁶ in PBS) were subcutaneously inoculated in C57BL/6N mice. Primary tumors were surgically resected at an average size of 300 mm³. Mice were administered with either anti-LRG1 or control-IgG (50 mg/kg) twice a week. For adjuvant treatment, therapy was initiated one day after tumor resections until the experimental endpoint criteria were reached. For perioperative treatment, therapy was initiated once the primary tumor size reached an average of 150 mm³ until 10 days following primary tumor resection.

MMTV-PyMT tumor model: Bio-banked tumor fragments (~10 mm³ in volume) were orthotopically implanted in the fourth mammary pad of syngeneic FVB/N mice. Primary tumors were surgically resected at an average size of 500 mm³.

B16F10 experimental metastasis assay: C57BL/6N mice were pretreated with one shot of either anti-LRG1 or IgG. 3 days later, B16F10 cells (2x10⁵ in PBS) were injected into the tail vein. Lungs were

collected two weeks after tumor cell inoculation, and metastatic foci were counted under a stereo-microscope.

LRG1 systemic gain-of-function and B16F10 experimental metastasis assay: *Lrg1*-overexpressing or control LLC cells (1×10^6 in PBS) were inoculated subcutaneously in C57BL/6N mice. 7 days later, B16F10 cells (2×10^5 in PBS) were injected into the tail vein. Two weeks later, lungs were collected, and melanoma metastatic foci were counted under a stereo-microscope. In a follow-up experiment, primary LLC tumors were additionally resected 24 h after intravenous injection of B16F10 cells.

4.2.4. Partial hepatectomy

Two-third partial hepatectomy was performed according to the methods described by Mitchell and Willenbring to induce liver regeneration (190). In brief, mice were anaesthetized with a mixture of ketamin (100 mg/kg body weight) and xylazine (10 mg/kg body weight). Then, the left lateral lobe and the median lobe were ligated with 4-0 silk sutures and resected. The mice were kept for ten days to regenerate the lost liver mass. Finally, the mice were euthanized and livers were collected for FACS analysis or immunostaining.

4.2.5. Transplantation of HSC without irradiation

PanRosaYFP mice were used as donors. Bone marrow cells of panRosaYFP mice were flushed from femurs, tibias, coxa and humeri using PBS supplemented with 5% heat-inactivated FCS. Cells were filtered through a 40- μ m cell strainer (Falcon). Fc receptors were blocked by incubating cells in 5% FCS with purified mouse IgG (500 mg/ml, Jackson ImmunoResearch Laboratories). All stainings were performed in 5% FCS on ice for 30 min with optimal dilutions of commercially-prepared antibodies. Reagents used were CD3 ϵ phycoerythrin (PE) (145-C11), CD8 PE (53-6.7), CD11b PE (M1/70), CD19 PE (ID3), CD45R PE (RA3-6B2), CD117 eFluor780 (2B8), Sca-1 PerCP-Cy5.5 (D7) (eBiosciences), CD4 PE (H129.19), CD8a PE (53-6.7), CD19 PE (1D3), Gr-1 PE (RB6-8C5), NK1.1 PE (PK136) and Ter119 PE (Ter119) (BD Pharmingen). The lineage cocktail (Lin) was composed of CD3 ϵ , CD4, CD8a, CD11b, CD19, CD45R, Gr-1, NK1.1 and Ter119. Dead cells were excluded by staining with Sytox Blue (Invitrogen). Approximately 5000 LSK cells were sorted by FACS Aria III (Becton & Dickinson) and injected intravenously into non-irradiated triple transgenic *Rag2*^{-/-} *γ c*^{-/-}*Kit*^{W/W^v} recipient mice. Donor chimerism of blood cells was determined one-month post-transplantation.

4.2.6. Irradiation-preconditioned bone marrow chimeric mice

Eight weeks old WT mice were lethally irradiated with a total dose of 9 Gy (split dose, 2x 4.5 Gy). After a 2 h rest, the mice were injected with bone marrow cells or 5000 LSK cells isolated from CAG-GFP transgenic mice via the tail vein. One month later, mice were subjected to 2/3 partial hepatectomy

(PHx). The resected liver lobes were isolated and subjected to FACS analysis and cryopreservation respectively. Ten days after PHx, the regenerated livers were resected and analyzed. Donor chimerism in the bone marrow of recipient animals was determined after sacrificing animals.

Lrg1-KO bone marrow chimeric mice. BM cells were isolated from *Lrg1*-KO or wild-type littermate mice. Genotyping PCR for *LacZ* (forward primer: TCCTGGTGGGAGAGGACTC; reverse primer: GTCTGTCCTAGCTTCCTCACTG) was performed to ensure the knockout of *Lrg1*. 8-wk-old WT mice were lethally irradiated with a total dose of 9 Gy (split dose, 2 × 4.5 Gy). After a 2 h rest, mice were injected with *Lrg1*-KO/WT bone marrow cells, consisting of approximately 5000 LSK cells, via the tail vein. 2 months later, LLC metastasis experiment was performed in BM chimeras. Leukocyte chimerism of recipient animals was determined by analyzing *Lrg1* gene expression in splenocytes after sacrificing animals.

4.2.7. Microarray analysis

For gene expression analysis, microarrays were performed by the DKFZ Genomics core facility. Briefly, liver EC were isolated from irradiation-conditioned bone marrow chimeric mice for surface marker expression (DAPI⁻ CD45⁻ CD31⁺ CD146⁺). Further, liver EC were segregated based on YFP expression (YFP⁻: resident liver EC; YFP⁺: bone marrow-derived liver EC). Thereafter, RNA was isolated with the Arcturus PicoPure RNA isolation kit (Life Technologies) and RNA quality and quantity were analyzed on an Agilent Bioanalyzer. Next, cDNA was hybridized on mouse Clariom S assay (Applied Biosystems) according to the manufacturer's protocol. Microarray data were normalized and analyzed with the Chipster software. The microarray data with the description are deposited under GEO accession number GSE116377.

4.2.8. Constitutive labeling of EC in *VECad-Cre^{ERT2}xRosa-YFP^{fl/fl}* mice

4-5 weeks old animals were administered four doses of tamoxifen (100 mg/kg) twice a week. The animals were rested for 1 month after tamoxifen application. Next, mice were subjected to 2/3rd partial hepatectomy (PHx). The resected and regenerated liver lobes of an individual mouse were analyzed with flow cytometry. To label the proliferating liver EC post-PHx, EdU (40 mg/kg) was administered intraperitoneally daily during the angiogenic phase of liver regeneration (day 2-6). The regenerated liver lobes were stained with EdU flow cytometry kit (Baseclick GmbH) and analyzed by FACS.

4.2.9. Chronic liver injury models

The carbon tetrachloride (CCl₄) model: *VECad-Cre^{ERT2}xRosa-YFP^{fl/fl}* mice with labeled EC were intraperitoneally injected with either peanut oil alone or in combination with CCl₄ (0.7 μl / g body weight) thrice a week for a duration of four weeks (241). After the last treatment, mice were allowed

to recover for two weeks and thereafter, mice were euthanized and livers were collected for FACS analysis or immunostaining. Mice were bled and plasma ALT/AST levels were monitored during the course of the experiment.

Adenovirus-mediated liver damage: *VECad-Cre^{ERT2}xRosa-YFP^{f1/f1}* mice with labeled EC were intravenously injected with either PBS or 10¹¹ viral particles of empty replication-deficient adenovirus (VectorBuilder Inc. VB180308-1016nff). Afterward, mice were bled at regular intervals and plasma ALT/AST levels were monitored. Once the ALT/AST levels have subsided, mice were euthanized and livers were collected for FACS analysis or immunostaining.

4.2.10. Regenerative therapy

Direct infusion of YFP-labeled stem cells: The whole bone marrow cells were isolated from PanRosaYFP mice as described above. On day two after PHx or sham-operation, the NSG mice were injected intravenously with suspension of bone marrow cells (consisting of 20000 LSK cells). After eight days, the mice were euthanized and blood as well as livers were collected for FACS analysis or immunostaining.

G-CSF mediated bone marrow-derived progenitor mobilization: On day two after PHx or sham-operation, the mice were injected with 100 µg of Neulasta (PEG-G-CSF) subcutaneously. After eight days, the mice were euthanized and bone marrow, blood and livers were collected for FACS analysis or immunostaining.

4.2.11. Flow cytometry analysis

Blood chimerism: Blood samples were drawn from the tail veins and kept in anticoagulant EDTA-K2 coated tubes. Erythrocytes were lysed with 1x ACK (Ammonium Chloride Potassium) lysis buffer and the remaining cells were collected by centrifugation at 500 g for 5 min. Cells were resuspended with PBS and analyzed by flow cytometry. Cells were gated based on size and granularity. Then the percentage of YFP⁺/GFP⁺ cells within the mononuclear population was determined.

Liver EC incorporation: Livers were collected and minced into small pieces and incubated with collagenase I buffer (collagenase I 200 U/ml, CaCl₂ 0.01%, DNase 1.25% in DMEM medium) for 30 min at 37°C with agitation. The cell suspension was filtered through a 100 µm cell strainer before being centrifuged twice at 50 g for 2 min to remove the hepatocytes. The cell suspension was further treated with 5 ml 1x ACK lysis buffer to remove erythrocytes. After centrifugation, the cells were incubated in staining solution with antibodies CD45-PE (BD Pharmingen #561087), CD45-APC-Cy7 (BD Pharmingen #557659), CD31-APC (BD Pharmingen #551262), CD133-FITC (ebioscience #11-1331-82) and CD146-PerCP-Vio700 (Miltenyi Biotec #130-103-865). All stainings were performed in 5% FCS (in PBS) on ice for 30 min with optimal dilutions of commercially-prepared antibodies. For FACS analysis, DAPI positive dead cells were first excluded and CD45⁺CD31⁺CD146⁺ population were defined as liver EC. Finally, the

percentage of GFP or YFP positive cells in the liver EC population was measured using either BD Canto-II or Aria Fusion platform.

EC isolation: Tissues were dissociated into single cell suspension with Liberase digestion enzyme mix (Roche). For brain, the single cell suspension was mixed with 22% bovine serum albumin in distilled water and centrifuged at 1300g for 15 mins to remove myelin. Thereafter, EC were enriched using CD31 microbeads (Miltenyi Biotec) according to the manufacturer's instructions. Enriched EC were further FACS sorted for the surface marker profile CD45⁺LYVE1⁺PDPN⁺TER-119⁻CD31⁺ using fluorescence-conjugated antibodies [CD45 (30-F11), CD31 (MEC 13.3), PDPN (eBio8.1.1), TER-119 (TER-119), and LYVE1 (ALY7)].

FACS-based immunophenotyping: In LLC metastasis model, lung and spleen tissues were collected at sequential stages of tumor progression. Lung tissue was dissociated into a single cell suspension with Liberase digestion enzyme mix (Roche). Spleen tissue was mechanically dissociated into single cell suspension. Following Erythrocyte lysis, the remaining single cell solution was divided for lymphoid [CD45 (30-F11), CD3 ϵ (17A2), CD4 (GK1.5), CD8a (53–6.7), CD45R-B220 (RA3-6B2), and NK- 1.1 (PK136)] and myeloid [CD45 (30-F11), CD11b (M1/70), Ly-6C (HK-1.4), Ly-6G (1A8), F4/80 (BM8), and CD11c (N418)] staining. Dead cells were excluded by FxCycle Violet staining. Stained cells were analyzed using a BD bioscience Aria cell sorting platform, and frequency of individual cell populations was quantified with FlowJo software.

4.2.12. Bulk RNA-sequencing and data analysis

Lung EC were isolated from four biological replicates at each stage of tumor progression and total RNA was isolated using Arcturus PicoPure RNA isolation kit (ThermoFisher Scientific) according to the manufacturer's instructions. Quality control was performed by Bioanalyzer (Agilent) measurements. The sequencing library was generated with 10 ng of total RNA using the SMARTer Ultra Low RNA kit for Illumina sequencing (Clontech) according to the manufacturer's protocol. Sequencing reads (100 bp Paired-End) were generated on the HiSeq2000 platform (Illumina) with four samples per lane. The sequenced reads were aligned to the mouse reference genome mm10 using STAR aligner (242). Differential gene expression was computed using DEseq2 (243). Only transcripts with an RPKM \geq 1 in at least one sample were considered for the downstream analysis. Gene Set Enrichment Analysis (GSEA) and Ingenuity Pathway Analysis (IPA) were undertaken to study regulated molecular pathways and corresponding biological functions. Bulk RNA-seq data have been deposited in the Gene Expression Omnibus under accession number GSE131072.

4.2.13. Single-cell RNA-sequencing

Lung EC were isolated from four biological replicates at each stage of tumor progression. Cell suspensions, consisting of randomly-selected 10,000 cells, for each time point, were separately loaded

on a Chromium Single Cell Instrument (10X Genomics). Single-cell RNA-seq libraries were prepared using Chromium Single cell 3' Library (v2), Gel beads & Multiplex kit (10X Genomics). Multiplexed libraries were sequenced on the HiSeq4000 platform (Illumina).

scRNA-seq data processing: The sequenced data were aligned to the mouse reference genome (mm10) using Cell Ranger (version 2.1.1), thereby generating gene-barcode matrices. Low-quality cells, containing less than 200 detected genes or mitochondrial genes accounting for more than 10% of total transcripts, were filtered out. Outlying cells were identified by three median absolute deviations away from the median through scater R package (version 1.10.1). After the quality control, Seurat R package (version 2.3.4) was used for further analysis (244). All quality-controlled samples (9036 cells) were integrated with Seurat. Highly variable genes were selected based on the dispersion of more than 0.5 and an average expression between 0.0125 and 4. The number of UMI varied among cells was regressed out with a linear model.

Unsupervised Clustering and visualization: We reduced dimensions of data using principal component analysis. First 28 principal components were chosen at the elbow of the curve using PCElbowPlot function and were used for the subsequent analysis. Initial unsupervised clustering with FindClusters function at resolution 0.4 yielded 11 clusters. Differentially expressed genes of each cluster were identified with FindAllMarkers function. Uniform Manifold Approximation and Projection (UMAP) was employed for data visualization.

Biologically-supervised annotation and filtering: We manually annotated unsupervised clusters based on previously-known markers of different cell types. Three clusters were identified as contaminants (mural cells, lymphatic EC, and cells with high expression of ribosomal genes) and excluded for further analysis. Thereafter, 8512 cells were reanalyzed for differential gene expression and re-clustered. Seven principal components were chosen, and nine unsupervised clusters were identified. We further merged five clusters that were weakly-distinguishable and embedded closely in UMAP. Altogether, we detected five clusters as indicated. Single-cell RNA-seq data have been deposited in the Gene Expression Omnibus under accession number GSE131110.

4.2.14. Serum Proteomics

Sample and library preparation: Protein concentration in serum samples was measured with Bicinchoninic Acid (BCA) assay according to the manufacturer's protocol (Thermo Fisher Scientific). Samples were prepared according to previously published protocol (245). Briefly, 50 µg of protein were diluted in a total volume of 100 µL of 0.1% (w/v) RapiGest-SF (Waters) dissolved in 50 mM ammonium bicarbonate (ABC) (pH 8) and heated for 15 min at 95°C. Prior to protein digestion disulfide bonds were reduced using Dithiothreitol (DTT, 5 mM final concentration) for 30 min at 60°C and subsequently alkylated with 2-Chloroacetamide (CAA, 15 mM final concentration) for 30 min at room temperature (RT). Proteolytic digestion was performed with trypsin (sequencing grade modified, Promega) in a protease-to-protein ratio of 1:50 (w/w) overnight at 37°C, shaking at 700 rpm. Following digestion,

Trifluoroacetic acid (TFA) was added (pH < 2) to a final concentration of 1% and incubated for 20 min at 37°C to stop digestion and break down RapiGest, followed by centrifugation at 20,000g for 10 min. The peptide containing supernatants were collected in new tubes. MS injection-ready samples were stored at -20°C. For relative quantification, samples were subjected to LC-MS analysis in single shots. Additionally, a library of protein identification was generated by deep fractionating a pool of all samples, using high pH reverse phase liquid chromatography.

Library fractionation: The pooled library-sample was adjusted to pH 10 with Ammonium Formate at a final concentration of 20 mM. Peptide fractionation was performed on a 1200 Infinity HPLC system (Agilent) with a Gemini C18 column (3 μ m, 110 Å, 100 \times 1.0 mm; Phenomenex) using a linear 60 min gradient from 0% to 35% (v/v) ACN in 20 mM Ammonium Formate (pH 10) at a flow rate of 0.1 mL/min. Sixty 1-min fractions were collected, and pooled into twelve fractions, dried, and reconstituted in 0.1% Formic Acid (FA). MS injection-ready samples were stored at -20°C.

LC-MS Analysis: The single shot samples and 12 library fractions were injected using an Easy-nLC 1200 nano-UPLC (Thermo Fisher Scientific) onto a trap column (Pepmap, 100 μ m \times 2cm, C18, 5 μ m 100Å pores) at a constant flow of solvent A (0.1% FA in water) at a maximum pressure of 800 bar, and separated on an analytical column (PepMap RSLC 75 μ m \times 50 cm, C18, 2 μ m, 100Å) at a constant flow of 0.3 μ l/minute, at 55°C by applying a multistep gradient. During elution, the percentage of solvent B (0.1% FA, 80% ACN 19.9% water) was increased linearly from 3% to 8% in 4 minutes, then from 8% to 10% in 2 minutes, then from 10% to 32% in further 17 minutes, and then to 50% B in 3 minutes. Finally, the gradient was finished with 8 minutes at 100% solvent B, followed by 11 minutes 97% solvent A.

Eluting peptides were electro-sprayed by applying 2 kV on a 360 μ m OD \times 20 μ m ID; 10 μ m Picotip coated emitter (New Objective) into a Q Exactive HF quadrupole mass spectrometer (Thermo Fisher Scientific). The capillary temperature was set to 275°C. The mass spectrometer was operated in data dependent mode of acquisition. Briefly, for each cycle, one Full MS spectrum was acquired in the Orbitrap with a mass range of 350-1500 m/z and a resolution of 60,000 FWHM at 200 m/z. The automated gain control (AGC) target was set to 3×10^6 with a maximum injection time of 32 ms. Precursor ions were filtered according to charge state (required 2-7 z) and monoisotopic peak assignment. The top 20 most abundant ions per full scan were selected for an MS2 acquisition. Previously interrogated precursors were excluded using a dynamic exclusion window (40 s \pm 10 ppm tolerance). For MS2 scans the resolution was set to 15,000 FWHM with an AGC of 1×10^5 ions and maximum fill time of 50 ms.

MS Data processing and protein identification: The mass spectra were processed with MaxQuant (V1.5.1.2) using the Andromeda search engine against UniProtKB/Swiss-Prot databases of *Mus musculus* (13.09.2017), with the following search settings: digestion enzyme was set to trypsin/P, with a maximum of two missed cleavages allowed (246, 247). Precursor and product ion tolerances were set at 20 ppm and 0.5 Da, respectively. Carbamidomethylation of cysteine was set as a fixed modification, oxidation of methionine and acetylation (protein N-term) were set as variable

modification. The match between run function was enabled to match from the “library” to the “single shot samples” with a time window of 0.7 min and an alignment window of 20 min. A minimum of one unique peptide and a false discovery rate below 0.01 was set for peptide and protein identification. The protein quantification was performed using the label-free quantification algorithm of MaxQuant.

As a decoy database reversed sequences of the target database were used. If not stated otherwise, MaxQuant settings were left as default. For identification of differentially expressed proteins the LFQ values extracted from the protein groups table were used and Linear Models for Microarray Data (Limma, Version 3.36.2; Rstudio, Version 1.1.456), with a p-value below 0.05 was performed. The mass spectrometry data files have been deposited to the ProteomeXchange Consortium under the accession number PXD013978 (248).

4.2.15. Hematoxylin and eosin staining

Tissue sections were hematoxylin and eosin (H&E) stained to visualize respective tissue architecture. Sections were thawed for 3 min at RT and fixed for 10 min at -20°C in methanol. Next, slides were washed two times in VE-water and incubated in freshly filtered Hemalaun for 4 min, washed with running tap water for up to 10 min, washed in VE-water and stained with 1% ethanoic eosin for 2 min. Following three times of washing with VE-water, sections were dipped into graded ethanol series (70%-80%-99%), isopropanol and xylol. Slides were mounted with Histomount and bright field images were acquired with the Zeiss Cell Observer or the Zeiss AxioScan slide scanner.

4.2.16. Immunofluorescence stainings and analysis

Livers were fixed in 4% PFA overnight. 50 µm sections were prepared with a vibratome. Sections were blocked and permeabilized with PBS containing 10% normal donkey serum and 0.3% Triton for 2 h at room temperature. Sections were then incubated with primary antibodies overnight at 4°C, followed by fluorophore-conjugated secondary antibodies for 2 h at room temperature. Images were taken with Leica SP8 confocal microscope. The following antibodies were used in this study: rabbit anti-mouse Lyve-1 (Reliatech, #103-PA50AG), hamster anti-mouse CD31 (Thermo Scientific, MA3105), Rabbit anti-mouse Cleaved Caspase-3 (Cell signaling technology, 9661), Rabbit anti-mouse Phospho-Histone H2A.X (Cell signaling technology, 9718), Rabbit anti-mouse Ki-67 (Cell signaling technology, 12202), Rabbit anti-mouse collagen-IV (polyclonal, Abcam), Rat anti-mouse CD133-FITC (ebioscience #11-1331-82), Rat anti-mouse CD45 (Cedarlane labs #CL9446AP), donkey anti-rabbit IgG-Rhodamine Red-X (Jackson Immunolaboratory, 711-296-152), donkey anti-rabbit IgG-Alexa Fluor® 647 (Jackson Immunolaboratory, 711-606-152), goat anti-american hamster IgG-Rhodamine Red-X (Jackson Immunolaboratory, 127-295-160) and goat anti-american hamster IgG-Alexa Fluor® 488 (Jackson Immunolaboratory, 127-545-160). All stainings were performed with optimal dilutions recommended by manufacturer.

Primary tumors and lung tissues were embedded in Tissue-Tek OCT compound and were cut into 5-7 μm sections. Tissue sections were fixed in ice-cold methanol and were blocked using 10% ready-to-use normal goat serum (Thermo Fisher Scientific). The tissue sections were then incubated overnight at 4°C with primary antibodies [rat anti-CD31 (BD Biosciences, catalog 550300); rabbit anti-Desmin (Abcam, catalog Ab15200-1); and rat anti-CD45 (Cedarlane labs, catalog CL9446AP)]. Staining with the secondary antibodies [anti-rat A488, anti-rabbit A546, and anti-rat A546 Abs (Thermo Fisher Scientific)] was performed next day for 1 h at room temperature. Thereafter, tissue sections were incubated with PE-conjugated antibodies [CD3 ϵ (17A2); CD4 (GK1.5); CD8a (53–6.7); CD11b (M1/70); Gr-1 (RB6-8C5)] for co-staining. Cell nuclei were stained with Hoechst (Merck- Sigma). Images were taken using a Zeiss AxioScan slide scanner, and image analysis was performed using FIJI software.

4.2.17. Gene expression analysis

Total RNA was extracted from the livers of irradiated or hepatectomized mice, using Trizol isolation system (Thermo Scientific) according to the manufacturer's instructions. RNA was transcribed into cDNA using the Quantitect reverse transcription kit (Qiagen). qPCR was performed with SYBR™ Green Master Mix (Thermo Fisher Scientific). Primers (Bax – AGACAGGGGCCTTTTGCTAC (forward) and AATTCGCCGAGACTCG (reverse); Icam1 – CTGGATCTCAGGCCGCAAG (forward) and TGTCGAGCTTTGGGATGGTAG (reverse)) were order from Eurofins.

Total RNA was transcribed into cDNA using the Quantitect reverse transcription kit (Qiagen). Quantitative PCRs were performed with Taqman master mix (Thermo Fisher Scientific). Taqman primers were ordered from Thermo Fisher Scientific. Gene expression levels were calculated based on the $\Delta\Delta\text{Ct}$ relative quantification method. mRNA levels were normalized to Actb or Pecam1 expression as indicated.

4.2.18. Statistical analysis

Statistical analysis was performed using GraphPad Prism (GraphPad Software). Data are expressed as the mean \pm SD. For all temporal analyses, different time points were compared with d0 samples. Employed statistical tests are indicated in corresponding figure legends. A p-value of less than 0.05 was considered statistically significant.

Abbreviations

γ_c	Common gamma chain of the IL2R
μ	Micro (10^{-6})
(c)DNA	(Complementary) Deoxyribonucleic acid
(m)RNA	(Messenger) Ribonucleic acid
(N)ES	(Normalized) Enrichment score
(q)PCR	(Quantitative) Polymerase chain reaction
ABC	Ammonium bicarbonate
ACK	Ammonium chloride potassium
ACTB	Beta-Actin
ADAM	A disintegrin and metalloproteinases
AGM	Aortic-gonado-mesonephros
ALK	Activin receptor-like kinase
ALT	Alanine transaminase
ANG/ANGPT	Angiopoietin
APC	Allophycocyanin
AST	Aspartate transaminase
ATCC	American type culture collection
AV	Adenovirus
BAX	BCL2 associated X
BCA	Bicinchoninic Acid
bFGF	Basic fibroblast growth factor
BIRC5	Baculoviral IAP repeat-containing protein 5
BM	Bone marrow
BMDMC	Bone marrow-derived mononuclear cells
CAA	2-Chloroacetamide
CAG	Chicken beta actin promoter and cytomegalovirus enhancer
CC3	Cleaved caspase 3
CCL	C-C motif chemokine ligand
CCl ₄	Carbon tetrachloride
CCR	C-C Motif Chemokine Receptor
CD	Cluster of differentiation
CDK1	Cyclin Dependent Kinase 1
CKS2	CDC28 Protein Kinase Regulatory Subunit 2
CLDN5	Claudin 5
CO ₂	Carbon dioxide
COL	Collagen
CSF	Colony stimulating factor
CXCL	C-X-C motif chemokine ligand
CXCR	C-X-C motif chemokine receptor
Cy	Cyanine
Da	Dalton
DAPI	4',6-diamidino-2-phenylindole
DARC	Duffy Antigen/Chemokine Receptor

DESeq	Differential expression analysis for sequence count data
DLL	Delta-like
DMEM	Dulbecco's modified Eagle's medium
DMN	Dimethylnitrosamine
DMSO	Dimethyl sulfoxide
DNase	Deoxyribonuclease
DTT	Dithiothreitol
E	Embryonic day
EC	Endothelial cells
EDNRB	Endothelin receptor type B
EdU	5-ethynyl-2'-deoxyuridine
EFNB2	Ephrin B2
EGFP	Enhanced green fluorescent protein
EMP	Erythro-myeloid progenitors
EPC	Endothelial progenitor cells
FA	Formic acid
FACS	Fluorescence activated cell sorting
FBLN5	Fibulin 5
FC	Log ₂ fold change
FCS	Fetal calf serum
FDA	Food and drug administration
FIJI	FIJI is just ImageJ
FITC	Fluorescein isothiocyanate
FOV	Field of view
FOXA2	Forkhead box A2
FUT	Fucosyltransferase
FVB	Friend leukemia virus B
G-CSF	Granulocyte-colony stimulating factor
GEMM	Genetically-engineered mouse model
GEO	Gene expression omnibus
GOF	Gain-of-function
GSEA	Gene set enrichment analysis
Gy	Grays
h	Hours
H&E	Hematoxylin and eosin
H2A.X	Histone H2A.X
HB-EFG	Heparin binding EGF like growth factor
HSC	Hematopoietic stem cell
HUVEC	Human umbilical vein endothelial cells
i.p.	Intraperitoneal
i.v.	Intravenous
iBAQ	Intensity based absolute quantification
ICAM	Intercellular adhesion molecule
IF	Immunofluorescence

Abbreviations

IFL	Irinotecan, bolus fluorouracil, and leucovorin
IGF1R	Insulin like growth factor 1 receptor
IgG	Immunoglobulin G
IL	Interleukin
IPA	Ingenuity pathway analysis
ITGB	Integrin subunit beta
JAG1	Jagged 1
k	Kilo
KEGG	Kyoto encyclopedia of genes and genomes
KITLG	KIT ligand
KO	Knock-out
LC-MS	Liquid chromatography–mass spectrometry
LLC	Lewis lung carcinoma
LOF	Loss-of-function
Log ₂	Binary logarithm
LRG1	Leucine rich alpha-2-glycoprotein 1
LSEC	Liver sinusoidal endothelial cells
LSK	Lin-Sca-1+Kit+
LYVE1	Lymphatic vessel endothelial hyaluronan receptor 1
m	Meter
m/z	Mass-to-charge ratio
MCT	Monocrotaline
MELD	Model for end-stage liver disease
MGP	Matrix gla protein
min	Minutes
Mm10	Mus musculus (house mouse) genome assembly GRCm38
MMP	Matrix metalloproteinase
MMTV-PyMT	Mouse mammary tumor virus-polyoma middle tumor-antigen
MRI	Magnetic resonance imaging
n	Nano (10 ⁻⁹)
N1ICD	NOTCH1 intracellular domain
ND	Non-detectable
NR2F2/COUP-TFII	Nuclear Receptor Subfamily 2 Group F Member 2
NS	Non-significant
NSG	NOD scid gamma
NTF3	Neurotrophin 3
OS	Overall survival
PBS	Phosphate buffered saline
PCA	Principal component analysis
PD-EGF	Platelet-derived endothelial growth factor
PDPN	Podoplanin
PE	Phycoerythrin
PECAM1	Platelet and endothelial cell adhesion molecule 1
PerCP	Peridinin chlorophyll protein
PFA	Paraformaldehyde

PFS	Progression-free survival
PGF	Placental Growth Factor
PHx	Partial hepatectomy
PLAT	T-Plasminogen Activator
PLGF	Placental growth factor
PNx	Partial pneumonectomy
PPM	Parts per million
PROM1	Prominin 1
PTGS2	Prostaglandin-endoperoxide synthase 2
RAG2	Recombination activating 2
RNA-seq	Ribonucleic acid sequencing
RNase	Ribonuclease
RPKM	Reads per kilobase of transcript, per million mapped reads
RT	Room temperature
RTK	Receptor tyrosine kinase
s.c.	Subcutaneous
S100A9	S100 calcium binding protein A9
SD	Standard deviation
SDF1	Stromal cell-derived factor 1
SEM	Standard error of the mean
SMT	Standard medical therapy
SPC	Sinusoid progenitor cells
STAT3	Signal transducer and activator of transcription 3
TBE	Tris-Borate-EDTA buffer
TBS-T	Tris-buffered saline Tween-20
TFA	Trifluoroacetic acid
TGF β	Transforming growth factor beta
TOP2A	DNA topoisomerase II alpha
U/L	Units per litre
UMAP	Uniform manifold approximation and projection
UMI	Unique molecular identifier
v/v	Volume-to-volume ratio
VCAM1	Vascular cell adhesion molecule 1
VE-water	vollentsalztes Wasser / Distilled water
VECad/Cdh5	Vascular endothelial cadherin 5
VEGF(R)	Vascular endothelial growth factor (receptor)
VPF	Vascular permeability factor
VWF	Von Willebrand factor
w/v	Mass-to-volume ratio
YFP	Yellow fluorescent protein

Publications

1. Singhal M^{*,#}, Gengenbacher N^{*}, Abdul Pari AA^{*}, Hai L, Kuhn B, Kallenberg DM, Besemfelder E, Leuchs B, Mogler C, Krijgsveld J, Schlesner M, Hu J, Moss SE, Greenwood J, Augustin HG[#] Temporal multi-omics identifies LRG1 as a vascular niche instructor of early metastatic colonization. *submitted* (*equally contributing, #joint corresponding authors)
2. Singhal M^{*}, Gengenbacher N^{*}, La Porta S^{*}, Gehrs S, Bodenmiller DM, Fischl A, Schieb B, Besemfelder E, Chintharlapalli S, Augustin HG Preclinical validation of a novel metastasis-inhibiting Tie1 function-blocking antibody. *submitted* (*equally contributing authors)
3. Singhal M^{*}, Liu X^{*}, Inverso D, Jiang D, Dai J, He H, Bartels S, Li W, Abdul Pari AA, Gengenbacher N, Besemfelder E, Hui L, Augustin HG[#], Hu J[#] (2018) Endothelial cell fitness dictates the source of regenerating liver vasculature. **J Exp Med** 215(10): 2497-2508 (*equally contributing, #joint corresponding authors)
4. La Porta S, Roth L, Singhal M, Mogler C, Spegg C, Schieb B, Qu X, Adams RH, Bladwin HS, Savant S, Augustin HG (2018) Endothelial Tie1-mediated angiogenesis and vascular abnormalization promote tumor progression and metastasis. **J Clin Invest** 128(2): 834-845
5. Gengenbacher N^{*}, Singhal M^{*}, Augustin HG (2017) Preclinical mouse solid tumour models: status quo, challenges and perspectives. **Nat Rev Cancer** 17: 751-765 (*equally contributing authors)
6. Rios Garcia M, Steinbauer B, Srivastava K, Singhal M, Mattijssen F, Maida A, Christian S, Hess-Stumpp H, Augustin HG, Muller-Decker K, Nawroth PP, Herzig S, Berriel Diaz M (2017) Acetyl-CoA carboxylase 1-dependent protein acetylation controls breast cancer metastasis and recurrence. **Cell Metab** 26: 842-855 e5

References

1. R. H. Adams, K. Alitalo, Molecular regulation of angiogenesis and lymphangiogenesis. *Nat Rev Mol Cell Biol* **8**, 464-478 (2007).
2. H. G. Augustin, G. Y. Koh, Organotypic vasculature: From descriptive heterogeneity to functional pathophysiology. *Science* **357**, (2017).
3. J. M. Butler, H. Kobayashi, S. Rafii, Instructive role of the vascular niche in promoting tumour growth and tissue repair by angiocrine factors. *Nat Rev Cancer* **10**, 138-146 (2010).
4. M. Potente, H. Gerhardt, P. Carmeliet, Basic and therapeutic aspects of angiogenesis. *Cell* **146**, 873-887 (2011).
5. S. Rafii, J. M. Butler, B. S. Ding, Angiocrine functions of organ-specific endothelial cells. *Nature* **529**, 316-325 (2016).
6. H. S. Baldwin, Early embryonic vascular development. *Cardiovasc Res* **31 Spec No**, E34-45 (1996).
7. S. Patan, Vasculogenesis and angiogenesis. *Cancer Treat Res* **117**, 3-32 (2004).
8. O. Cleaver, D. A. Melton, Endothelial signaling during development. *Nat Med* **9**, 661-668 (2003).
9. J. D. Coffin, J. Harrison, S. Schwartz, R. Heimark, Angioblast differentiation and morphogenesis of the vascular endothelium in the mouse embryo. *Dev Biol* **148**, 51-62 (1991).
10. C. J. Drake, P. A. Fleming, Vasculogenesis in the day 6.5 to 9.5 mouse embryo. *Blood* **95**, 1671-1679 (2000).
11. T. J. Poole, J. D. Coffin, Vasculogenesis and angiogenesis: two distinct morphogenetic mechanisms establish embryonic vascular pattern. *J Exp Zool* **251**, 224-231 (1989).
12. L. Pardanaud, C. Altmann, P. Kitos, F. Dieterlen-Lievre, C. A. Buck, Vasculogenesis in the early quail blastodisc as studied with a monoclonal antibody recognizing endothelial cells. *Development* **100**, 339-349 (1987).
13. L. Pardanaud, F. Yassine, F. Dieterlen-Lievre, Relationship between vasculogenesis, angiogenesis and haemopoiesis during avian ontogeny. *Development* **105**, 473-485 (1989).
14. W. Risau, I. Flamme, Vasculogenesis. *Annu Rev Cell Dev Biol* **11**, 73-91 (1995).
15. M. R. Swift, B. M. Weinstein, Arterial-venous specification during development. *Circ Res* **104**, 576-588 (2009).
16. H. M. Eilken, R. H. Adams, Dynamics of endothelial cell behavior in sprouting angiogenesis. *Curr Opin Cell Biol* **22**, 617-625 (2010).
17. L. K. Phng, H. Gerhardt, Angiogenesis: a team effort coordinated by notch. *Dev Cell* **16**, 196-208 (2009).
18. C. Korn, H. G. Augustin, Mechanisms of Vessel Pruning and Regression. *Dev Cell* **34**, 5-17 (2015).
19. H. G. Augustin, Tubes, branches, and pillars: the many ways of forming a new vasculature. *Circ Res* **89**, 645-647 (2001).
20. S. Patan *et al.*, Vascular morphogenesis and remodeling in a model of tissue repair: blood vessel formation and growth in the ovarian pedicle after ovariectomy. *Circ Res* **89**, 723-731 (2001).

21. S. Patan *et al.*, Vascular morphogenesis and remodeling in a human tumor xenograft: blood vessel formation and growth after ovariectomy and tumor implantation. *Circ Res* **89**, 732-739 (2001).
22. V. Djonov, O. Baum, P. H. Burri, Vascular remodeling by intussusceptive angiogenesis. *Cell Tissue Res* **314**, 107-117 (2003).
23. O. Goldman *et al.*, Endoderm generates endothelial cells during liver development. *Stem Cell Reports* **3**, 556-565 (2014).
24. S. Han, O. Goldman, V. Gouon-Evans, Liver progenitor cell and KDR. *Cell Cycle* **13**, 1051-1052 (2014).
25. H. Zhang *et al.*, Genetic lineage tracing identifies endocardial origin of liver vasculature. *Nat Genet* **48**, 537-543 (2016).
26. M. L. Iruela-Arispe, A dual origin for blood vessels. *Nature* **562**, 195-197 (2018).
27. A. Plein, A. Fantin, L. Denti, J. W. Pollard, C. Ruhrberg, Erythro-myeloid progenitors contribute endothelial cells to blood vessels. *Nature* **562**, 223-228 (2018).
28. K. Matsumoto, H. Yoshitomi, J. Rossant, K. S. Zaret, Liver organogenesis promoted by endothelial cells prior to vascular function. *Science* **294**, 559-563 (2001).
29. E. Lammert, O. Cleaver, D. Melton, Induction of pancreatic differentiation by signals from blood vessels. *Science* **294**, 564-567 (2001).
30. V. L. Bautch, Stem cells and the vasculature. *Nat Med* **17**, 1437-1443 (2011).
31. A. C. Zovein *et al.*, Fate tracing reveals the endothelial origin of hematopoietic stem cells. *Cell Stem Cell* **3**, 625-636 (2008).
32. F. E. Varzaneh, G. Shillabeer, K. L. Wong, D. C. Lau, Extracellular matrix components secreted by microvascular endothelial cells stimulate preadipocyte differentiation in vitro. *Metabolism* **43**, 906-912 (1994).
33. H. P. Gerber *et al.*, VEGF couples hypertrophic cartilage remodeling, ossification and angiogenesis during endochondral bone formation. *Nat Med* **5**, 623-628 (1999).
34. A. Tufro, V. F. Norwood, R. M. Carey, R. A. Gomez, Vascular endothelial growth factor induces nephrogenesis and vasculogenesis. *J Am Soc Nephrol* **10**, 2125-2134 (1999).
35. Q. Shen *et al.*, Endothelial cells stimulate self-renewal and expand neurogenesis of neural stem cells. *Science* **304**, 1338-1340 (2004).
36. C. Lancrin *et al.*, The haemangioblast generates haematopoietic cells through a haemogenic endothelium stage. *Nature* **457**, 892-895 (2009).
37. C. Ottone *et al.*, Direct cell-cell contact with the vascular niche maintains quiescent neural stem cells. *Nat Cell Biol* **16**, 1045-1056 (2014).
38. A. C. Delgado *et al.*, Endothelial NT-3 delivered by vasculature and CSF promotes quiescence of subependymal neural stem cells through nitric oxide induction. *Neuron* **83**, 572-585 (2014).
39. W. Tang *et al.*, White fat progenitor cells reside in the adipose vasculature. *Science* **322**, 583-586 (2008).
40. B. Heissig *et al.*, Recruitment of stem and progenitor cells from the bone marrow niche requires MMP-9 mediated release of kit-ligand. *Cell* **109**, 625-637 (2002).
41. Z. Cao *et al.*, Targeting the vascular and perivascular niches as a regenerative therapy for lung and liver fibrosis. *Sci Transl Med* **9**, (2017).
42. B. S. Ding *et al.*, Endothelial-derived angiocrine signals induce and sustain regenerative lung alveolarization. *Cell* **147**, 539-553 (2011).

43. S. Rafii *et al.*, Platelet-derived SDF-1 primes the pulmonary capillary vascular niche to drive lung alveolar regeneration. *Nat Cell Biol* **17**, 123-136 (2015).
44. Z. Cao *et al.*, Targeting of the pulmonary capillary vascular niche promotes lung alveolar repair and ameliorates fibrosis. *Nat Med* **22**, 154-162 (2016).
45. G. K. Michalopoulos, Liver regeneration. *J Cell Physiol* **213**, 286-300 (2007).
46. G. K. Michalopoulos, M. C. DeFrances, Liver regeneration. *Science* **276**, 60-66 (1997).
47. J. Hu *et al.*, Endothelial cell-derived angiopoietin-2 controls liver regeneration as a spatiotemporal rheostat. *Science* **343**, 416-419 (2014).
48. B. S. Ding *et al.*, Divergent angiocrine signals from vascular niche balance liver regeneration and fibrosis. *Nature* **505**, 97-102 (2014).
49. L. Lorenz *et al.*, Mechanosensing by beta1 integrin induces angiocrine signals for liver growth and survival. *Nature* **562**, 128-132 (2018).
50. P. Carmeliet, R. K. Jain, Molecular mechanisms and clinical applications of angiogenesis. *Nature* **473**, 298-307 (2011).
51. P. Saharinen, L. Eklund, K. Alitalo, Therapeutic targeting of the angiopoietin-TIE pathway. *Nat Rev Drug Discov* **16**, 635-661 (2017).
52. W. Risau, Differentiation of endothelium. *FASEB J* **9**, 926-933 (1995).
53. J. Folkman, Y. Shing, Angiogenesis. *J Biol Chem* **267**, 10931-10934 (1992).
54. T. Asahara *et al.*, Isolation of putative progenitor endothelial cells for angiogenesis. *Science* **275**, 964-967 (1997).
55. Q. Shi *et al.*, Evidence for circulating bone marrow-derived endothelial cells. *Blood* **92**, 362-367 (1998).
56. S. Rafii, Circulating endothelial precursors: mystery, reality, and promise. *J Clin Invest* **105**, 17-19 (2000).
57. T. Asahara, A. Kawamoto, H. Masuda, Concise review: Circulating endothelial progenitor cells for vascular medicine. *Stem Cells* **29**, 1650-1655 (2011).
58. M. Peichev *et al.*, Expression of VEGFR-2 and AC133 by circulating human CD34(+) cells identifies a population of functional endothelial precursors. *Blood* **95**, 952-958 (2000).
59. N. Takakura, Discovery of a vascular endothelial stem cell (VESC) population required for vascular regeneration and tissue maintenance. *Circ J* **83**, 12-17 (2018).
60. K. K. Hirschi, D. A. Ingram, M. C. Yoder, Assessing identity, phenotype, and fate of endothelial progenitor cells. *Arterioscler Thromb Vasc Biol* **28**, 1584-1595 (2008).
61. D. A. Ingram, N. M. Caplice, M. C. Yoder, Unresolved questions, changing definitions, and novel paradigms for defining endothelial progenitor cells. *Blood* **106**, 1525-1531 (2005).
62. C. Urbich, S. Dimmeler, Endothelial progenitor cells: characterization and role in vascular biology. *Circ Res* **95**, 343-353 (2004).
63. J. Patel, P. Donovan, K. Khosrotehrani, Concise review: Functional definition of endothelial progenitor cells: a molecular perspective. *Stem Cells Transl Med* **5**, 1302-1306 (2016).
64. M. S. Chong, W. K. Ng, J. K. Chan, Concise review: Endothelial progenitor cells in regenerative medicine: applications and challenges. *Stem Cells Transl Med* **5**, 530-538 (2016).
65. G. K. Michalopoulos, Hepatostat: Liver regeneration and normal liver tissue maintenance. *Hepatology* **65**, 1384-1392 (2017).

66. C. C. Jadowiec, T. Taner, Liver transplantation: Current status and challenges. *World J Gastroenterol* **22**, 4438-4445 (2016).
67. M. Maes, M. Vinken, H. Jaeschke, Experimental models of hepatotoxicity related to acute liver failure. *Toxicol Appl Pharmacol* **290**, 86-97 (2016).
68. T. M. Rahman, H. J. Hodgson, Animal models of acute hepatic failure. *Int J Exp Pathol* **81**, 145-157 (2000).
69. M. Zhang, A. B. Malik, J. Rehman, Endothelial progenitor cells and vascular repair. *Curr Opin Hematol* **21**, 224-228 (2014).
70. A. S. Bailey *et al.*, Myeloid lineage progenitors give rise to vascular endothelium. *Proc Natl Acad Sci U S A* **103**, 13156-13161 (2006).
71. J. G. Roncalli, J. Tongers, M. A. Renault, D. W. Losordo, Endothelial progenitor cells in regenerative medicine and cancer: a decade of research. *Trends Biotechnol* **26**, 276-283 (2008).
72. N. Werner, G. Nickenig, Endothelial progenitor cells in health and atherosclerotic disease. *Ann Med* **39**, 82-90 (2007).
73. R. Harb *et al.*, Bone marrow progenitor cells repair rat hepatic sinusoidal endothelial cells after liver injury. *Gastroenterology* **137**, 704-712 (2009).
74. L. D. DeLeve, Liver sinusoidal endothelial cells and liver regeneration. *J Clin Invest* **123**, 1861-1866 (2013).
75. L. Wang *et al.*, Liver sinusoidal endothelial cell progenitor cells promote liver regeneration in rats. *J Clin Invest* **122**, 1567-1573 (2012).
76. L. Wang *et al.*, Hepatic vascular endothelial growth factor regulates recruitment of rat liver sinusoidal endothelial cell progenitor cells. *Gastroenterology* **143**, 1555-1563 e1552 (2012).
77. Y. N. Kallis, M. R. Alison, S. J. Forbes, Bone marrow stem cells and liver disease. *Gut* **56**, 716-724 (2007).
78. G. Lanzoni *et al.*, Concise review: clinical programs of stem cell therapies for liver and pancreas. *Stem Cells* **31**, 2047-2060 (2013).
79. S. J. Forbes, P. N. Newsome, New horizons for stem cell therapy in liver disease. *J Hepatol* **56**, 496-499 (2012).
80. R. C. Huebert, J. Rakela, Cellular therapy for liver disease. *Mayo Clin Proc* **89**, 414-424 (2014).
81. J. K. Moore, B. M. Stutchfield, S. J. Forbes, Systematic review: the effects of autologous stem cell therapy for patients with liver disease. *Aliment Pharmacol Ther* **39**, 673-685 (2014).
82. S. Terai *et al.*, Improved liver function in patients with liver cirrhosis after autologous bone marrow cell infusion therapy. *Stem Cells* **24**, 2292-2298 (2006).
83. M. Y. Gordon *et al.*, Characterization and clinical application of human CD34+ stem/progenitor cell populations mobilized into the blood by granulocyte colony-stimulating factor. *Stem Cells* **24**, 1822-1830 (2006).
84. S. Gaia *et al.*, Feasibility and safety of G-CSF administration to induce bone marrow-derived cells mobilization in patients with end stage liver disease. *J Hepatol* **45**, 13-19 (2006).
85. A. King, P. N. Newsome, Bone marrow stem cell therapy for liver disease. *Dig Dis* **32**, 494-501 (2014).

86. B. M. Stutchfield, S. J. Forbes, S. J. Wigmore, Prospects for stem cell transplantation in the treatment of hepatic disease. *Liver Transpl* **16**, 827-836 (2010).
87. M. J. Williams, A. D. Clouston, S. J. Forbes, Links between hepatic fibrosis, ductular reaction, and progenitor cell expansion. *Gastroenterology* **146**, 349-356 (2014).
88. L. Spahr *et al.*, Autologous bone marrow mononuclear cell transplantation in patients with decompensated alcoholic liver disease: a randomized controlled trial. *PLoS One* **8**, e53719 (2013).
89. P. N. Newsome *et al.*, Granulocyte colony-stimulating factor and autologous CD133-positive stem-cell therapy in liver cirrhosis (REALISTIC): an open-label, randomised, controlled phase 2 trial. *Lancet Gastroenterol Hepatol* **3**, 25-36 (2018).
90. D. Hanahan, R. A. Weinberg, The hallmarks of cancer. *Cell* **100**, 57-70 (2000).
91. D. Hanahan, R. A. Weinberg, Hallmarks of cancer: the next generation. *Cell* **144**, 646-674 (2011).
92. A. W. Lambert, D. R. Pattabiraman, R. A. Weinberg, Emerging biological principles of metastasis. *Cell* **168**, 670-691 (2017).
93. J. Folkman, Tumor angiogenesis: therapeutic implications. *N Engl J Med* **285**, 1182-1186 (1971).
94. I. F. Tannock, The relation between cell proliferation and the vascular system in a transplanted mouse mammary tumour. *Br J Cancer* **22**, 258-273 (1968).
95. I. F. Tannock, Population kinetics of carcinoma cells, capillary endothelial cells, and fibroblasts in a transplanted mouse mammary tumor. *Cancer Res* **30**, 2470-2476 (1970).
96. R. K. Jain, P. Au, J. Tam, D. G. Duda, D. Fukumura, Engineering vascularized tissue. *Nat Biotechnol* **23**, 821-823 (2005).
97. G. P. Gupta, J. Massague, Cancer metastasis: building a framework. *Cell* **127**, 679-695 (2006).
98. D. R. Senger *et al.*, Tumor cells secrete a vascular permeability factor that promotes accumulation of ascites fluid. *Science* **219**, 983-985 (1983).
99. N. Ferrara, W. J. Henzel, Pituitary follicular cells secrete a novel heparin-binding growth factor specific for vascular endothelial cells. *Biochem Biophys Res Commun* **161**, 851-858 (1989).
100. D. W. Leung, G. Cachianes, W. J. Kuang, D. V. Goeddel, N. Ferrara, Vascular endothelial growth factor is a secreted angiogenic mitogen. *Science* **246**, 1306-1309 (1989).
101. N. Ferrara, Binding to the extracellular matrix and proteolytic processing: two key mechanisms regulating vascular endothelial growth factor action. *Mol Biol Cell* **21**, 687-690 (2010).
102. K. A. Houck, D. W. Leung, A. M. Rowland, J. Winer, N. Ferrara, Dual regulation of vascular endothelial growth factor bioavailability by genetic and proteolytic mechanisms. *J Biol Chem* **267**, 26031-26037 (1992).
103. S. Lee, S. M. Jilani, G. V. Nikolova, D. Carpizo, M. L. Iruela-Arispe, Processing of VEGF-A by matrix metalloproteinases regulates bioavailability and vascular patterning in tumors. *J Cell Biol* **169**, 681-691 (2005).
104. C. de Vries *et al.*, The fms-like tyrosine kinase, a receptor for vascular endothelial growth factor. *Science* **255**, 989-991 (1992).

105. B. I. Terman *et al.*, Identification of the KDR tyrosine kinase as a receptor for vascular endothelial cell growth factor. *Biochem Biophys Res Commun* **187**, 1579-1586 (1992).
106. R. S. Apte, D. S. Chen, N. Ferrara, VEGF in signaling and disease: Beyond discovery and development. *Cell* **176**, 1248-1264 (2019).
107. A. K. Olsson, A. Dimberg, J. Kreuger, L. Claesson-Welsh, VEGF receptor signalling - in control of vascular function. *Nat Rev Mol Cell Biol* **7**, 359-371 (2006).
108. N. Ferrara, A. P. Adamis, Ten years of anti-vascular endothelial growth factor therapy. *Nat Rev Drug Discov* **15**, 385-403 (2016).
109. C. H. Ha, B. S. Jhun, H. Y. Kao, Z. G. Jin, VEGF stimulates HDAC7 phosphorylation and cytoplasmic accumulation modulating matrix metalloproteinase expression and angiogenesis. *Arterioscler Thromb Vasc Biol* **28**, 1782-1788 (2008).
110. P. Subarsky, R. P. Hill, The hypoxic tumour microenvironment and metastatic progression. *Clin Exp Metastasis* **20**, 237-250 (2003).
111. R. S. Kerbel, Tumor angiogenesis. *N Engl J Med* **358**, 2039-2049 (2008).
112. P. Buchler *et al.*, Hypoxia-inducible factor 1 regulates vascular endothelial growth factor expression in human pancreatic cancer. *Pancreas* **26**, 56-64 (2003).
113. C. Lin, R. McGough, B. Aswad, J. A. Block, R. Terek, Hypoxia induces HIF-1 α and VEGF expression in chondrosarcoma cells and chondrocytes. *J Orthop Res* **22**, 1175-1181 (2004).
114. G. L. Semenza, Targeting HIF-1 for cancer therapy. *Nat Rev Cancer* **3**, 721-732 (2003).
115. P. Carmeliet, VEGF as a key mediator of angiogenesis in cancer. *Oncology* **69 Suppl 3**, 4-10 (2005).
116. H. L. Goel, A. M. Mercurio, VEGF targets the tumour cell. *Nat Rev Cancer* **13**, 871-882 (2013).
117. K. J. Kim *et al.*, Inhibition of vascular endothelial growth factor-induced angiogenesis suppresses tumour growth in vivo. *Nature* **362**, 841-844 (1993).
118. L. G. Presta *et al.*, Humanization of an anti-vascular endothelial growth factor monoclonal antibody for the therapy of solid tumors and other disorders. *Cancer Res* **57**, 4593-4599 (1997).
119. J. C. Yang *et al.*, A randomized trial of bevacizumab, an anti-vascular endothelial growth factor antibody, for metastatic renal cancer. *N Engl J Med* **349**, 427-434 (2003).
120. H. Hurwitz *et al.*, Bevacizumab plus irinotecan, fluorouracil, and leucovorin for metastatic colorectal cancer. *N Engl J Med* **350**, 2335-2342 (2004).
121. N. Ferrara, K. J. Hillan, H. P. Gerber, W. Novotny, Discovery and development of bevacizumab, an anti-VEGF antibody for treating cancer. *Nat Rev Drug Discov* **3**, 391-400 (2004).
122. T. Shih, C. Lindley, Bevacizumab: an angiogenesis inhibitor for the treatment of solid malignancies. *Clin Ther* **28**, 1779-1802 (2006).
123. L. M. Ellis, D. J. Hicklin, VEGF-targeted therapy: mechanisms of anti-tumour activity. *Nat Rev Cancer* **8**, 579-591 (2008).
124. A. Grothey, E. Galanis, Targeting angiogenesis: progress with anti-VEGF treatment with large molecules. *Nat Rev Clin Oncol* **6**, 507-518 (2009).
125. B. Sitohy, J. A. Nagy, H. F. Dvorak, Anti-VEGF/VEGFR therapy for cancer: reassessing the target. *Cancer Res* **72**, 1909-1914 (2012).
126. R. K. Jain, D. G. Duda, J. W. Clark, J. S. Loeffler, Lessons from phase III clinical trials on anti-VEGF therapy for cancer. *Nat Clin Pract Oncol* **3**, 24-40 (2006).

127. R. K. Jain, Normalizing tumor vasculature with anti-angiogenic therapy: a new paradigm for combination therapy. *Nat Med* **7**, 987-989 (2001).
128. R. K. Jain, Normalization of tumor vasculature: an emerging concept in antiangiogenic therapy. *Science* **307**, 58-62 (2005).
129. R. K. Jain, Normalizing tumor microenvironment to treat cancer: bench to bedside to biomarkers. *J Clin Oncol* **31**, 2205-2218 (2013).
130. H. P. Gerber, N. Ferrara, Pharmacology and pharmacodynamics of bevacizumab as monotherapy or in combination with cytotoxic therapy in preclinical studies. *Cancer Res* **65**, 671-680 (2005).
131. R. K. Jain, Antiangiogenesis strategies revisited: from starving tumors to alleviating hypoxia. *Cancer Cell* **26**, 605-622 (2014).
132. A. A. Van der Veldt *et al.*, Rapid decrease in delivery of chemotherapy to tumors after anti-VEGF therapy: implications for scheduling of anti-angiogenic drugs. *Cancer Cell* **21**, 82-91 (2012).
133. M. H. Zissen *et al.*, 18F-5-fluorouracil dynamic positron emission tomography/computed tomography shows decreased tracer activity after bevacizumab in colorectal metastases. *Nucl Med Commun* **32**, 343-347 (2011).
134. T. T. Batchelor *et al.*, AZD2171, a pan-VEGF receptor tyrosine kinase inhibitor, normalizes tumor vasculature and alleviates edema in glioblastoma patients. *Cancer Cell* **11**, 83-95 (2007).
135. T. T. Batchelor *et al.*, Phase II study of cediranib, an oral pan-vascular endothelial growth factor receptor tyrosine kinase inhibitor, in patients with recurrent glioblastoma. *J Clin Oncol* **28**, 2817-2823 (2010).
136. T. T. Batchelor *et al.*, Improved tumor oxygenation and survival in glioblastoma patients who show increased blood perfusion after cediranib and chemoradiation. *Proc Natl Acad Sci U S A* **110**, 19059-19064 (2013).
137. T. T. Batchelor *et al.*, Phase III randomized trial comparing the efficacy of cediranib as monotherapy, and in combination with lomustine, versus lomustine alone in patients with recurrent glioblastoma. *J Clin Oncol* **31**, 3212-3218 (2013).
138. N. S. Vasudev, A. R. Reynolds, Anti-angiogenic therapy for cancer: current progress, unresolved questions and future directions. *Angiogenesis* **17**, 471-494 (2014).
139. P. Carmeliet, R. K. Jain, Principles and mechanisms of vessel normalization for cancer and other angiogenic diseases. *Nat Rev Drug Discov* **10**, 417-427 (2011).
140. M. Thomas, H. G. Augustin, The role of the Angiopoietins in vascular morphogenesis. *Angiogenesis* **12**, 125-137 (2009).
141. H. G. Augustin, G. Y. Koh, G. Thurston, K. Alitalo, Control of vascular morphogenesis and homeostasis through the angiopoietin-Tie system. *Nat Rev Mol Cell Biol* **10**, 165-177 (2009).
142. H. T. Yuan, E. V. Khankin, S. A. Karumanchi, S. M. Parikh, Angiopoietin 2 is a partial agonist/antagonist of Tie2 signaling in the endothelium. *Mol Cell Biol* **29**, 2011-2022 (2009).
143. M. Scharpfenecker, U. Fiedler, Y. Reiss, H. G. Augustin, The Tie-2 ligand angiopoietin-2 destabilizes quiescent endothelium through an internal autocrine loop mechanism. *J Cell Sci* **118**, 771-780 (2005).

144. N. W. Gale *et al.*, Angiopoietin-2 is required for postnatal angiogenesis and lymphatic patterning, and only the latter role is rescued by Angiopoietin-1. *Dev Cell* **3**, 411-423 (2002).
145. B. Hu, S. Y. Cheng, Angiopoietin-2: development of inhibitors for cancer therapy. *Curr Oncol Rep* **11**, 111-116 (2009).
146. D. Gerald, S. Chintharlapalli, H. G. Augustin, L. E. Benjamin, Angiopoietin-2: an attractive target for improved antiangiogenic tumor therapy. *Cancer Res* **73**, 1649-1657 (2013).
147. T. Holopainen *et al.*, Effects of angiopoietin-2-blocking antibody on endothelial cell-cell junctions and lung metastasis. *J Natl Cancer Inst* **104**, 461-475 (2012).
148. J. Oliner *et al.*, Suppression of angiogenesis and tumor growth by selective inhibition of angiopoietin-2. *Cancer Cell* **6**, 507-516 (2004).
149. P. Nasarre *et al.*, Host-derived angiopoietin-2 affects early stages of tumor development and vessel maturation but is dispensable for later stages of tumor growth. *Cancer Res* **69**, 1324-1333 (2009).
150. Y. J. Koh *et al.*, Double antiangiogenic protein, DAAP, targeting VEGF-A and angiopoietins in tumor angiogenesis, metastasis, and vascular leakage. *Cancer Cell* **18**, 171-184 (2010).
151. B. J. Monk *et al.*, Anti-angiopoietin therapy with trebananib for recurrent ovarian cancer (TRINOVA-1): a randomised, multicentre, double-blind, placebo-controlled phase 3 trial. *Lancet Oncol* **15**, 799-808 (2014).
152. B. J. Monk *et al.*, Final results of a phase 3 study of trebananib plus weekly paclitaxel in recurrent ovarian cancer (TRINOVA-1): Long-term survival, impact of ascites, and progression-free survival-2. *Gynecol Oncol* **143**, 27-34 (2016).
153. I. Vergote *et al.*, Trebananib or placebo plus carboplatin and paclitaxel as first-line treatment for advanced ovarian cancer (TRINOVA-3/ENGOT-ov2/GOG-3001): a randomised, double-blind, phase 3 trial. *Lancet Oncol*, (2019).
154. L. Moserle, G. Jimenez-Valerio, O. Casanovas, Antiangiogenic therapies: going beyond their limits. *Cancer Discov* **4**, 31-41 (2014).
155. G. Nikolova, B. Strilic, E. Lammert, The vascular niche and its basement membrane. *Trends Cell Biol* **17**, 19-25 (2007).
156. B. Beck *et al.*, A vascular niche and a VEGF-Nrp1 loop regulate the initiation and stemness of skin tumours. *Nature* **478**, 399-403 (2011).
157. R. J. Gilbertson, J. N. Rich, Making a tumour's bed: glioblastoma stem cells and the vascular niche. *Nat Rev Cancer* **7**, 733-736 (2007).
158. F. M. R. Witjas, B. M. van den Berg, C. W. van den Berg, M. A. Engelse, T. J. Rabelink, Concise review: The endothelial cell extracellular matrix regulates tissue homeostasis and repair. *Stem Cells Transl Med* **8**, 375-382 (2019).
159. G. S. Schultz, A. Wysocki, Interactions between extracellular matrix and growth factors in wound healing. *Wound Repair Regen* **17**, 153-162 (2009).
160. Y. Ben-Yosef, A. Miller, S. Shapiro, N. Lahat, Hypoxia of endothelial cells leads to MMP-2-dependent survival and death. *Am J Physiol Cell Physiol* **289**, C1321-1331 (2005).
161. J. Fang *et al.*, Matrix metalloproteinase-2 is required for the switch to the angiogenic phenotype in a tumor model. *Proc Natl Acad Sci U S A* **97**, 3884-3889 (2000).
162. G. Bergers *et al.*, Matrix metalloproteinase-9 triggers the angiogenic switch during carcinogenesis. *Nat Cell Biol* **2**, 737-744 (2000).

163. J. S. Pober, W. C. Sessa, Evolving functions of endothelial cells in inflammation. *Nat Rev Immunol* **7**, 803-815 (2007).
164. J. Mai, A. Virtue, J. Shen, H. Wang, X. F. Yang, An evolving new paradigm: endothelial cells--conditional innate immune cells. *J Hematol Oncol* **6**, 61 (2013).
165. M. P. Bevilacqua, Endothelial-leukocyte adhesion molecules. *Annu Rev Immunol* **11**, 767-804 (1993).
166. T. Collins *et al.*, Transcriptional regulation of endothelial cell adhesion molecules: NF-kappa B and cytokine-inducible enhancers. *FASEB J* **9**, 899-909 (1995).
167. J. S. Pober, R. S. Cotran, Cytokines and endothelial cell biology. *Physiol Rev* **70**, 427-451 (1990).
168. J. R. Teijaro *et al.*, Endothelial cells are central orchestrators of cytokine amplification during influenza virus infection. *Cell* **146**, 980-991 (2011).
169. I. Novitzky-Basso, A. Rot, Duffy antigen receptor for chemokines and its involvement in patterning and control of inflammatory chemokines. *Front Immunol* **3**, 266 (2012).
170. S. C. Peiper *et al.*, The Duffy antigen/receptor for chemokines (DARC) is expressed in endothelial cells of Duffy negative individuals who lack the erythrocyte receptor. *J Exp Med* **181**, 1311-1317 (1995).
171. J. Kloepper *et al.*, Ang-2/VEGF bispecific antibody reprograms macrophages and resident microglia to anti-tumor phenotype and prolongs glioblastoma survival. *Proc Natl Acad Sci U S A* **113**, 4476-4481 (2016).
172. T. E. Peterson *et al.*, Dual inhibition of Ang-2 and VEGF receptors normalizes tumor vasculature and prolongs survival in glioblastoma by altering macrophages. *Proc Natl Acad Sci U S A* **113**, 4470-4475 (2016).
173. K. Srivastava *et al.*, Postsurgical adjuvant tumor therapy by combining anti-angiopoietin-2 and metronomic chemotherapy limits metastatic growth. *Cancer Cell* **26**, 880-895 (2014).
174. G. Poste, I. J. Fidler, The pathogenesis of cancer metastasis. *Nature* **283**, 139-146 (1980).
175. I. J. Fidler, G. Poste, The "seed and soil" hypothesis revisited. *Lancet Oncol* **9**, 808 (2008).
176. J. Folkman, Angiogenesis in cancer, vascular, rheumatoid and other disease. *Nat Med* **1**, 27-31 (1995).
177. J. Folkman, Role of angiogenesis in tumor growth and metastasis. *Semin Oncol* **29**, 15-18 (2002).
178. M. Esposito *et al.*, Bone vascular niche E-selectin induces mesenchymal-epithelial transition and Wnt activation in cancer cells to promote bone metastasis. *Nat Cell Biol* **21**, 627-639 (2019).
179. U. Harjes, E-selectin fills two needs for metastasis. *Nat Rev Cancer* **19**, 301 (2019).
180. A. Zijlstra, J. P. Quigley, The DARC side of metastasis: shining a light on KAI1-mediated metastasis suppression in the vascular tunnel. *Cancer Cell* **10**, 177-178 (2006).
181. S. Bandyopadhyay *et al.*, Interaction of KAI1 on tumor cells with DARC on vascular endothelium leads to metastasis suppression. *Nat Med* **12**, 933-938 (2006).
182. C. Roca, R. H. Adams, Regulation of vascular morphogenesis by Notch signaling. *Genes Dev* **21**, 2511-2524 (2007).

183. R. Zhang *et al.*, In vivo cardiac reprogramming contributes to zebrafish heart regeneration. *Nature* **498**, 497-501 (2013).
184. P. Ntziachristos, J. S. Lim, J. Sage, I. Aifantis, From fly wings to targeted cancer therapies: a centennial for notch signaling. *Cancer Cell* **25**, 318-334 (2014).
185. P. Guo, S. Rafii, Dangerous Liaisons: Deviant Endothelium NOTCHes toward Tumor Metastasis. *Cancer Cell* **31**, 301-303 (2017).
186. E. Wieland *et al.*, Endothelial Notch1 Activity Facilitates Metastasis. *Cancer Cell* **31**, 355-367 (2017).
187. Z. Cao *et al.*, Angiocrine factors deployed by tumor vascular niche induce B cell lymphoma invasiveness and chemoresistance. *Cancer Cell* **25**, 350-365 (2014).
188. S. Seton-Rogers, Microenvironment: Endothelial cells create a niche. *Nat Rev Cancer* **14**, 298 (2014).
189. Y. Liu, X. Cao, Characteristics and significance of the pre-metastatic niche. *Cancer Cell* **30**, 668-681 (2016).
190. C. Mitchell, H. Willenbring, A reproducible and well-tolerated method for 2/3 partial hepatectomy in mice. *Nat Protoc* **3**, 1167-1170 (2008).
191. W. Hilbe *et al.*, CD133 positive endothelial progenitor cells contribute to the tumour vasculature in non-small cell lung cancer. *J Clin Pathol* **57**, 965-969 (2004).
192. M. Paprocka *et al.*, CD133 positive progenitor endothelial cell lines from human cord blood. *Cytometry A* **79**, 594-602 (2011).
193. V. Mathews *et al.*, Recruitment of bone marrow-derived endothelial cells to sites of pancreatic beta-cell injury. *Diabetes* **53**, 91-98 (2004).
194. R. E. Langley, E. A. Bump, S. G. Quartuccio, D. Medeiros, S. J. Braunhut, Radiation-induced apoptosis in microvascular endothelial cells. *Br J Cancer* **75**, 666-672 (1997).
195. D. Gao *et al.*, Endothelial progenitor cells control the angiogenic switch in mouse lung metastasis. *Science* **319**, 195-198 (2008).
196. A. D. Bhatwadekar *et al.*, Retinal endothelial cell apoptosis stimulates recruitment of endothelial progenitor cells. *Invest Ophthalmol Vis Sci* **50**, 4967-4973 (2009).
197. J. Dietrich *et al.*, Bone marrow drives central nervous system regeneration after radiation injury. *J Clin Invest* **128**, 281-293 (2018).
198. J. P. Abbuehl, Z. Tatarova, W. Held, J. Huelsken, Long-term engraftment of primary bone marrow stromal cells repairs niche damage and improves hematopoietic stem cell transplantation. *Cell Stem Cell* **21**, 241-255 e246 (2017).
199. C. Waskow *et al.*, Hematopoietic stem cell transplantation without irradiation. *Nat Methods* **6**, 267-269 (2009).
200. T. Hofer, K. Busch, K. Klapproth, H. R. Rodewald, Fate mapping and quantitation of hematopoiesis in vivo. *Annu Rev Immunol* **34**, 449-478 (2016).
201. L. He *et al.*, Preexisting endothelial cells mediate cardiac neovascularization after injury. *J Clin Invest* **127**, 2968-2981 (2017).
202. S. Purhonen *et al.*, Bone marrow-derived circulating endothelial precursors do not contribute to vascular endothelium and are not needed for tumor growth. *Proc Natl Acad Sci U S A* **105**, 6620-6625 (2008).
203. B. A. Peters *et al.*, Contribution of bone marrow-derived endothelial cells to human tumor vasculature. *Nat Med* **11**, 261-262 (2005).
204. T. Wakabayashi *et al.*, CD157 marks tissue-resident endothelial stem cells with homeostatic and regenerative properties. *Cell Stem Cell* **22**, 384-397 e386 (2018).

-
205. A. I. McDonald *et al.*, Endothelial regeneration of large vessels is a biphasic process driven by local cells with distinct proliferative capacities. *Cell Stem Cell* **23**, 210-225 e216 (2018).
 206. J. P. Iredale, Models of liver fibrosis: exploring the dynamic nature of inflammation and repair in a solid organ. *J Clin Invest* **117**, 539-548 (2007).
 207. H. Malhi, G. J. Gores, Cellular and molecular mechanisms of liver injury. *Gastroenterology* **134**, 1641-1654 (2008).
 208. D. A. Muruve, M. J. Barnes, I. E. Stillman, T. A. Libermann, Adenoviral gene therapy leads to rapid induction of multiple chemokines and acute neutrophil-dependent hepatic injury in vivo. *Hum Gene Ther* **10**, 965-976 (1999).
 209. D. M. Shayakhmetov, Z. Y. Li, S. Ni, A. Lieber, Analysis of adenovirus sequestration in the liver, transduction of hepatic cells, and innate toxicity after injection of fiber-modified vectors. *J Virol* **78**, 5368-5381 (2004).
 210. T. Verbiest *et al.*, NOD scid gamma mice are permissive to allogeneic HSC transplantation without prior conditioning. *Int J Mol Sci* **17**, (2016).
 211. E. Gomez Perdiguero *et al.*, Tissue-resident macrophages originate from yolk-sac-derived erythro-myeloid progenitors. *Nature* **518**, 547-551 (2015).
 212. C. Stremmel *et al.*, Yolk sac macrophage progenitors traffic to the embryo during defined stages of development. *Nat Commun* **9**, 75 (2018).
 213. R. K. Hopman, J. F. DiPersio, Advances in stem cell mobilization. *Blood Rev* **28**, 31-40 (2014).
 214. S. Yoshikawa *et al.*, Characterization of CD133+ parenchymal cells in the liver: histology and culture. *World J Gastroenterol* **15**, 4896-4906 (2009).
 215. Z. Zhu *et al.*, Cancer stem/progenitor cells are highly enriched in CD133+CD44+ population in hepatocellular carcinoma. *Int J Cancer* **126**, 2067-2078 (2010).
 216. P. Mehlen, A. Puisieux, Metastasis: a question of life or death. *Nat Rev Cancer* **6**, 449-458 (2006).
 217. N. Gengenbacher, M. Singhal, H. G. Augustin, Preclinical mouse solid tumour models: status quo, challenges and perspectives. *Nat Rev Cancer* **17**, 751-765 (2017).
 218. R. Demicheli, M. W. Retsky, W. J. Hrushesky, M. Baum, Tumor dormancy and surgery-driven interruption of dormancy in breast cancer: learning from failures. *Nat Clin Pract Oncol* **4**, 699-710 (2007).
 219. K. Smietana, M. Siatkowski, M. Moller, Trends in clinical success rates. *Nat Rev Drug Discov* **15**, 379-380 (2016).
 220. A. Mullard, Parsing clinical success rates. *Nat Rev Drug Discov* **15**, 447 (2016).
 221. M. De Palma, D. Biziato, T. V. Petrova, Microenvironmental regulation of tumour angiogenesis. *Nat Rev Cancer* **17**, 457-474 (2017).
 222. H. Peinado *et al.*, Pre-metastatic niches: organ-specific homes for metastases. *Nat Rev Cancer* **17**, 302-317 (2017).
 223. M. Binnewies *et al.*, Understanding the tumor immune microenvironment (TIME) for effective therapy. *Nat Med* **24**, 541-550 (2018).
 224. D. F. Quail, J. A. Joyce, Microenvironmental regulation of tumor progression and metastasis. *Nat Med* **19**, 1423-1437 (2013).

-
225. C. Devaud, L. B. John, J. A. Westwood, P. K. Darcy, M. H. Kershaw, Immune modulation of the tumor microenvironment for enhancing cancer immunotherapy. *Oncoimmunology* **2**, e25961 (2013).
 226. X. Wang *et al.*, LRG1 promotes angiogenesis by modulating endothelial TGF-beta signalling. *Nature* **499**, 306-311 (2013).
 227. S. Kumagai *et al.*, Myeloid cell-derived LRG attenuates adverse cardiac remodelling after myocardial infarction. *Cardiovasc Res* **109**, 272-282 (2016).
 228. K. Schlereth *et al.*, The transcriptomic and epigenetic map of vascular quiescence in the continuous lung endothelium. *Elife* **7**, (2018).
 229. J. D. Andersen *et al.*, Leucine-rich alpha-2-glycoprotein-1 is upregulated in sera and tumors of ovarian cancer patients. *J Ovarian Res* **3**, 21 (2010).
 230. K. Furukawa *et al.*, Clinicopathological significance of leucine-rich alpha2-glycoprotein-1 in sera of patients with pancreatic cancer. *Pancreas* **44**, 93-98 (2015).
 231. Y. S. Liu *et al.*, Shotgun and targeted proteomics reveal that pre-surgery serum levels of LRG1, SAA, and C4BP may refine prognosis of resected squamous cell lung cancer. *J Mol Cell Biol* **4**, 344-347 (2012).
 232. E. Shinozaki *et al.*, Serum leucine-rich alpha-2-glycoprotein-1 with fucosylated triantennary N-glycan: a novel colorectal cancer marker. *BMC Cancer* **18**, 406 (2018).
 233. M. Yamamoto *et al.*, Overexpression of leucine-rich alpha2-glycoprotein-1 is a prognostic marker and enhances tumor migration in gastric cancer. *Cancer Sci* **108**, 2052-2060 (2017).
 234. L. C. O'Donnell, L. J. Druhan, B. R. Avalos, Molecular characterization and expression analysis of leucine-rich alpha2-glycoprotein, a novel marker of granulocytic differentiation. *J Leukoc Biol* **72**, 478-485 (2002).
 235. L. J. Druhan *et al.*, Leucine rich alpha-2 glycoprotein: A novel neutrophil granule protein and modulator of myelopoiesis. *PLoS One* **12**, e0170261 (2017).
 236. Q. Zhao *et al.*, Single-cell transcriptome analyses reveal endothelial cell heterogeneity in tumors and changes following antiangiogenic treatment. *Cancer Res* **78**, 2370-2382 (2018).
 237. M. Vanlandewijck *et al.*, A molecular atlas of cell types and zonation in the brain vasculature. *Nature* **554**, 475-480 (2018).
 238. K. Saito *et al.*, Gene expression profiling of mucosal addressin cell adhesion molecule-1+ high endothelial venule cells (HEV) and identification of a leucine-rich HEV glycoprotein as a HEV marker. *J Immunol* **168**, 1050-1059 (2002).
 239. F. Shojaei *et al.*, Bv8 regulates myeloid-cell-dependent tumour angiogenesis. *Nature* **450**, 825-831 (2007).
 240. F. Shojaei *et al.*, Tumor refractoriness to anti-VEGF treatment is mediated by CD11b+Gr1+ myeloid cells. *Nat Biotechnol* **25**, 911-920 (2007).
 241. D. Scholten, J. Trebicka, C. Liedtke, R. Weiskirchen, The carbon tetrachloride model in mice. *Lab Anim* **49**, 4-11 (2015).
 242. A. Dobin, T. R. Gingeras, Mapping RNA-seq reads with STAR. *Curr Protoc Bioinformatics* **51**, 11.14 (2015).
 243. M. I. Love, W. Huber, S. Anders, Moderated estimation of fold change and dispersion for RNA-seq data with DESeq2. *Genome Biol* **15**, 550 (2014).
 244. R. Satija, J. A. Farrell, D. Gennert, A. F. Schier, A. Regev, Spatial reconstruction of single-cell gene expression data. *Nat Biotechnol* **33**, 495-502 (2015).

-
245. G. Kramer *et al.*, Accuracy and reproducibility in quantification of plasma protein concentrations by mass spectrometry without the use of isotopic standards. *PLoS One* **10**, e0140097 (2015).
 246. J. Cox, M. Mann, MaxQuant enables high peptide identification rates, individualized p.p.b.-range mass accuracies and proteome-wide protein quantification. *Nat Biotechnol* **26**, 1367-1372 (2008).
 247. J. Cox *et al.*, Andromeda: a peptide search engine integrated into the MaxQuant environment. *J Proteome Res* **10**, 1794-1805 (2011).
 248. Y. Perez-Riverol *et al.*, The PRIDE database and related tools and resources in 2019: improving support for quantification data. *Nucleic Acids Res* **47**, D442-D450 (2019).